



National Library  
of Canada

Acquisitions and  
Bibliographic Services Branch

395 Wellington Street  
Ottawa, Ontario  
K1A 0N4

Bibliothèque nationale  
du Canada

Direction des acquisitions et  
des services bibliographiques

395, rue Wellington  
Ottawa (Ontario)  
K1A 0N4

*Your file* *Votre référence*

*Our file* *Notre référence*

## NOTICE

The quality of this microform is heavily dependent upon the quality of the original thesis submitted for microfilming. Every effort has been made to ensure the highest quality of reproduction possible.

If pages are missing, contact the university which granted the degree.

Some pages may have indistinct print especially if the original pages were typed with a poor typewriter ribbon or if the university sent us an inferior photocopy.

Reproduction in full or in part of this microform is governed by the Canadian Copyright Act, R.S.C. 1970, c. C-30, and subsequent amendments.

## AVIS

La qualité de cette microforme dépend grandement de la qualité de la thèse soumise au microfilmage. Nous avons tout fait pour assurer une qualité supérieure de reproduction.

S'il manque des pages, veuillez communiquer avec l'université qui a conféré le grade.

La qualité d'impression de certaines pages peut laisser à désirer, surtout si les pages originales ont été dactylographiées à l'aide d'un ruban usé ou si l'université nous a fait parvenir une photocopie de qualité inférieure.

La reproduction, même partielle, de cette microforme est soumise à la Loi canadienne sur le droit d'auteur, SRC 1970, c. C-30, et ses amendements subséquents.

Canada

University of Alberta

**RADAR OBSERVATIONS OF PRECIPITATION PRODUCTION  
IN ALBERTA SNOWBANDS**

by

Raymond Beaubien

A thesis submitted to the Faculty of Graduate Studies and  
Research in partial fulfillment of the requirements for the  
degree of MASTER OF SCIENCE

in

**METEOROLOGY**

**DEPARTMENT OF GEOGRAPHY**

Edmonton, Alberta

Spring 1995



National Library  
of Canada

Acquisitions and  
Bibliographic Services Branch

395 Wellington Street  
Ottawa, Ontario  
K1A 0N4

Bibliothèque nationale  
du Canada

Direction des acquisitions et  
des services bibliographiques

395, rue Wellington  
Ottawa (Ontario)  
K1A 0N4

*Your file* *Votre référence*

*Our file* *Notre référence*

THE AUTHOR HAS GRANTED AN IRREVOCABLE NON-EXCLUSIVE LICENCE ALLOWING THE NATIONAL LIBRARY OF CANADA TO REPRODUCE, LOAN, DISTRIBUTE OR SELL COPIES OF HIS/HER THESIS BY ANY MEANS AND IN ANY FORM OR FORMAT, MAKING THIS THESIS AVAILABLE TO INTERESTED PERSONS.

L'AUTEUR A ACCORDE UNE LICENCE IRREVOCABLE ET NON EXCLUSIVE PERMETTANT A LA BIBLIOTHEQUE NATIONALE DU CANADA DE REPRODUIRE, PRETER, DISTRIBUER OU VENDRE DES COPIES DE SA THESE DE QUELQUE MANIERE ET SOUS QUELQUE FORME QUE CE SOIT POUR METTRE DES EXEMPLAIRES DE CETTE THESE A LA DISPOSITION DES PERSONNE INTERESSEES.

THE AUTHOR RETAINS OWNERSHIP OF THE COPYRIGHT IN HIS/HER THESIS. NEITHER THE THESIS NOR SUBSTANTIAL EXTRACTS FROM IT MAY BE PRINTED OR OTHERWISE REPRODUCED WITHOUT HIS/HER PERMISSION.

L'AUTEUR CONSERVE LA PROPRIETE DU DROIT D'AUTEUR QUI PROTEGE SA THESE. NI LA THESE NI DES EXTRAITS SUBSTANTIELS DE CELLE-CI NE DOIVENT ETRE IMPRIMES OU AUTREMENT REPRODUITS SANS SON AUTORISATION.

ISBN 0-612-01581-5

Canada

University of Alberta  
Library Release Form

Name of Author: Raymond Beaubien

Title of Thesis: Radar observations of precipitation  
production in Alberta snowbands

Degree: Master of Science

Year this Degree Granted: 1995

Permission is hereby granted to the University of Alberta Library to reproduce single copies of this thesis and to lend or sell such copies for private, scholarly, or scientific research purposes only.

The author reserves all other publication and other rights in association with the copyright in the thesis, and except as hereinbefore provided, neither the thesis nor any substantial portion thereof may be printed or otherwise reproduced in any material form whatever without the author's prior written permission.



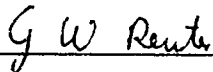
Raymond Beaubien  
6719-101A Ave  
Edmonton, Alberta  
T6A 0M3

20 April 1995

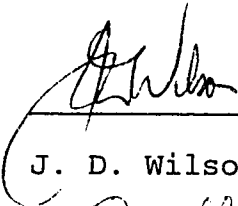
University of Alberta

Faculty of Graduate Studies and Research


The undersigned certify that they have read, and recommend to the Faculty of Graduate Studies and Research for acceptance, a thesis entitled RADAR OBSERVATIONS OF PRECIPITATION PRODUCTION IN ALBERTA SNOWBANDS submitted by Raymond Beaubien in partial fulfillment of the requirements for the degree of MASTER OF SCIENCE in METEOROLOGY.

  
\_\_\_\_\_

G. W. Reuter, Supervisor

  
\_\_\_\_\_

J. D. Wilson

  
\_\_\_\_\_

T. Y. Gan

13 April 1994

## Abstract

Radar observations, sounding data, and synoptic charts were analyzed to investigate two snowband cases over central Alberta. The Richardson number stability analysis indicated that the warm frontal snowband of 16 October 1991 occurred in an airmass that was unstable for Conditional Symmetric Instability. The cold frontal snowband of 13 February 1994 developed in a convectively unstable airmass. Taking ice phase processes into account had only minute effects on the stability analysis.

From volume scan of radar reflectivity data, the time evolution of precipitation production was computed. The warm frontal snowband generated about two and one-half times more snow than the cold frontal band. Both cases, however, had similar values for the average snow content ( $0.16 \text{ g/m}^3$ ) and the average snowfall rate ( $0.7 \text{ cm/h}$ ). Likewise, times and updrafts required for snow production were similar ( $\sim 32 \text{ min}$  and  $\sim 1.2 \text{ m/s}$ ), suggesting that the same snow formation mechanism occurred in the two snowbands.

## Acknowledgements

I am indebted to the many individuals who provided encouragement and guidance to me during this undertaking. In particular, I wish to thank:

- ♦ Dr. G. W. Reuter, my thesis supervisor. His comments, suggestions and guidance were invaluable and very much appreciated.
- ♦ Mr. Bruno Larochelle, for the many hours spent to familiarize me with the weather radar archive and for the numerous comments and suggestions.
- ♦ My wife, Kitty for her suggestions and patience during this undertaking.
- ♦ Mr. Russ Sampson, for his helpful suggestions.
- ♦ Mr. T. Thompson and Mrs. L. Smith, for their unhesitant and varied support.
- ♦ Environment Canada for supplying data and for the financial support provided during my education leave.

## Table of Contents

1	Introduction	1
1.1	Research topic	1
1.2	Precipitation production in snow storms	4
1.3	Conditional Symmetric Instability	10
1.4	Studies of Alberta precipitation	12
1.5	Statement of the research problems	15
1.6	Thesis layout	15
2	Data and Method of Analysis	17
2.1	The Carvel weather radar	17
2.2	Snow budget analysis from radar data	19
2.3	Errors affecting a snow budget analysis	27
2.4	CSI analysis from sounding data	31
2.5	Assessing CSI from a single sounding	34
3	Analysis of a Warm Frontal Snowband	39
3.1	Introduction	39
3.2	Synoptic overview	41
3.3	Atmospheric stability	46
3.4	Radar analysis	51
3.5	Snow budget at the mature stage	54
3.6	Time evolution of the snow budget	60
3.7	Snow budget sensitivity analysis	65
4	Analysis of a Wide Cold Frontal Snowband	72
4.1	Introduction	72
4.2	Synoptic overview	73
4.3	Atmospheric stability	76
4.4	Radar analysis	81



4.5	Precipitation production .....	85
5	Discussion and Conclusions .....	93
5.1	Summary .....	93
5.2	Comparisons between the two snowbands .....	97
5.3	Comparisons with other studies .....	99
5.4	Discussion .....	101
5.5	Recommendations for further research .....	102
	Bibliography .....	103

## List of Tables

<i>Tables</i>	<i>Contents</i>	<i>Pages</i>
2.1	Carvel radar system characteristics.....	18
3.1	Sounding data for 1200 UTC 16 October 1991.....	50
3.2	Stability analysis of the 1200 UTC 16 October 1991 sounding.....	50
3.3	Snow budget analysis of the mature stage (0800 UTC) warm frontal snowband.....	55
3.4	Snow budget comparison between the snowband and the ambient snow field.....	59
3.5	Variation of snow budget quantities with reflectivity threshold at 0830 UTC.....	68
3.6	Variation of snow budget quantities with the cross-section azimuth angle at 0830 UTC.....	70
3.7	Variation of snow budget quantities with the cloud base height at 0830 UTC.....	71
4.1	Sounding data for 0000 UTC 14 February 1994....	80
4.2	Stability analysis of the 0000 UTC 14 February 1994 sounding data.....	80
5.1	Time average precipitation production values for the warm and cold frontal snowbands.....	98
5.2	Precipitation production comparisons between snowbands and thunderstorms.....	100

## List of Figures

<b>Figure</b>	<b>Contents</b>	<b>Page</b>
1.1	Rainband types in mid-latitude cyclones.....	2
1.2	Schematic of a snow budget for a precipitation system.....	5
2.1	Snowfall rate versus reflectivity factor for various Z-R relations.....	24
2.2	Calculation of cross-sectional area about a radar observation.....	26
2.3	Error propagation in the Z-R relation.....	30
2.4	Finite difference approximation of the Laplacian.....	38
3.1	Snowfall accumulations for 16 October 1991.....	40
3.2	2237 UTC 15 October 1991 IR-satellite image....	40
3.3	Surface analyses for 16 October 1991.....	43
3.4	850 hPa analyses for 16 October 1991.....	44
3.5	500 hPa analyses for 16 October 1991.....	45
3.6	Tephigram analysis for 0000 UTC and 1200 UTC 16 October 1991 sounding data.....	48
3.7	CAPPI 1.5 km radar images from 0700 UTC to 0930 UTC 16 October 1991.....	52
3.8	Reflectivity cross-section at 0830 UTC 16 October 1991.....	54
3.9	Time evolution of snow budget parameters for 16 October 1991.....	61-63
3.10	Outflow and cumulative amount of snow generated by the warm frontal snowband.....	66
4.1	Snowfall accumulations for 13 February 1994....	73
4.2	Surface, 850 hPa, and 500 hPa analysis for 0000 UTC 14 February, 1994.....	74-75
4.3	0220 UTC 14 February IR-satellite image.....	75
4.4	Tephigram analysis for 0000 UTC 14 February 1994 sounding data.....	77

<i>Figure</i>	<i>Contents</i>	<i>Page</i>
4.5	CAPPI 1.0 km radar images from 0100 UTC to 0300 UTC 14 February 1994.....	82
4.6	Reflectivity cross-section at 0200 UTC 14 February 1994.....	84
4.7	Time evolution of snow budget parameters....	89-91
4.8	Outflow and cumulative amount of snow generated by cold frontal snowband.....	92

# 1 Introduction

## 1.1 Research topic

One of the most important functions of an operational weather forecast office is the timely issue of warnings for extreme weather. In winter, the Alberta Weather Centre in Edmonton issues heavy snowfall warnings when forecasts suggest that snow accumulations will exceed 10 cm within a 24 hour period. For central Alberta, about half of the annual precipitation falls as snow (~150 cm), thus predicting the timing, the amount and the distribution of snow from snowfall events is important (Environment Canada 1986).

Significant snowfall events in Alberta are often associated with cyclones that originate from the Pacific (Reinelt 1970; Chung et al. 1976). The conceptual cyclone model advanced by the Norwegian school (Bjerknes 1919; Bjerknes and Solberg 1922) accounts for the formation of a broad uniform shield of precipitation in the pre-frontal region of the warm front and for squall line type bands along the cold front. However, radar observations of precipitation areas associated with mid-latitude cyclones indicate that precipitation bands are common (Nozumi and Arakawa 1968; Browning and Harrold 1969; Browning 1974; Houze et al. 1976a; Hobbs 1978). Since the 1970's, significant effort has been devoted to determining precipitation band characteristics and scales of motion.

The CYCLonic Extratropical Storms (CYCLES) Project (winters of 1973-1978) was the first systematic attempt to investigate the relation between rainbands and large scale processes which produce clouds and precipitation in mid-latitude cyclones (Hobbs et al. 1980). Studies of these cyclones (Houze et al. 1976a,b; Hobbs 1978; Matejka et al. 1980) indicate that rainbands tend to form in preferred

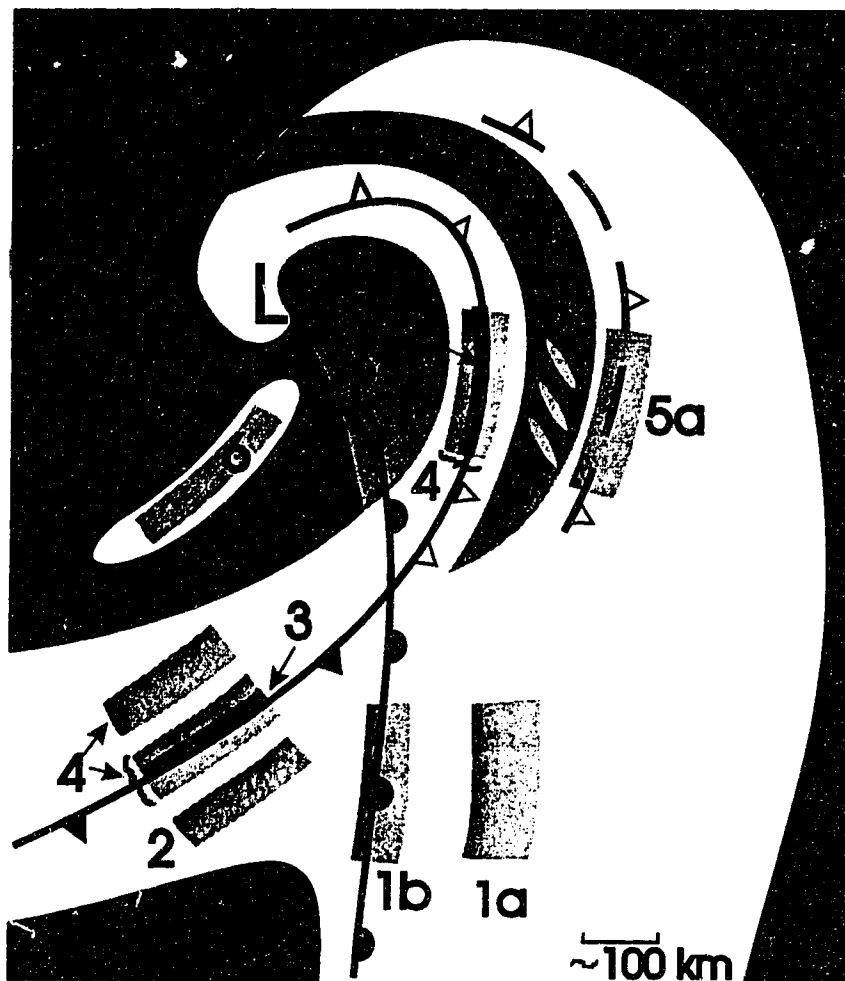


Figure 1.1: Locations of rainband types observed in mid-latitude cyclones. The upper level cloud shield shown in white; lower cloud decks shaded grey.

Type 1a: Warm pre-frontal rainband.

Type 1b: Warm frontal rainband.

Type 2: Warm Sector rainband.

Type 3: Narrow cold frontal rainband.

Type 4: Wide cold frontal rainband (may straddle the narrow cold frontal rainband).

Type 5a: Surge rainband which coincides with a surge of cold air aloft.

Type 5b: Post surge rainband.

Type 6: Postfrontal rainband.

locations and orientations relative to one of the fronts. Six types of rainbands have been identified and are shown in Fig. 1.1 (After Matejka et al. 1980).

A number of mechanisms have been proposed to explain the development of precipitation bands. These include differential temperature advection (Browning et al. 1973), Ekman layer instability (Lilly 1966; Kaylor and Faller 1972), gravity wave ducting (Lindzen and Tung 1976; Bosart and Sanders 1985), frontogenetic forcing (Sanders 1955, 1986), breakdown of horizontal shear across the frontal zone (Solberg 1930; Carbone 1982; Hobbs and Persson 1982), and conditional symmetric instability (Bennetts and Hoskins 1979; Emanuel 1979, 1983a).

Studies of precipitation bands in Alberta (Reuter and Nguyen 1993; Aktary and Reuter 1993) suggest that Conditional Symmetric Instability (CSI) is a likely band formation mechanism. CSI is an instability arising from an imbalance of forces in a baroclinic flow (Bennetts and Hoskins 1979). It manifests as helical roll circulations with the axes parallel to the baroclinic zone. A climatological study of precipitation events in Alberta (Reuter and Aktary 1995) indicated that during the winter months, the potential for CSI existed in 55% of the snowfall events. However, little is known about the characteristics of Alberta snowbands such as life span, resident time for precipitation development and updraft required to maintain the band. These quantities can be determined from weather radar observations of a band's precipitation production, which quantifies the time evolution of a water budget integrated over the precipitation system.

In this thesis two snowfall cases in central Alberta are analyzed. The first event was the Pacific cyclone of 16 October 1991. Radar observations of the pre-frontal region of the warm front indicated the presence of a

snowband which had a life span of about 6 hours. The snowband showed up as an elongated radar echo with a length of about 200 km and a width of about 30 km. For the second event, radar observations indicate snow fell from a number of snowbands the evening of 13 February 1994. The snowbands developed north of a southward moving Arctic cold front and lasted for 3 to 5 hours. Since the snowbands associated with each event formed in different frontal environments, the two snowfall events will be identified as the warm frontal snowband and the cold frontal snowband. Digital radar data are used to examine the time evolution of the precipitation field and its relation to the synoptic airflow. The focus will be on characteristic properties of the snowband based on radar observations of precipitation production. A CSI analysis will also be done to assess its potential for snowband formation. Before precise statements of the thesis problem are made, essential background material will be described.

## 1.2 Precipitation production in snow storms

### a) *Integrated snow budget*

Water that condenses in a storm updraft is either present in the form of cloud, precipitation or has evaporated. The mass  $Q$  that has condensed up to time  $t$  may be written as (Rogers and Yau 1989, pg. 234)

$$Q(t) = E(t) + C(t) + P(t) + O(t) \quad (1.1)$$

where  $C$  is the mass of cloud water at time  $t$ ,  $P$  is the mass of precipitation (snow) aloft,  $O$  is the accumulated mass of precipitation that has reached the ground (total outflow of snow), and  $E$  is the accumulated mass of cloud water and precipitation that has evaporated (Fig. 1.2).  $P$  contains all the snowflakes and large ice particles that fall downwards,



whereas  $C$  contains the small supercooled water droplets and small ice crystals that simply follow the ambient airflow. In the cases analyzed in this study, temperatures values were always below  $0^{\circ}\text{C}$  so that precipitation was exclusively

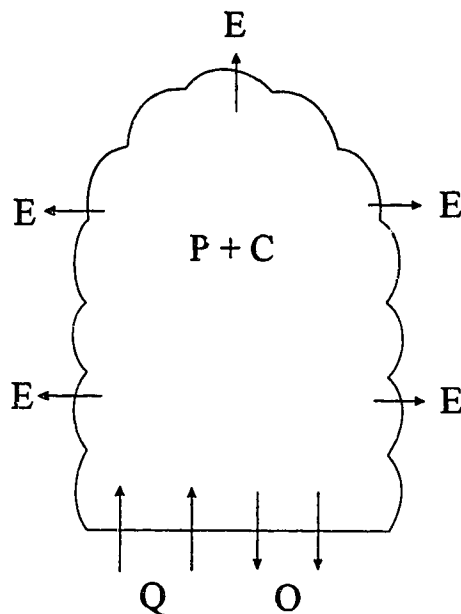


Figure 1.2: Schematic of a snow budget for a precipitation system (See text for symbol definition).

in the form of snow.

Both  $P(t)$  and  $O(t)$  are estimated from a series of radar observations of the precipitation pattern. The value of  $P$  is determined by integrating the snow content  $M$  over the storm volume. Here  $M$  is determined from reflectivity factor  $Z$  using an empirical  $Z$ - $M$  relation. The mass outflow rate through the cloud base  $dO/dt$  at time  $t$  is determined by integrating the snowfall rate  $R$  over the area of the cloud base. Here  $R$  is estimated from  $Z$  using an empirical  $Z$ - $R$  relation. The value  $O$  is determined by integrating  $dO/dt$  over the time period  $0$  to  $t$ . Empirical  $Z$ - $M$  and  $Z$ - $R$  relations are derived using a spectrum of melted snowflakes. Thus  $M$  represents the mass of the melted snow per unit volume and  $R$  represents the melted snow precipitation rate.

The basic assumptions underlying the snow budget equation (1.1) are:

- ♦ Water vapour ascending through the cloud base provides the only source of ice.
- ♦ The vapour is converted into either cloud ice or precipitating ice (i.e. snow) which drifts downwards.
- ♦ No ice is lost through the cloud top or cloud sides.

The two events analyzed in this study are cases where the precipitation field was organized in linear snowbands. The slab-symmetric geometry of such snowbands allows us to consider the snow budget for a cross-section of the snowband with a unit length in the band direction. Due to slab-symmetry, a single vertical cross-section (oriented perpendicular to the band direction) is sufficient to compute the snow budget for a section of the snowband of unit length (e.g. Houze *et al.* 1981). We will now introduce formulas that define  $P$  and  $O$  for a snowband.

From radar measurements of a snowband, a vertical cross-section of digital reflectivity data (oriented perpendicular to the band direction) is used to estimate both  $P$  and  $dO/dt$ . Applying an empirical Z-R relation to data near the cloud base, and integrating across the width of the snowband  $W$  yields an estimate of  $dO/dt$ ,

$$\frac{dO}{dt} = \rho_w \int R dw. \quad (1.2)$$

Here,  $dw$  is the infinitesimal width of the snowband and  $\rho_w$  is the density of water. Likewise, applying an empirical Z-M relation and integrating over the cross-sectional area  $A$  of the snowband yields an estimate of  $P$ ,

$$P = \int M da . \quad (1.3)$$

Here  $da$  is the infinitesimal cross-sectional area of the snowband.

From these quantities, a number of properties can be introduced which further characterize the snowband. The average snowfall rate through the cloud base  $R_{avg}$  and the average snow content in the cloud  $P_{avg}$  are defined by:

$$R_{avg} = \frac{1}{\rho_w} \frac{(dO/dt)}{W} \quad (1.4)$$

$$P_{avg} = \frac{P}{A} . \quad (1.5)$$

Holtz (1968) introduced the concept of characteristic time  $\tau$

$$\tau = \frac{P}{(dO/dt)} . \quad (1.6)$$

The value  $\tau$  represents the time required for all snow located within the snowband to discharge through the cloud base at the mass outflow rate. In periods when  $P$  and  $dO/dt$  are relatively steady,  $\tau$  represents the time needed for snow to develop. Reuter (1990) introduced the characteristic updraft  $U$  given by

$$U = \frac{R_{avg}}{P_{avg}} . \quad (1.7)$$

The value  $U$  represents the average fall speed of the snow within the snowband. When  $R_{avg}$  and  $P_{avg}$  are relatively steady,  $U$  represents the storm updraft required to maintain the average snow content while snow is falling through the cloud base at the average snowfall rate. For this calculation, it

is assumed that there is no mass transport or evaporation of snow through the sides or through the top of the snowband.

Integrating  $dO(t)/dt$  over the time interval 0 to  $t$  gives the accumulated outflow  $O(t)$ . Combined with the total snow content aloft  $P(t)$ , the cumulative amount of snow generated  $G(t)$  is given by the equation

$$G(t) = P(t) + O(t) . \quad (1.8)$$

#### ***b) Past studies***

The systematic study of convective storms started with the Thunderstorm Project (Byers and Braham 1949). One of the fundamental concepts identified during this investigation was the integrated water budget of a thunderstorm cell. Braham (1952) determined that the updraft in a typical airmass thunderstorm cell condenses about 0.5 Gg (1 Gg =  $1 \times 10^6$  kg) of water mass. After this pioneering study, several researchers used radar data to estimate some of the quantities of the integrated water budget:

- a) Holtz and Marshall (1966) used radar data to obtain a total precipitation content of 190 Tg (1 Tg =  $1 \times 10^9$  kg) for a Montreal storm complex.
- b) Holtz (1968), working with the same Montreal storm complex, determined an outflow rate of 47 Gg/s and an accumulated outflow of 379 Tg. Holtz also introduced the concept of characteristic time and the cumulative amount of precipitation generated.
- c) McLaughlin (1967) showed that from an outflow rate of 9.7 Gg/s, the latent heat released by a severe Oklahoma storm was more than a magnitude greater than the estimate determined by Braham (1952).

- d) Barge (1968) determined an average accumulated outflow of 18 Tg for four storms in the Montreal area.
- e) Auer and Marwitz (1968) estimated the rain outflow rate for eight Colorado thunderstorms during their mature stage. The average outflow rate was 1.7 Gg/s.
- f) Pell (1971) reported an average total precipitation content of 1.2 Tg for two storms near Red Deer, Alberta.
- g) From eight intense New England storms, Geotis (1971) determined an average size of 1500 km<sup>3</sup>, an average total precipitation content of 1.7 Tg, an average outflow rate of 0.96 Gg/s, and an average accumulated rainfall of 5.3 Tg. A time history of the rainfall rate was included for one storm.
- h) Fankhauser (1971) determined the time history of the outflow rate and the average rainfall rate for an Oklahoma hailstorm. At the storm's mature stage, an outflow rate of 16 Gg/s and an average rainfall rate of 32 mm/h were observed. By comparing moisture convergence from aircraft wind measurements with the average rainfall rate, the storm had a precipitation efficiency of 60%.
- i) Foote and Fankhauser (1973) determined the time history of the outflow rate for a Colorado hailstorm. The average outflow rate was 2 Gg/s.
- j) Rogers and Sakellariou (1986) introduced the term precipitation production to describe the integrated water budget of a precipitation system. They examined precipitation production in three long lasting Alberta thunderstorms. The most intense storm had a maximum total precipitation content of 1 Tg, a peak outflow rate of 1 Gg/s, a total accumulation of 7 Tg, an

average characteristic time of 25 min and an updraft of about 5 m/s.

- k) Reuter (1990) examined precipitation production in 9 intense thunderstorms that developed over the Lowveld in South Africa. At the storm's mature stage, the most intense storm had maximum total precipitation content of 5.0 Tg, a outflow rate of 2.0 Gg/s, a total accumulation of 10 Tg, a characteristic time of 23 minutes and a characteristic updraft of 5 m/s.

Although precipitation production of a precipitation band has not been determined by radar, the water budget of a rainband has been examined by Houze et al. (1981) using aircraft measurements, atmospheric soundings and rainguage data collected during the CYCLES Project.

### 1.3 Conditional Symmetric Instability

Conditional Symmetric Instability (CSI) is a mesoscale instability that arises from an unstable balance between gravity, the pressure gradient force and the Coriolis force acting on a tube of air oriented along the thermal wind. Bennetts and Hoskins (1979) were the first to suggest that Symmetric Instability may be important in the formation of precipitation bands. They concluded that the conditions required for the realization of dry Symmetric Instability are rarely satisfied in a frontal region. However, the realization of moist Symmetric Instability or Conditional Symmetric Instability (CSI) is possible in a saturated atmosphere. The concept of CSI will be discussed further in chapter 2.

Observational studies have supported the relationships between precipitation bands and CSI (Bennetts and Sharp 1982; Seltzer et al. 1985; Emanuel 1988). Other studies have examined CSI in relation to snowbands.

- a) Emanuel (1983b) analyzed squall lines that occurred in the Oklahoma snowstorm of 2-3 December 1982. Sounding data was analyzed using a single sounding technique for Symmetric Instability.
- b) Sanders and Bosart (1985) analyzed the snowstorm of 11-12 February 1983 which produced a snowband from North Carolina to New England. For this event the snowband could be attributed to thermally direct circulation induced by frontogenetic forcing. CSI was thought to enhance the ascent of the circulations (Emanuel 1985) resulting in pulse-like eruptions of the elevated cloud tops.
- c) Wolfsberg et al. (1986) analyzed the 11 December 1982 New England snowstorm. They found that CSI could explain many of the observed features of the bands such as their alignment and slope.
- d) Moore and Blakley (1988) analyzed the Midwest snowstorm of 30-31 January 1982 which showed similar behaviour to the Sanders and Bosart (1985) study.
- e) Byrd (1989) showed that CSI was an important mechanism in overrunning banded precipitation events over the southern plains of the United states during 1981-1982.
- f) Donaldson and Stewart (1989) suggested that CSI may have been a contributing factor in the development of snowbands in two Atlantic storms during the winter of 1986.
- g) Reuter and Yau (1990) studied seven precipitation bands during the Canadian Atlantic Storms Program (CASP). CSI was found to be realized in the lower part of the atmosphere resulting in banded precipitation.

- h) Shields et al. (1991) analyzed the Midwest snowstorm of 10-11 February 1988. They found CSI existed above the cold frontal zone, but the snowbands observed along the cold front were attributed to frontogenetic forcing.

#### 1.4 Studies of Alberta precipitation

The Rocky Mountain range is a formidable barrier which stretches from the Mackenzie Delta in the Northwest Territories to southern Texas. The weather circulation pattern is affected by this barrier which in turn affects the timing and the distribution of precipitation across Alberta (Reinelt 1970). In westerly mid-tropospheric flows, subsidence to the lee side of the mountains will "wring" out moisture from disturbances as they cross the mountains. With a downward slope of the terrain from west to east, low level easterly winds will produce upslope conditions which often enhance precipitation over western Alberta. The annual precipitation amount in the Prairie regions of eastern Alberta is about 300 mm, whereas the foothills and mountains receive about 400 mm or more.

The slope of the terrain can also affect the development of precipitation systems. Significant precipitation events in Alberta tend to occur when a Pacific cyclone dissipates along the west coast of British Columbia and reforms over western Alberta by lee cyclogenesis (Chung et al. 1976). Summertime differential heating of the eastern slope of the Rockies can also produce extensive outbreaks of convection (Smith and Yau 1987).

Significant effort has gone into understanding thunderstorms, but at the expense of nearly ignoring synoptic events and precipitation bands. Studies of all three types of precipitation systems are now reviewed.



**a) Summertime Convection**

Studies of severe storms in Alberta began in the 1960's with the installation of a 10 cm S-band polarization radar in Penhold, Alberta (52.2°N, 113.8°W, 904 m). Besides researching severe storms, the radar was also used to study hailstone growth and to evaluate the effectiveness of weather modification. The major findings for summertime convection are documented in:

- a) Formation of hail (Longley and Thompson 1965).
- b) Quantitative hailstorm studies (Pell 1971).
- c) Multicell hailstorms (Chisholm and Renick 1972).
- d) Growth of individual hail stones (English 1973).
- e) Climatology of hail (Wojtiw 1975).
- f) Forecasting of hailstorms (Renick and Maxwell 1977).
- g) Distribution of hailstone sizes (Cheng and English 1983).
- h) Supercell hailstorms (Krauss and Marwitz 1984).
- i) Water budget of hailstorms (Rogers and Sakellariou 1986).
- j) Mesoscale upper air analysis (Strong 1989).
- k) Polarized radar estimates of heavy rainfall rate (English et al. 1991).
- l) Hail identification using polarization radar (Al-Jumily et al. 1991).
- m) Aerial precipitation amounts from radar (Kochtubajda 1991).
- n) Causes of severe convection (Smith and Yau 1993a,b).
- o) Severe storm structure from polarization and Doppler (Carvel radar) observations (Holt et al. 1994).

With the improvements in the weather radar system at Carvel (53.34°N, 114.09°W, 783 m) in 1991, digital radar is now incorporated into studies of summertime convection in central Alberta. Larochelle (1994) developed a synthetic dual Doppler technique for viewing a thunderstorm's horizontal wind field, and applied it to a meso-cyclone that spawned a tornado.

***b) Synoptic precipitation***

Much less effort has been devoted to the study of synoptic precipitation in Alberta. With significant precipitation events occurring during the passage of a Pacific cyclone, research has focused on lee cyclogenesis with an emphasis on its climatology and typical storm tracks (Chung et al. 1976; Vickers 1975). Case studies of the snow distribution from Pacific cyclones have also been undertaken by the weather office in Edmonton (Gendron 1991; Larochelle 1991).

***c) Precipitation bands***

Until recently, there has been little interest in Alberta precipitation bands. Reuter and Nguyen (1993) analyzed multiple rainbands that formed in the 17 July 1986 rainstorm. An analysis of the Stony Plain sounding indicated that potential for CSI existed in a layer between 600 hPa and 400 hPa. Aktary and Reuter (1993) observed a snowband during the 4 October 1990 snowstorm in central Alberta. Potential for CSI existed in a layer between 700 hPa and 500 hPa.

### 1.5 Statement of the research problems

The aim of this thesis is to document the integral parameters of the snow budget derived from radar measurements of a warm frontal and a cold frontal snowband. The main objective of this study is to determine the feasibility of using the Carvel radar to determine portions of a snowband's integrated snow budget. Assuming slab-symmetry, snow budget properties will be determined from a vertical cross-section of digital reflectivity data obtained perpendicular to the snowband. Budget properties include the total snow content, the mass outflow rate, the average snow content, the average snowfall rate, the characteristic time, the characteristic updraft and the total mass of snow generated. The relationship between the synoptic conditions and the development of the snowband will also be examined. The assumption of band slab-symmetry will be verified through a sensitivity study of the cross-section angle.

A second objective of this thesis is to determine the potential for the existence of Conditional Symmetric Instability in the two cases. The potential for CSI will be assessed from atmospheric sounding data collected at Stony Plain (53.33°N, 114.06°W, 766 m) using a single sounding technique (Emanuel 1983b; Seltzer et al. 1985). The results will be compared to a vertical cross-section of reflectivity normal to the snowband.

### 1.6 Thesis layout

The approach taken here will be to analyze digital reflectivity data from the Carvel radar and data sampled by radiosondes from Stony Plain.

Chapter 2 will give the necessary background information on the sources of data used in this study. The

method is split into 2 sections. The first will explain how to determine the integrated snow budget from a volume scan of reflectivity data. A discussion of the errors affecting this method will also be included. The second section will give a brief explanation of the theory of CSI and how to determine the potential for CSI using a single sounding technique.

Chapters 3 and 4 will determine the snow budget as well as the potential for CSI for the warm and the cold frontal snowbands, respectively. The synoptic conditions and the distribution of snowfall will also be discussed for each event. Additionally, in chapter 3 a sensitivity analysis of the snow budget will be presented.

Chapter 5 will summarize and compare the findings of this thesis with other studies. The results will then be synthesized into final conclusions, along with some suggestions for future research.

## 2 Data and Method of Analysis

### 2.1 The Carvel weather radar

The Alberta Weather Centre in Edmonton operates a Doppler weather radar located in Carvel, Alberta (53.34°N, 114.09°W, 783 m). The radar collects both conventional data (reflectivity) and Doppler data (velocity, spectral width) sampled over 10 minutes. The primary purpose of this radar is to support weather forecast operations at the Alberta Weather Centre. It provides graphical displays of precipitation measurements, such as Constant Altitude Plan Position Indicator (CAPPI) imagery. Since this study will not be using Doppler data, the discussion will focus on the conventional data.

Reflectivity measurements of precipitation are determined from the emission of pulsed electromagnetic energy which is focused by the radar antenna into a narrow beam. A portion of the transmitted energy is back-scattered by precipitation particles. The receiver within the antenna collects this energy and converts it to a reflectivity factor  $Z$  which is proportional to the sum of the particle diameters to the sixth power over a unit volume ( $\text{mm}^6/\text{m}^3$ ). Reflectivity factor is usually expressed in dBz (i.e.  $Z(\text{dBz}) = 10\log(Z)$ ). By sending pulses of energy at the pulse repetition frequency,  $Z(\text{dBz})$  values can be determined over a number of pulse volumes. A pulse volume is a fulstrum that is bounded by the range resolution and the radar beam width. To improve the accuracy of the  $Z(\text{dBz})$ , a number of pulse volume measurements are integrated in space to determine an average value. The spatial volume over which samples are integrated are referred to as range bins. Integrating conventional data over 1 km range bins provides an accuracy of  $\pm 1$  dBz. Some of the technical characteristics of the

Carvel radar are given in Table 2.1. More details are available in Crozier (1986).

Table 2.1: System characteristics for the Carvel radar. After Crozier (1986).

Parameter	Conventional	Doppler
Disk diameter (m)	3	3
Peak power (kw)	260	260
wavelength (cm)	5.34	5.34
frequency (MHz)	5625	5625
Azimuthal beam width (degrees)	2.2	1.4
Elevation beam width (degrees)	1.1	1.1
Scanning rate (rpm)	6	0.75
Pulse duration ( $\mu$ s)	2	0.5
Pulse repetition frequency (Hz)	250	1190 and 892
Range resolution (m)	300	75
Range bin length (km)	1	0.5
Max. observed range (km)	256	113
Elevation scan angles (degrees)	24 angles from 0.4 to 24.6	0.4, 0.5, 1.5, 3.5

In order to collect radar data in an efficient manner (i.e. 28 scans required in a 10 minute period), the radar scans continually in azimuth  $\theta$  and steps to a new elevation angle  $\emptyset$  after each rotation. After the data is processed and graphical displays are produced, the digital measurements (both Doppler and conventional) and the images are archived on optical disks at the radar site. Digital data are stored in spherical co-ordinates ( $r, \theta, \emptyset, t$ ) where  $r$  is the slant range to the target and  $t$  is the sample time. Due to the large volume of data collected by each scan, measurements are compressed using a routine that stores data from locations where echoes occurred (Crozier 1986). For conventional data, values are only archived if they are above a minimum reflectivity of 7 dBz.

To acquire data from the archive, files are loaded from the optical disks to the computer at the radar site. These files, up to two megabytes in size, are then downloaded to a personal computer by a modem. I have written a program in C-language to uncompress the digital reflectivity data.

For  $Z(\text{dBz})$  measurements of snow, an adjustment to the data is needed since the radar is set for rain measurements. The ice reflectivity factor  $Z_i(\text{dBz})$  is determined by (Sauvageot 1992, pg. 113)

$$Z_i(\text{dBz}) = Z(\text{dBz}) + 6.5(\text{dB}) . \quad (2.1)$$

Correction of  $Z_i(\text{dBz})$  data for attenuation is not required. Attenuation reduces the intensity of the radar signal as it passes through the atmosphere. The attenuation of the radar beam by snow is about one-tenth that produced by rain and can be neglected unless there are high  $Z_i(\text{dBz})$  values ( $\sim 3 \text{ dBz}$ ) over a large distance ( $\sim 50 \text{ km}$ ) (Gunn and East 1954).

## 2.2 Snow budget analysis from radar data

This section will address the method required to determine a snow budget from conventional radar data.  $Z_i$  can be used to provide estimates of the total snow content aloft  $P$  (equation 1.1) and the mass outflow rate  $dO/dt$  using empirical  $Z_i$ - $M$  and  $Z_i$ - $R$  relations, respectively.

Assuming that the geometry of the snowband is slab-symmetric,  $P$  and  $dO/dt$  can be estimated from a vertical cross-section of  $Z_i$  oriented perpendicular to the band length. By taking a vertical cross-section along a fixed azimuth angle  $\theta$ , the co-ordinate system of the  $Z_i$  data is simplified to  $(r, \phi, t)$ . To ensure good  $Z_i$  data resolution and to minimize the amount of precipitation lost above and below the highest and the lowest radar elevation angles, a

snowband vertical cross-section is limited to a distance between 10 km and 60 km from the radar.

Prior to explaining the method for estimating the snow budget quantities, the problems of  $Z_1$  data corrections for ground clutter, band identification, the cloud base height, and missing data will be addressed. Following this, the snow budget method and the errors associated in using this method will be discussed.

**a) Removal of ground clutter**

When the radar beam scans at low elevation angles (of less than approximately  $3^\circ$ ), ground echoes can occur with meteorological echoes. These ground echoes called ground clutter can be caused by hilly terrain or by temperature inversion close to the earth's surface. A temperature inversion can cause the radar beam to refract back towards the earth's surface. Ground clutter can be easily identified in a vertical  $Z_1$ (dBz) cross-section as spikes of approximately 45 dBz.

To eliminate possible contributions of ground clutter to a snow budget analysis, ground echoes are recorded when atmospheric echoes are absent.  $Z_1$ (dBz) data at these ranges and elevations are then removed from the analysis (Sauvageot 1992, pg. 204).

**b) Band identification**

A snowband can be embedded in an area of snow resulting from thick layers of nimbostratus. To identify the band at various stages, a reflectivity threshold  $Z_t$ (dBz) has to be chosen to distinguish the snowband from the ambient snow. To find  $Z_t$ (dBz), a vertical cross-section of  $Z_1$ (dBz) is interpolated to a Cartesian grid using Cresman's (1959) interpolation (e.g. Haltiner and Williams 1980, pg. 356). Contouring the Cartesian grid data,  $Z_t$ (dBz) is found from



the contour value which defines the boundary of the snowband. For the warm and cold frontal snowbands, a  $Z_e$  (dBz) value of 25 dBz and 20 dBz were used, respectively.

*c) Cloud base height*

To determine the snow budget parameters  $dO(t)/dt$  and  $P(t)$ , the height of the snowband's cloud base relative to the radar site is required. Since hourly synoptic observations are not taken at the radar site, the AGL (above ground level) height of the snowband's cloud base is determined from hourly synoptic observations. Observations from the Edmonton Municipal Airport (53.34°N, 113.31°W, 671 m) or the Edmonton International Airport (53.19°N, 113.35°W, 715 m) are used. Since moderate snowfalls (0.8 cm/h to 1.6 cm/h) can produce false precipitation ceilings, the height of the cloud base was chosen from a report when the edge of the snowband observed on radar was close to the airport. To account for a possible lower cloud base at the centre of the snowband and for the elevation difference of about 70-110 m between the airport and the radar site, the cloud base height is lowered by 300 m and rounded to the nearest 100 m.

To exclude  $Z_e$  (dBz) data below the cloud base in the snow budget analysis, the height of the radar beam at each range bin is determined. Since the density of air changes with height, the resulting change in the index of refraction causes the radar beam to curve. For a standard atmosphere, the curvature of the beam can be accounted for by increasing the earth's diameter by 4/3 (Battan 1973, pg. 24). The height of the radar beam  $H$ , in metres, above the earth's surface is then (Mohr and Vaughan 1978)

$$H = z + \left[ \frac{d^2}{\frac{4}{3}D} \right], \quad (2.2)$$

where  $d$  is the horizontal distance to the radar bin in metres, and  $z$  is the height of the radar bin in metres above the zero degree radar elevation angle (i.e.  $z = r \sin(\theta)$ ). The value  $D$  is the earth's diameter (12,730 km) at the radar site (Meeus 1988).

Since a standard atmosphere (Wallace and Hobbs 1977, pg. 23) is assumed in equation 2.2,  $H$  can only be considered an approximation. However, compared to other studies of precipitation production (Rogers and Sakellariou 1986; Reuter 1990) where a low radar elevation scan angle is used to approximate a horizontal surface below the cloud base, the use of  $H$  should be an improvement.

#### *d) Missing data*

For this study, a snowband has a typical cloud base and cloud top of 500 m and 5000 m AGL, respectively. With the radar scanning in a geometric progression from  $0.4^\circ$  to  $24.6^\circ$  (Crozier 1986) portions of the snowband could lie outside this scanning range. The height of the lowest scan angle will lie above the typical cloud base beyond 45 km. To include the possible contributions of this unobserved precipitation, it is assumed that the reflectivity in any vertical column is constant from the lowest altitude of observation down to the cloud base level. Thus missing observations are approximated by

$$Z(r, 0.2^\circ, t) = Z(r, 0.3^\circ, t) = Z(r, 0.4^\circ, t) . \quad (2.3)$$

Between the radar range of 10 km to 15 km, the height of the radar beam at the highest elevation angle will lie below the typical cloud top. The amount of precipitation contained in this range with a beam height between 4.5 km and 6 km is small compared to the whole snowband. Thus in the cases

considered, no adjustment was required to the vertical cross-section of the snowband.

**e) Assessment of the mass outflow rate**

To determine the mass outflow rate  $dO/dt$  from  $Z_i$  (dBz) cross-section values, the values of  $Z_i$  (dBz) are first converted to  $Z_i$  ( $mm^6/m^3$ ) by the relation

$$Z_i(dBz) = 10 \log(Z_i(mm^6/m^3)) . \quad (2.4)$$

The snowfall rate  $R$  is determined from an empirical  $Z_i$ - $R$  relation for dry snow. A few  $Z_i$ - $R$  relations for dry snow are:

- a)  $Z_i = 2150 R^{1.8}$  derived from snow measurements over a 1 hr 40 min period (Imai et al. 1955),
- b)  $Z_i = 2000 R^2$  derived from snow measurements over a 10 day period (Gunn and Marshall 1958),
- c)  $Z_i = 1780 R^{2.21}$  derived from snow measurements from four previous studies (Sekhon and Srivastava 1970).

A plot of the three  $Z_i$ - $R$  relations (Fig. 2.1) shows only a small difference below 45 dBz, thus Sekhon and Srivastava's (1970) relation will be used since it is based on a number of data sets. Re-writing their relation in terms of  $R$  gives

$$R = \left( \frac{Z_i}{1780} \right)^{0.4525} . \quad (2.5)$$

Here  $R$  is expressed as the melted snowfall rate in mm/h of liquid water. Since the density of dry snow is about one tenth the density of liquid water,  $R$  can also be interpreted as the snowfall rate in cm/h.  $R$  is determined for every

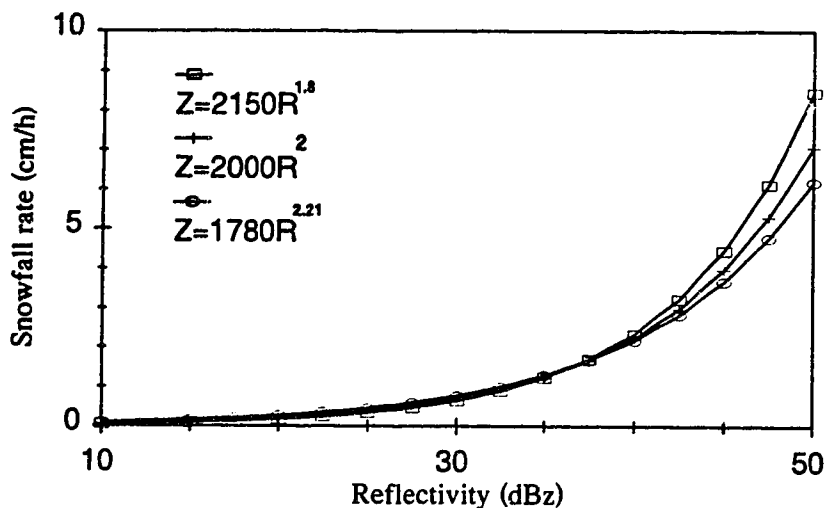


Figure 2.1: Snowfall rate  $R$ (cm/h) versus reflectivity factor  $Z_1$ (dBz) for different empirical  $Z_1$ - $R$  snow relations.

$Z_1$ (dBz) value in the snowband cross-section and is set equal to zero if  $Z_2$ (dBz) falls below  $Z_t$ (dBz).

The mass outflow rate through the cloud base,  $dO/dt$  (equation 1.2), in  $Mg/s km^{-1}$  (1 Mg =  $10^3$  kg) is approximated by

$$\frac{dO}{dt} \approx 2.78 \times 10^{-4} \sum_j \rho_w \cdot R_j \cdot \Delta w_j . \quad (2.6)$$

Here  $\rho_w$ (Mg/m<sup>3</sup>) is the density of water and  $\Delta w_j$  is the horizontal width of radar bin  $j$ . For cloud bases below 600 m AGL,  $\Delta w_j$  can be approximated as 1000 m (between 10 km and 20 km from the radar, the width of the bin is 999 m).

Integrating  $\Delta w_j$  gives the width in metres of the snowband  $W$

$$W = \sum_j \Delta w_j . \quad (2.7)$$

The average snowfall rate  $R_{avg}$  in cm/h is given by

$$R_{avg} = 3600 \frac{1}{\rho_w} \left( \frac{dO/dt}{W} \right). \quad (2.8)$$

**f) Assessment of the total snow content aloft**

Based on the empirical  $Z_1$ -R relation for dry snow, Sekhon and Srivastava (1970) derived an empirical M-R relation

$$M = 0.250R^{0.86}, \quad (2.9)$$

where M is the snow content in g/m<sup>3</sup>. The total snow content aloft P (equation 1.3), in Gg/km (1 Gg = 1x10<sup>6</sup> kg) is approximated by

$$P \approx 1x10^{-6} \sum_j M_j \cdot \Delta a_j. \quad (2.10)$$

Here  $\Delta a_j$  in m<sup>2</sup> is the cross-sectional area around each radar bin  $j$  and is given by (Donald 1983, pg. 409)

$$\Delta a_j = \frac{1}{2} \left[ r_{n+\frac{1}{2}}^2 - r_{n-\frac{1}{2}}^2 \right] \Delta \theta. \quad (2.11)$$

The value  $r_n$  is the range to the radar bin  $n$  and  $\Delta \theta = \frac{1}{2}(\theta_{p+1} - \theta_{p-1})$ , where  $\theta_p$  is the elevation angle in radians of the radar observation (Fig. 2.2). When M values are observed along the highest elevation angle,  $\Delta \theta$  is determined using a radar beam width of 1.1°. Integrating  $\Delta a_j$  gives the cross-sectional area A of the snowband

$$A = \sum_j \Delta a_j. \quad (2.12)$$

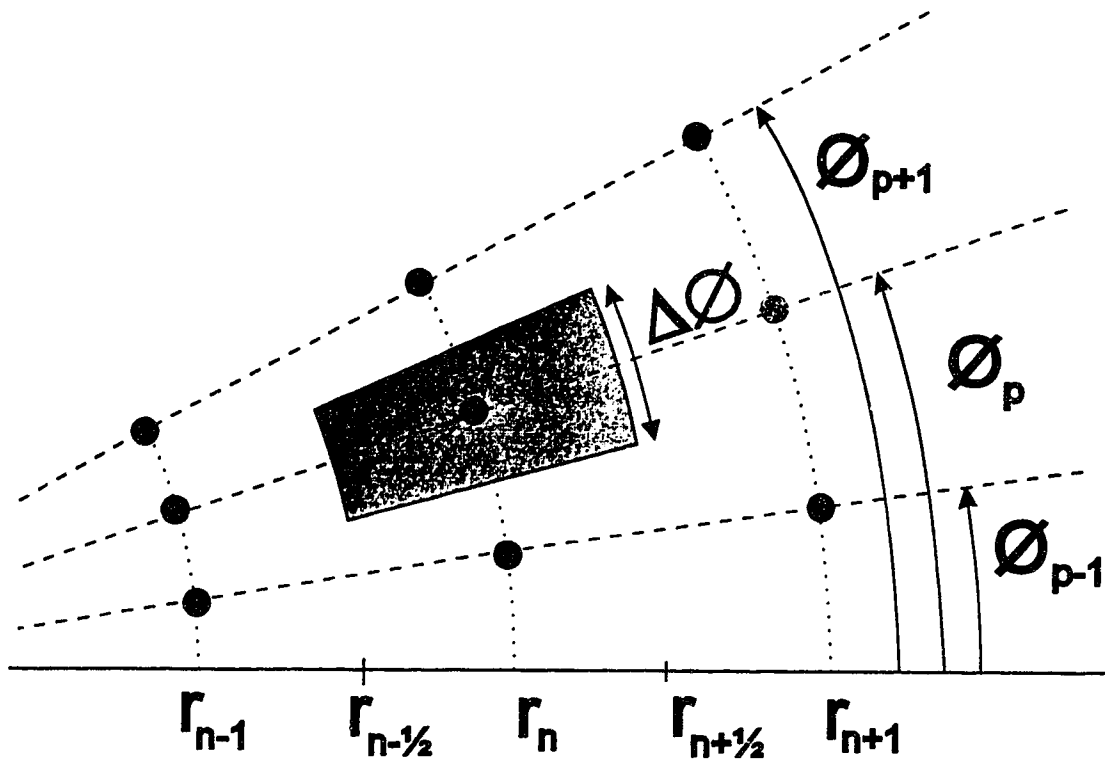


Figure 2.2: Cross-sectional area (shaded grey) about a radar observation (black dot). Observation (n, p) given by slant range r and by the radar elevation angle  $\phi$ .

The average snow content  $P_{avg}$  in  $g/m^3$  is

$$P_{avg} = 1 \times 10^6 \left( \frac{P}{A} \right). \quad (2.13)$$

**g) Characteristic properties and snow generated**

Other properties can be found which further characterize the snowband. The characteristic time  $\tau$  in minutes and the characteristic updraft  $U$  in m/s are given by

$$\tau = 16.67 \frac{P}{(dO/dt)}, \quad (2.14)$$

$$U = 0.28 \left( \frac{R_{avg}}{P_{avg}} \right). \quad (2.15)$$

The accumulated outflow  $O(t)$  of the snowband over the analysis time period from 0 to  $t$  can be estimated through finite differencing

$$O(t) = \int_0^t \left( \frac{dO}{dt} \right) dt \approx \sum_{k=1}^t \left[ \frac{(dO/dt)_k + (dO/dt)_{k-1}}{2} \right] \Delta t, \quad (2.16)$$

where  $\Delta t$  is the time step (10 minutes) and  $k$  is the time interval. At  $t=0$ , the accumulated outflow from the snowband is zero. The generation rate of snow accumulated from time 0 to  $t$  is

$$G(t) = P(t) + O(t). \quad (2.17)$$

### 2.3 Errors affecting a snow budget analysis

The accuracy of the snow budget parameters can be affected by errors in  $Z_1$  (dBz) values, in the  $Z_1$ -R relation, and in integrated properties.

#### a) Factors affecting $Z_1$ measurements

A number of factors can affect the determination of  $Z_1$  (dBz), including instrumentation error, integration of the digital reflectivity measurements, partial beam filling, ground clutter, radar calibration, side lobes and attenuation.

Values of  $Z_1$  (dBz) are obtained from integrating reflectivity measurements over a number of pulse volumes. From instrumentation error (i.e. the digital integrator at the radar site), the integrated  $Z_1$  (dBz) value will have an uncertainty of  $\pm 1$  dBz. Zawadzki (1973) indicated that integrating and averaging of radar data increases the

precision of the reflectivity measurements. However, this increase in precision comes with a loss of spatial resolution and a loss of detecting extreme reflectivity values. If averaging is not performed, Rogers (1971) showed that a maximum error of  $\pm 5$  dBz can occur in the pulse volume measurement of  $Z_1$ (dBz).

The largest factor affecting the measurement of  $Z_1$ (dBz) is partial beam filling. In the radar equation (Probert-Jones 1962) it is assumed that the radar pulse volume is completely filled with a homogeneous spectra of precipitation particles. If the radar beam is partially filled, the radar will include this "null region" in determining the reflectivity value over the pulse volume. Partial beam filling occurs along the edges of a precipitation system. This becomes more significant with distance from the radar due to the widening of the radar beam. The reflectivity threshold helps to reduce the effects of partial beam filling since it is more likely that a partially filled radar beam will produce a  $Z_1$ (dBz) value below this threshold. From modelling the observation of a rain cell by space born radar, Amayenc et al. (1989) indicated that if the cell was at least twice the beam width of the radar, the error in  $Z$ (dBz), due to partial beam filling, is 10% to 20%. With a beam width of approximately 0.5 km over a distance of 10 km to 60 km from the Carvel radar, the error in  $Z_1$ (dBz) for a snowband should also be about 20%.

Errors in  $Z_1$ (dBz) due to attenuation, side lobes, radar calibration drift and ground clutter are likely to be less important or can be corrected in the  $Z_1$ (dBz) data. Attenuation and ground clutter have already been discussed in sections 1 and 2. The Carvel radar has a self calibration routine that runs on a daily basis, thus the error in  $Z_1$ (dBz) due to calibration drift is negligible.



Contributions to  $Z_1(\text{dBz})$  from side lobes (i.e. secondary lobes within the radiation pattern radiated by the antenna) can be ignored unless the reflectivity exceeds 40 dBz or the  $Z_1(\text{dBz})$  examined is within 5 km of the radar (Battan 1973).

**b) Factors affecting the  $Z_1$ -R and R-M relations**

Besides the  $Z_1(\text{dBz})$  error of approximately 20% propagating into M and R, there are errors in M and R due to local variations in the spectra of precipitation particles. However, the error in R and M would be negligible unless wet snow or rain is measured.

To determine the effect of a  $Z_1(\text{dBz})$  error on R, error ratios are considered. From Sekhon and Srivastava's empirical  $Z_1$ -R relation, the ratio  $R_m/R$  can be determined for a  $Z_m(\text{dBz})/Z_1(\text{dBz})$  ratio

$$\frac{R_m}{R} = \left( 10^{0.1(Z_m(\text{dBz}) - Z_1(\text{dBz}))} \right)^{0.4525}, \quad (2.18)$$

where  $Z_m$  and  $R_m$  are the maximum values achieved when the error is added to  $Z_1$  and R respectively. For example, a 20% error in  $Z_1(\text{dBz})$  will give  $Z_m(\text{dBz}) = 1.20 Z_1(\text{dBz})$ . A plot of  $R_m/R$  verses  $Z_m(\text{dBz})/Z_1(\text{dBz})$ , Fig. 2.3 indicates that the error in R is a function of both the size of  $Z_m(\text{dBz})/Z_1(\text{dBz})$  and of the initial  $Z_1(\text{dBz})$  value. For instance, a 20% error in  $Z_1(\text{dBz})$  will cause R to be in error by a factor of 2 at 35 dBz. Thus the error in  $Z_1(\text{dBz})$  is much more significant than the error associated with the fixed  $Z_1$ -R relation selected.

Similarly, an error ratio can be derived for the precipitation content M, but since M is a function of R (equation 2.9), the magnitude of the error in M will be similar to that of R.

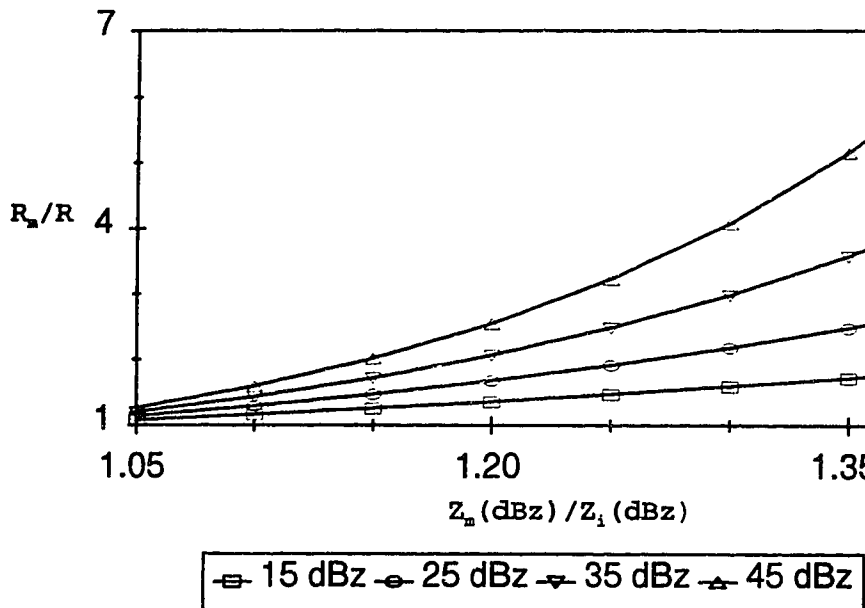


Figure 2.3: Ratio of maximum error in the snowfall rate  $R$  versus the ratio of the maximum error in  $Z_i(\text{dBz})$  for different initial  $Z_i(\text{dBz})$  values.

### c) Factors affecting integrated properties

Besides local errors in  $Z_i(\text{dBz})$  propagated into the integrated snow budget parameters, the removal of  $Z_i(\text{dBz})$  data due to ground clutter, and the loss of  $Z_i(\text{dBz})$  due to  $Z_t(\text{dBz})$  will also affect snow budget parameters. The effects of removing ground clutter and the effects of different  $Z_t(\text{dBz})$  on budget quantities will be case dependent. A sensitivity analysis in chapter 3 will address these problems.

The error in  $Z_i(\text{dBz})$  due to partial beam filling will have the largest affect on  $R$  and  $M$  values. Integration of  $R$  and  $M$  values to determine  $dO/dt$  and  $P$ , respectively will smooth out some of their local errors. Errors in  $dO/dt$  and  $P$  can be reduced further by averaging. The distribution of errors in  $Z_i(\text{dBz})$  and the error caused by partial beam filling are not fully known for a snowband, thus error

propagation techniques cannot directly be applied to this integration (Bevington 1969). Based on the partial beam filling study by Amayenc et al. (1989), the likely error in integrated properties is at least 20% and may be as high as 100% in some cases.

#### **2.4 CSI analysis from sounding data**

Symmetric Instability is a two-dimensional instability which manifests itself as helical roll circulations in a baroclinic atmosphere. It results from an unstable balance between gravity, the pressure gradient force and the Coriolis force acting on a tube of air oriented along the thermal wind (Emanuel 1983a). Most frontal zones are stable to dry Symmetric Instability but in a saturated atmosphere, the latent heat released within the rising tube of air can assist moist Symmetric Instability (Bennetts and Hoskins 1979). This moist Symmetric Instability is often referred to as Slantwise Convective Instability or Conditional Symmetric Instability (CSI). The basic theory of CSI has been well laid out in research papers (Bennetts and Hoskins 1979; Emanuel 1983a,b) and in textbooks (Ray 1986; Cotton 1990; Rogers and Yau 1989). Prior to explaining the method required to determine the potential for CSI, the data source used for the analysis and the conditions required for the release of CSI must be examined.

##### **a) Database used for CSI analysis**

Atmospheric sounding and maps (i.e. surface and height analysis charts) were acquired from the Climate Section associated with the Edmonton Weather Centre. Atmospheric sounding data is collected twice daily (00 UTC and 12 UTC) using a balloon radiosonde system located at Stony Plain, Alberta (53.33°N, 114.06°W, 766 m). This sounding system

collects pressure, temperature, height, relative humidity, and wind velocity.

**b) Conditions for CSI**

A number of conditions are required before CSI can be realized in the atmosphere. These include:

- a) The stratified flow is locally two-dimensional, with most variations in the thermodynamic and kinematic properties occurring in the cross-flow direction.
- b) The flow is in hydrostatic and in geostrophic balance.
- c) The airmass is saturated with respect to water or ice.
- d) There should be a region in the atmosphere where the moist Richardson number  $Ri_m$  (Seltzer et al. 1985) is less than 1.

The moist Richardson number is calculated using

$$Ri_m \equiv \frac{\eta}{f} N_m^2 \left( \frac{\partial v_g}{\partial z} \right)^{-2} \equiv \frac{\eta \Gamma_m}{f \Gamma_d \theta_{ref}} \frac{g}{\partial \theta_e}{\partial z} \left( \frac{\partial v_g}{\partial z} \right)^{-2} < 1. \quad (2.19)$$

The Cartesian co-ordinate system  $(x, y, z)$  used in equation (2.19) has the  $y$  axis oriented in the direction of the geostrophic wind shear, the  $x$  axis normal to the shear (pointing towards warmer air) and the  $z$  axis pointing upwards. Here  $\partial v_g / \partial z$  denotes the vertical shear of the geostrophic wind, where  $v_g$  is the  $y$  component of the geostrophic wind.  $\eta$  is the vertical component of the absolute vorticity ( $\eta = f + (\partial v_g / \partial x)$ ), where  $f$  is the Coriolis parameter.  $N_m$  is the moist Brunt-Väisälä frequency (Durran and Klemp 1982), where  $\theta_e$  is the equivalent potential temperature,  $\theta_{ref}$  is a reference equivalent potential temperature, and  $g$  is the gravitational acceleration. The

values  $\Gamma_d$  and  $\Gamma_m$  are the dry and moist adiabatic lapse rates, respectively.

Emanuel (1983a) and Xu and Clark (1985) stressed that Convective Instability is a special case of CSI. Convective Instability arises when a layer of moist air of finite depth is lifted vertically (Rogers and Yau 1989, pg. 33). The criteria for the release of Convective Instability when a layer is lifted to saturation is

$$\frac{\partial \theta_e}{\partial z} < 0. \quad (2.20)$$

When the atmosphere satisfies the condition in (2.20), it will also satisfy the condition for the release of CSI (2.19). With different time scales for each type of instability, a few minutes for Convective Instability and a few hours for CSI (Bennetts and Hoskins 1979), one would expect all the Convective Instability to be released before CSI occurs. However, studies have shown that CSI and Convective Instability can co-exist (Jascourt et al. 1988; Reuter and Yau 1993).

When applying CSI theory to the real atmosphere, some caution is required. When the atmosphere is moist but not saturated, CSI can only be realized when the airmass is lifted to saturation. Thus only the potential for CSI can be examined. CSI theory requires that the wind be unidirectional in the layer under investigation. Friction and viscous stress forces should also be small compared to the pressure gradient forces. At the Stony Plain upper air station, the planetary boundary layer, where frictional and viscous stress forces are typically significant, extends from the surface to about 850 hPa.

## 2.5 Assessing CSI from a single sounding

Techniques have been developed to analyse CSI from a group of soundings (Emanuel 1983b). However, with a distance of 500-700 km to the nearest atmospheric sounding station from Stony Plain, this technique is not feasible for Alberta. Seltzer et al. (1985) showed that the potential for CSI can be assessed from a single sounding using the moist Richardson number  $Ri_m$ . This technique has been used in other studies to assess CSI potential (Seltzer et al. 1985; Donaldson and Steward 1989; Reuter and Nguyen 1993; Aktary and Reuter 1993; Reuter and Aktary 1995). In these cases, the thermodynamics in (2.19) were determined for the liquid water phase. Since the temperatures were below zero for the two snow events, it is of interest to use ice phase thermodynamics.

Based on the CSI criteria given in (2.19),  $Ri_m$  can be assessed for an atmospheric sounding. Since sounding data annotates height in the atmosphere through pressure  $p$ , the atmosphere can be broken up into layers of finite thickness  $\Delta p$ . To characterize the mesoscale flow, Aktary and Reuter (1993) and Reuter and Nguyen (1993) determined  $Ri_m$  about every 100 hPa. Instead of breaking up the sounding at fixed pressure levels, layers will be separated by distinct temperature inflections. There are two criteria required for breaking up the sounding this way. First, the resultant layer must be greater than 50 hPa thick to prevent the analysis of small scale eddies in the flow. Second, the effects of the planetary boundary layer on the CSI analysis is removed by setting the limits of the first layer as surface to 850 hPa.

For a layer  $\Delta p$ , the ice Richardson number  $Ri_{ice}$  criterion is

$$Ri_{ice} \approx \frac{\eta_g \Gamma_{ice} g}{f \Gamma_d \theta_{ref} \Delta z} \left( \frac{\Delta v_g}{\Delta z} \right)^{-2} < 1, \quad (2.21)$$

where  $\Delta\theta_{ei} = \theta_{ei}(p - \Delta p) - \theta_{ei}(p)$ ,

$\Delta v_g = v_g(p - \Delta p) - v_g(p)$ ,

$\Delta z = z(p - \Delta p) - z(p)$ ,

and  $\eta_g$  is the geostrophic absolute vorticity in the layer ( $\eta \equiv \eta_g$ ). Here  $\theta_{ref}$  is a reference ice equivalent potential temperature and is measured at the top of the atmospheric layer. Variables in (2.21) can be separated into those that determine thermodynamic properties and those that determine dynamic properties.

#### a) Assessment of thermodynamic properties

For the ice phase,  $\theta_{ei}$  is calculated from Bolton's (1980) expression

$$\theta_{ei} = \theta_i \exp \left[ \left( \frac{3376}{T_{LCL}} - 2.54 \right) w_i (1 + 0.81 w_i) \right], \quad (2.22)$$

where  $\theta_i$  (K) is the ice potential temperature,  $w_i$  (kg/kg) is the ice mixing ratio, and  $T_{LCL}$  (K) is the temperature of the lifting condensation level. Following Bolton,  $T_{LCL}$  is computed from

$$T_{LCL} = \left[ \frac{1}{T_f - 56} + \frac{\ln(T/T_f)}{800} \right]^{-1} + 56, \quad (2.23)$$

where  $T_f$  (K) is the frost point temperature (i.e. the temperature where the air is saturated with respect to ice). Since sounding data contain the dewpoint temperature  $T_d$  (K),  $T_f$  (K) is computed by (Iribarne and Godson 1986)

$$T_f = \frac{T_t}{1 + L_v/L_s(T_t - T_d)/T_d} \quad (2.24)$$

where  $T_t$  (K) is the triple point of water (273.16 K), and  $L_v$  and  $L_s$  are the latent heats of vapourization and sublimation, respectively. The values  $L_v$  and  $L_s$  vary little with temperature (< 4% change between 0°C and -30°C), and are assumed to be constant. Due to errors in radiosonde measurements of relative humidity,  $T_f$  can become supersaturated in equation (2.24). For these situations, the frost point is set equal to the air temperature.

The ice mixing ratio  $w_i$  and the ice potential temperature  $\theta_i$  (K) are computed by

$$w_i = 0.622 \left[ \frac{e_i}{P - e_i} \right], \quad (2.25)$$

$$\theta_i = T \left[ \frac{1000}{P} \right]^{0.2854(1 - 0.28w_i)}, \quad (2.26)$$

where  $P$  (hPa) is the air pressure and  $e_i$  (hPa) is the saturated ice vapour pressure which is determined from Smithsonian tables (List 1963).

The ratio  $\Gamma_{ice}/\Gamma_d$  is evaluated using a standard thermodynamic expression (Rogers and Yau 1989, pg. 32)

$$\frac{\Gamma_{ice}}{\Gamma_d} = \frac{1 + (L_s w_i / R_d T)}{1 + 0.622 (L_s^2 w_i / C_{pd} R_d T^2)}, \quad (2.27)$$

where  $R_d$  is the specific gas constant for dry air, and  $C_{pd}$  is the specific heat capacity of dry air at constant pressure.

#### **b) Assessment of dynamic properties**

To determine the vertical shear in (2.21), the atmospheric flow is assumed to be in geostrophic balance. Thus the  $y$  component of the geostrophic flow  $v_g$  is



$$v_g \approx V \cos(\alpha - \beta), \quad (2.28)$$

where  $V$  is the speed of the observed wind,  $\alpha$  is the direction of  $V$  in degrees from north and  $\beta$  is the direction of the thermal wind shear in degrees from north. Seltzer et al. (1985) showed that a  $15^\circ$  error in  $\beta$  will only change the vertical shear by 4% for typical wind conditions.

The geostrophic absolute vorticity is given by

$$\eta_g = f + \frac{g}{f} \left[ \frac{\partial^2 Z}{\partial x^2} + \frac{\partial^2 Z}{\partial y^2} \right], \quad (2.29)$$

where  $Z(m)$  denotes the height of the pressure level  $P$ . Using height contours from the standard map levels (i.e. 850 hPa, 700 hPa, 500 hPa, 250 hPa),  $\eta_g$  is approximated using the finite difference approximation for the Laplacian of  $Z$

$$\nabla^2 Z \approx \frac{Z_1 + Z_2 + Z_3 + Z_4 - 4Z_0}{d^2}, \quad (2.30)$$

where  $Z_1, Z_2, Z_3, Z_4, Z_0$  are the heights, in metres, of the pressure level on a grid with spacing  $d(m)$  (Fig. 2.4). For the computation of  $\eta_g$ ,  $d$  is 222 km ( $2^\circ$  latitude) and  $f$  is  $11.7 \times 10^{-5} \text{ s}^{-1}$  at latitude  $53.3^\circ\text{N}$ . To determine the vertical profile in  $\eta_g$ , linear interpolation is used.

### c) Errors

The single sounding technique has a number of error sources which will affect the thermodynamic and dynamic calculations. For the thermodynamic calculation in equation (2.21) errors in the measurement of temperature ( $\pm 0.8^\circ\text{C}$ ) and relative humidity ( $\pm 15\%$ ) by the radiosonde (Ray 1986) will affect the moist Brunt-Väisälä frequency.

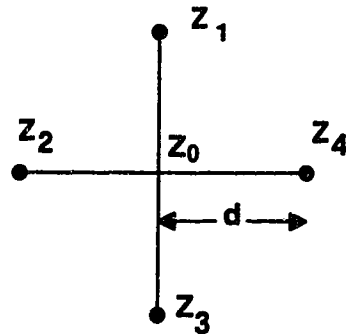


Figure 2.4: Finite difference approximation of the Laplacian.

The requirement for a geostrophic balanced flow in equation (2.21) may not be the case when winds are light or do not increase with height in a baroclinic zone. In these weakly sheared environments, the geostrophic shear  $\Delta v_g / \Delta z$  may not be accurate (Aktary and Reuter 1993; Seltzer et al. 1985), but these situations are of little interest as the flow is usually absolutely stable ( $Ri_{ice} \rightarrow \infty$  when  $\Delta v_g / \Delta z \rightarrow 0$ ).

The value of  $\eta_g$  will also have an error of about 10% due to a fixed grid distance  $d$  placed on a polar stereographic map projection (Aktary and Reuter 1993). If weakly sheared environments are neglected and if the flow is in geostrophic and hydrostatic balance, the primary source of error in  $Ri_{ice}$  will occur from errors in the radiosonde measurements and  $\eta_g$ . Thus in these situations a 10-15% error in  $Ri_{ice}$  should be expected.

### 3 Analysis of a Warm Frontal Snowband

#### 3.1 Introduction

On 16 October 1991, a Pacific storm moved into southern British Columbia. Heavy snow fell north of the storm's warm front which was oriented in a west to east line across south-central Alberta. Snowfall accumulations associated with this storm are shown in Fig. 3.1. Radar observations indicated the snow field was enhanced by a warm frontal snowband (type 1a in Fig. 1.1) which was oriented in the direction of the upper-level flow. The goal of this chapter is to determine the precipitation production of the snowband using radar observations. The potential for Conditional Symmetric Instability (CSI) as a formation mechanism will also be examined. The organization of this chapter is as follows:

- a) Section 2 presents the large-scale flow pattern and the snowfall accumulations across central Alberta.
- b) Section 3 examines the thermodynamic profile of the airmass and determines the potential for CSI in the baroclinic flow.
- c) Section 4 presents the evolution and the vertical structure of the snowband.
- d) Section 5 determines the integrated snow budget at the snowband's mature stage.
- e) Section 6 examines the time evolution of the integrated snow budget.
- f) Section 7 performs a sensitivity analysis on the snow budget results.

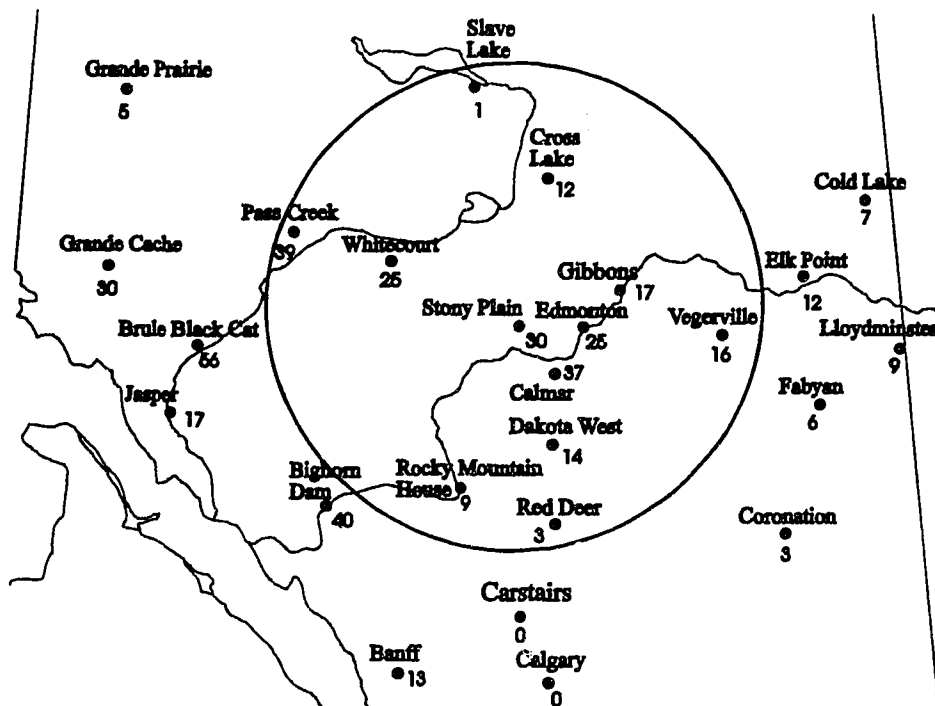


Figure 3.1: Snowfall accumulations (cm) across central Alberta for 16 October 1991. The circle represents the outer range (220 km) of the Carvel radar.

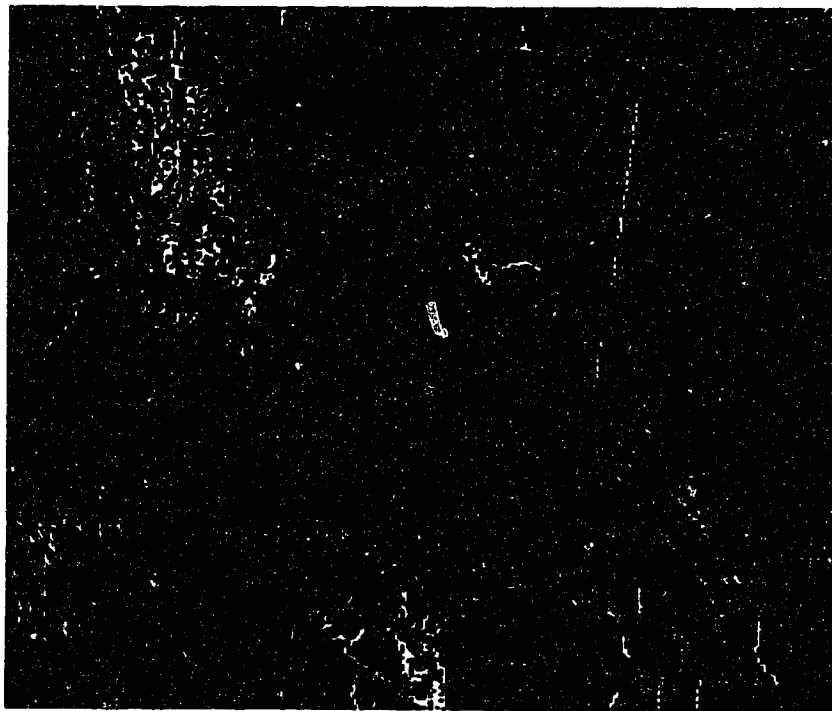


Figure 3.2: 2237 UTC 15 October 1991 IR-satellite image of British Columbia and Alberta.

## 3.2 Synoptic overview

### a) Storm Evolution

On 15 October 1991 cloud was streaming in from the Pacific into southern British Columbia and central Alberta (Fig. 3.2). The cloud mass was associated with a Polar Maritime front (Petterssen 1940) lying over southern British Columbia and central Alberta. The surface analysis at 0000 UTC 16 October 1991 showed the Polar Maritime front with a number of weak low pressure systems (Fig. 3.3a). In Alberta, the north to south temperature gradient across this front was about  $5^{\circ}\text{C}/100\text{ km}$  which is considered large for Alberta.

The cloud mass shown on the satellite image covered the 850 hPa baroclinic zone, indicated by the strong temperature gradient over central Alberta and southern British Columbia (Fig. 3.4a). This cloud mass was composed of thick cloud layers since it followed the 500 hPa circulation pattern (Fig. 3.5a). The presence of backing winds between 850 hPa and 500 hPa over northern British Columbia and Alberta at 0000 UTC, indicated the airmass was cooling. The amount of change in the wind direction and speed across the depth of the layer determines the rate of cooling. With no cooling occurring over southern British Columbia and Alberta, the baroclinic zone at 850 hPa intensified over the next 12 hours (Fig. 3.4b). With cold air advection, heights at 500 hPa decreased, thus allowing the longwave trough in the eastern Pacific to approach the west coast (Fig. 3.5b).

By 0600 UTC 16 October 1991 (Fig. 3.3b), the last in a series of low pressure systems moved over Vancouver Island. With dynamic support from the approaching mid-tropospheric trough, the precipitation area now stretched from Vancouver Island to central Alberta. Precipitation consisted of snow

over central British Columbia and a combination of rain and snow over Alberta.

By 1200 UTC 16 October 1991, the low pressure system moved into southern British Columbia and deepened to 986 hPa (Fig. 3.3c). Snow was widespread north of the warm front with the highest accumulations reported over the foothills (Fig. 3.1). The low pressure system continued to deepen to 980 hPa over the next 6 hours. By this time, the system crossed the mountains into south-central Alberta triggering strong downslope winds over southern Alberta with gusts exceeding 100 km/h. The low pressure system moved into south-western Saskatchewan by 0000 UTC 17 October 1991 with associated snow dissipating over central Alberta.

#### *b) Snowfall distribution*

Precipitation associated with the Pacific cyclone began as rain then changed to snow across central Alberta by 0700 UTC 16 October 1991. Snow fell across central Alberta for approximately the next 20 hours with total snowfall accumulations shown in Fig. 3.1. The snowfall accumulations associated with this one storm were more typical of the climatological monthly snowfall for October (10 cm to 20 cm).

Snowfall accumulations for the Edmonton area ranged from 29 cm at the International Airport (53.19°N, 113.35°W) to 17 cm at CFB Namao (53.40°N, 113.28°W). Besides some local variability in the ambient snow field, the difference in snowfall accumulations was probably caused by a west to east snowband which formed about 30 km south of Edmonton between 0600 UTC and 0700 UTC. The snowband, observed on radar, remained stationary until 0900 UTC then drifted northward across the city before dissipating near 1300 UTC.

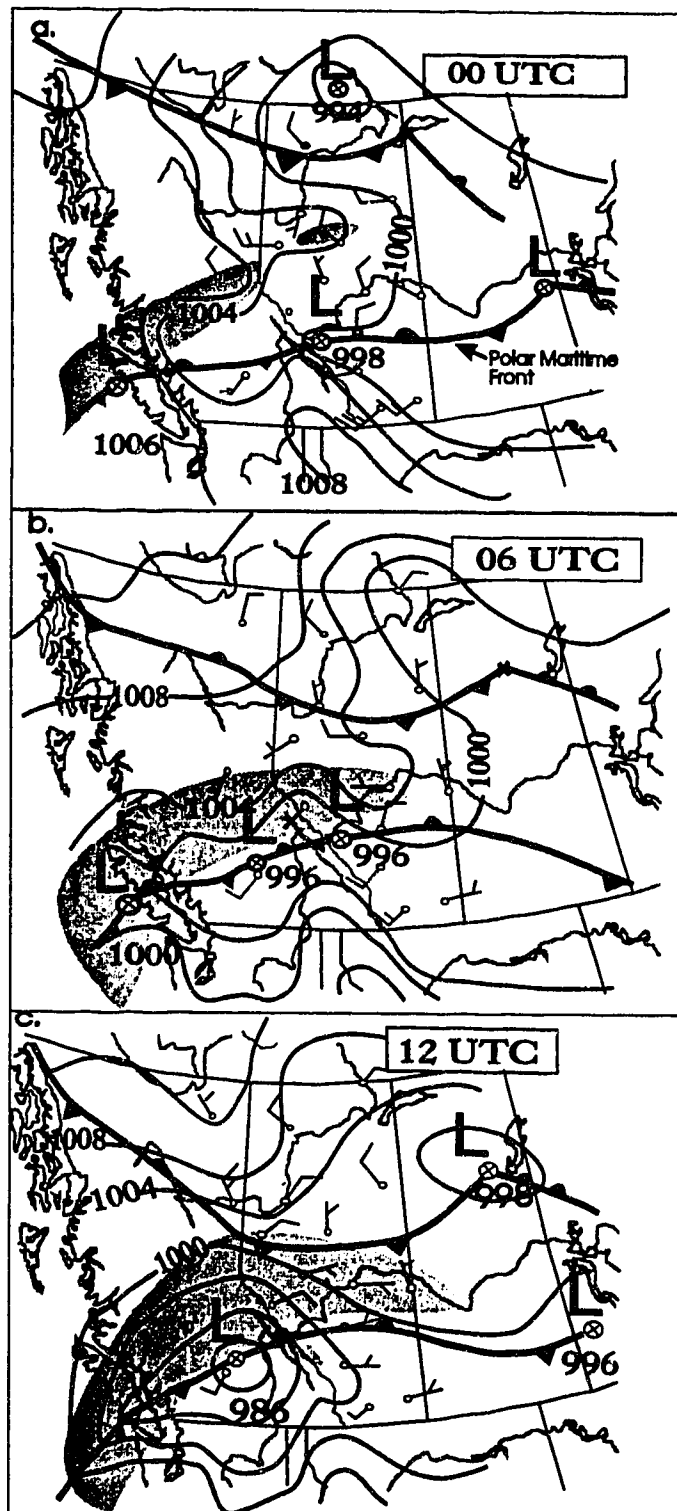


Figure 3.3: Surface analyses for 16 October 1991 with mean sea level pressure contours in hPa and precipitation shaded grey. Conventional station model used for winds (half barb 5 Kt and full barb 10 Kt).

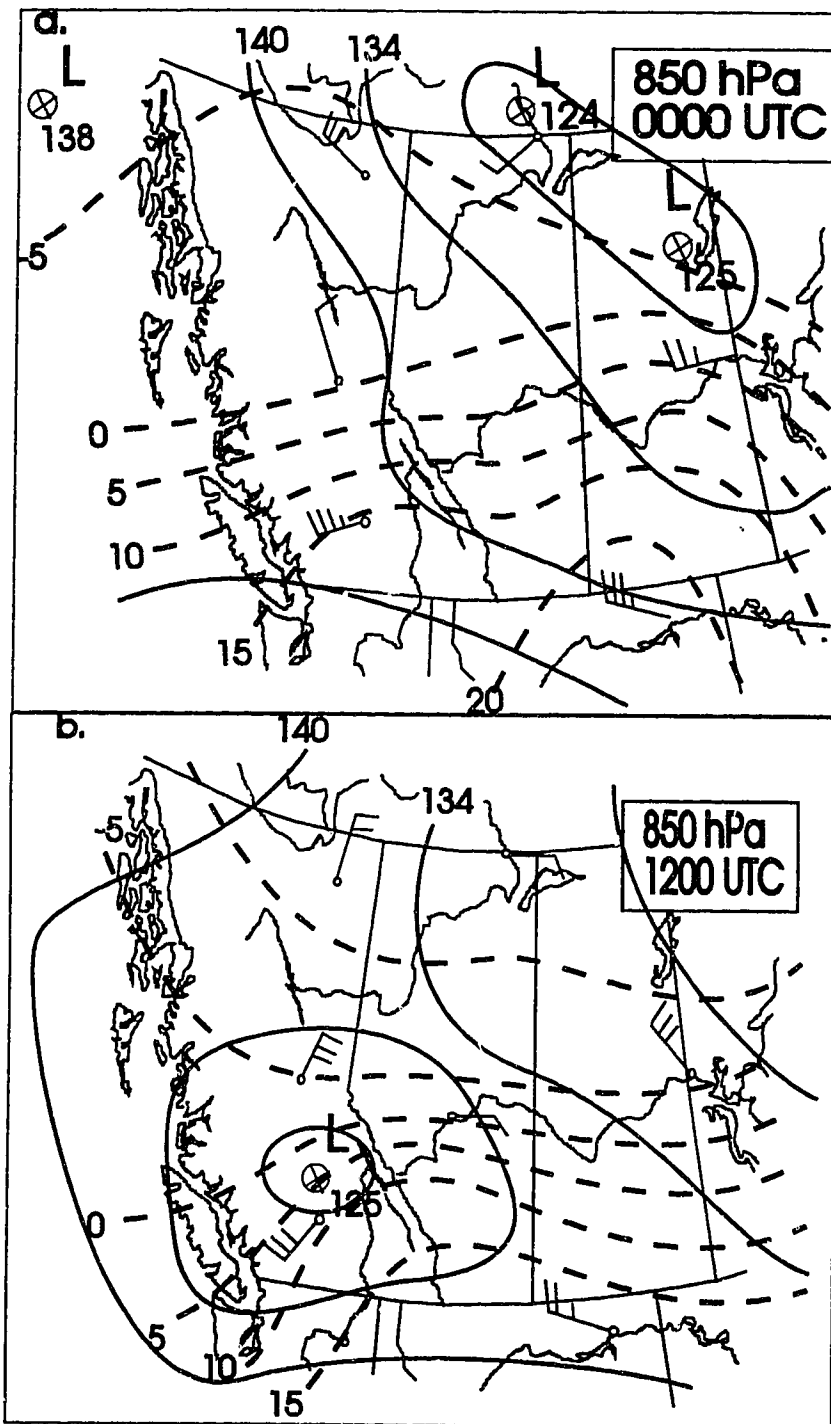


Figure 3.4: 850 hPa analysis (a) 0000 UTC and (b) 1200 UTC for 16 October 1991. Height contours (solid lines) in dm and isotherms (dashed) in °C. Conventional station model used for winds.



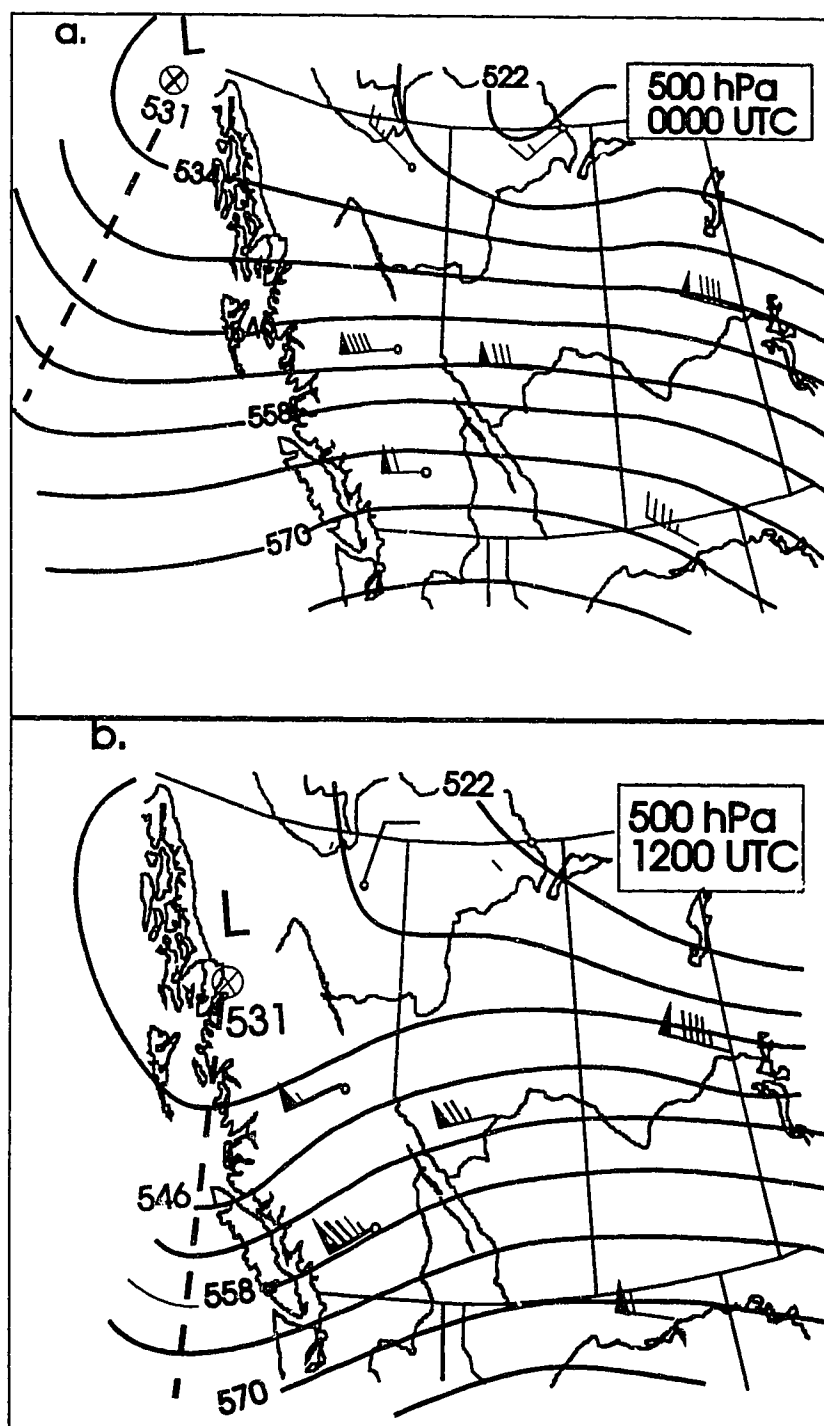


Figure 3.5: 500 hPa analyses (a) 0000 UTC and (b) 1200 UTC for 16 October 1991. Height contours (solid lines) in dm. Dashed line marks position of longwave trough. Conventional station model used for winds (filled wind barbs represents 50 Kt, full barbs 10 Kt with half barbs 5 Kt).

### 3.3 Atmospheric stability

The thermodynamic structure of the atmosphere is determined by radiosondes launched daily from Stony Plain at 0000 UTC and 1200 UTC. The atmosphere can be assessed for CSI from the sounding data by calculating the ice Richardson Number  $Ri_{ice}$  for various layers (chapter 2).

At 0000 UTC 16 October 1991, the atmospheric sounding (Fig. 3.6a) showed a dry airmass with a frontal zone between 750 hPa and 700 hPa. The wet bulb potential temperature  $\theta_w$  was 8°C below 750 hPa and 14°C above 700 hPa. This  $\theta_w$  profile is typical for a Polar Maritime frontal zone (Petterssen 1940). Although the sounding was dry, potential instability existed between 700 hPa and 500 hPa. If sufficient moisture became available, lifting an air parcel to saturation from the base of this layer would allow Altocumulus Castellanus (ACC) type cloud to development.

Conditions changed dramatically over the next 12 hours as the baroclinic zone tightened over central Alberta (Fig. 3.4), resulting in cooling of about 7°C below 650 hPa (Fig. 3.6b). The atmosphere also became saturated below 350 hPa resulting in a stable atmosphere except for the layer between 630 hPa and 350 hPa which was close to neutral. The veering of the wind direction with height (implies warm air advection) below 630 hPa showed that central Alberta was in the pre-frontal region of a warm front. The frontal zone (700 hPa to 630 hPa) was marked by the strong vertical shear with winds increasing from 5 Kt to 55 Kt (1 Kt = 1.98 m/s) over 700 metres. Above 630 hPa winds remained from the south-west and increased gradually with height.

### a) Analysis for CSI

Previous studies have computed the moist Richardson Number  $Ri_m$  for various layers (e.g. Seltzer et al. 1985; Donaldson and Stewart 1989; Reuter and Aktary 1993). This study is unique in using ice phase processes in the stability analysis. The potential for CSI exists in a given layer of air when  $Ri_{ice} < 1$ . Since the 0000 UTC sounding had no wind data, our stability analysis is confined to 1200 UTC sounding data (Table 3.1). From a thermal shear direction of  $265^\circ$  (determined using winds at 630 hPa and 500 hPa), both  $Ri_m$  and  $Ri_{ice}$  were determined for various layers (Table 3.2). The following statements can be made about this CSI analysis:

- ♦ The airmass was moist symmetrically unstable from 700 hPa to 500 hPa and from 400 hPa to 300 hPa. The airmass was saturated in the first layer, thus slantwise overturning could occur.
- ♦ The release of CSI accounts for the snowband orientation and it's life span since the potential for CSI most likely existed for the previous 6 hours.
- ♦ Below 700 hPa, the flow was not unidirectional and probably non-geostrophic due to light winds. Thus, conditions required to analyze CSI were not met and the analysis can be ignored in this region.
- ♦ For Richardson numbers less than 1,  $Ri_{ice}$  and  $Ri_m$  produced similar results with values within  $\pm 0.1$ . Thus  $Ri_m$  provides an adequate indication of airmass stability for CSI, even when temperatures are below  $0^\circ\text{C}$ .

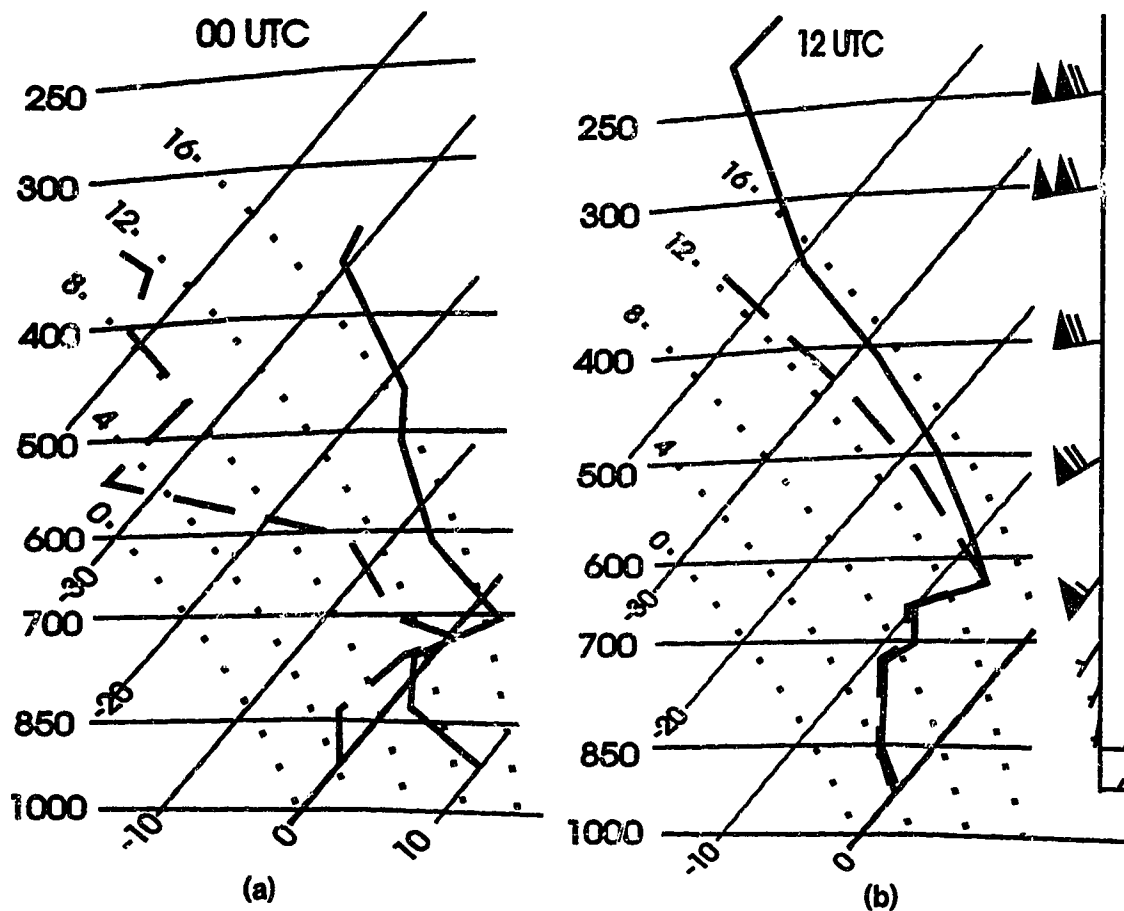


Figure 3.6: Tephigram of 16 October 1991 (a) 0000 UTC and (b) 1200 UTC, soundings taken at Stony Plain (WSE) with temperature (thick solid line) and dew point (dashed line). Horizontal lines are isobars (hPa), straight lines skewed to the right are isotherms ( $^{\circ}\text{C}$ ), and dotted lines are pseudo-adiabats ( $^{\circ}\text{C}$ ). Observed winds with height on the right hand side using the conventional station model (solid flag represents 50 Kt, full barb is 10 Kt and half barb 5 Kt).

- ♦ With the ratio  $\eta_v/f$  ranging from 0.7 to 1.2, the effect of approximating this ratio as one (e.g. Seltzer et al. 1985) would not affect the stability analysis.
- ♦ In the fall season (September to November), only 16% of precipitation events are associated with CSI (Reuter and

Aktary 1995). This is one type of synoptic event where CSI can be observed in the fall season.

Studies have shown the presence of generating cells above warm frontal precipitation bands (e.g. Browning et al. 1973; Hobbs and Locatelli 1978; Herzegh and Hobbs 1980). The concept of generating cells was introduced by Marshall (1953) to describe the region where convective cells provide the environment for the growth of ice crystals. These cells can be inferred from radar observations by the snow trails they produce (Rogers and Yau 1989, pg. 201). Using a vertical pointing Doppler radar, Carbone and Bohne (1975) determined that generating cells have vertical air velocities of  $\pm 1.5$  m/s. Wexler (1955) suggested that ice crystals developed in the generating cells by deposition and accretion (i.e. the process of collecting supercooled cloud drops).

Matejka et al. (1980) suggested that a seeder-feeder mechanism can occur within a warm frontal rainband. In an unstable layer called the seeder zone, generating cells form which produce ice crystals. These crystals fall into thick stratiform cloud called the feeder zone and grow by further accretion and aggregation (i.e. the process of collecting other ice crystals). This seeder-feeder mechanism aids in the conversion of cloud water and cloud ice in the feeder zone to precipitation (Herzegh and Hobbs 1980; Houze et al. 1981). In our case, generating cells at the top of the snowband seed the roll cloud formed by slantwise overturning. Within this roll cloud, the seed crystals grow mainly by accretion and aggregation. As the crystals fall out of the convective cells, they grow further by aggregation in the thick feeder cloud (i.e. stratiform cloud) below 3 km. However with the data available, the growth of snow by this method cannot be verified.

Table 3.1: 16 October 1991, 1200 UTC sounding data. Listed are the temperature  $T$ , dewpoint  $T_d$ , frost point  $T_f$ , ice saturation vapour pressure  $e_i$ , ice mixing ratio  $w_i$ , ice potential temperature  $\theta_i$ , lifting condensation temperature  $T_{LCL}$ , the ice equivalent potential temperature  $\theta_{ei}$ , and the ratio of the ice adiabatic lapse rate to the dry adiabatic lapse rate  $\Gamma_{ice}/\Gamma_d$ .

Press hPa	$T$ °C	$T_d$ °C	$T_f$ °C	$e_i$ hPa	$w_i$ g/kg	$\theta_i$ K	$T_{LCL}$ K	$\theta_{ei}$ K	$\Gamma_{ice}/\Gamma_d$
911	-0.5	-0.6	-0.5	5.86	4.0	280	273	291	0.6
850	3.7	-3.9	-3.7	4.49	3.3	282	269	292	0.6
700	-7.9	-8.5	-7.9	3.12	2.8	294	255	302	0.7
631	-5.9	-6.0	-5.9	3.72	3.7	305	267	316	0.6
500	-17.1	-19.2	-17.1	1.36	1.7	312	256	318	0.7
400	-29.3	-33.9	-30.3	0.41	0.6	317	243	319	0.9
300	-44.7	-50.7	-45.6	0.07	0.2	322	227	323	1.0
250	-52.7	-59.7	-54	0.003	0.01	327	219	328	1.0

Table 3.2: Stability analysis for 12 UTC 16 October 1991. Listed are the relative humidity RH, the vertical gradient of the zonal wind  $dv_g/dz$ , the ice Brunt-Väisälä frequency  $N_i^2$ , the ratio  $\eta_g/f$ , the ice Richardson number  $Ri_{ice}$  and the moist Richardson number  $Ri_m$ . Conditional Symmetric Instability and Absolute Stability are denoted by SI and AS, respectively.

Layer hPa	RH %	$dv_g/dz$ $\times 10^{-3} s^{-1}$	$N_i^2$ $\times 10^{-4} s^{-2}$	$\eta_g/f$	$Ri_{ice}$	$Ri_m$	Stability Condition
sfc-850	100	-6.4	0.2	1.0	0.3	0.6	SI
850-700	100	4.8	2.2	1.5	9.4	9.8	AS
700-631	100	26	5.5	1.2	0.6	0.7	SI
631-500	100	7.0	0.2	0.7	0.2	0.3	SI
500-400	96	0.7	0.2	0.8	32	89	AS
400-300	69	10.	0.6	0.9	0.6	0.5	SI
300-250	65	2.8	1.2	1.0	15	11	AS

### 3.4 Radar analysis

#### a) *Evolution of the snowband from radar*

Observations from the C-band radar located in Carvel, indicated that the snowband existed ~~for~~ 6 to 7 hours. From 0700 UTC to 0930 UTC, the snowband remained about 30 km south of the radar. Fig. 3.7 depicts the half-hourly CAPPI radar imagery for this period.

At 0700 UTC 16 October, an area of stronger precipitation (0.9 cm/h), existed to the north-west of the radar. Also a broken east to west precipitation band was found about 30 km south of the radar. Over the next 30 minutes, the echoes south of the radar formed into a continuous band. During the next 2 hours, the snowfall rates in the roughly 25 km wide snowband varied in intensity, suggesting the band was in various stages of it's life span. Between 0700 UTC and 0730 UTC, the snowband was in the developing stage as the echoes to the south of the radar formed into a line echo. The snowfall rate continued to intensify until reaching a maximum near 0800 UTC. At the mature stage, the snowband was characterized by a sharp cross-band reflectivity gradient. This gradient, along with the snowfall intensity, weakened to become quasi-steady by 0830 UTC. Between 0900 UTC and 0930 UTC, the snowband drifted towards the radar probably as a result of the mid-tropospheric flow shifting from westerly to south-westerly.

#### b) *Snowband vertical cross-section*

The CAPPI imagery shown in Fig. 3.7 indicated the snowfall intensity varied only slightly along the length of the band (i.e. the precipitation field was close to slab-symmetric). Thus a vertical cross-section, oriented perpendicular to the snowband, is representative of the

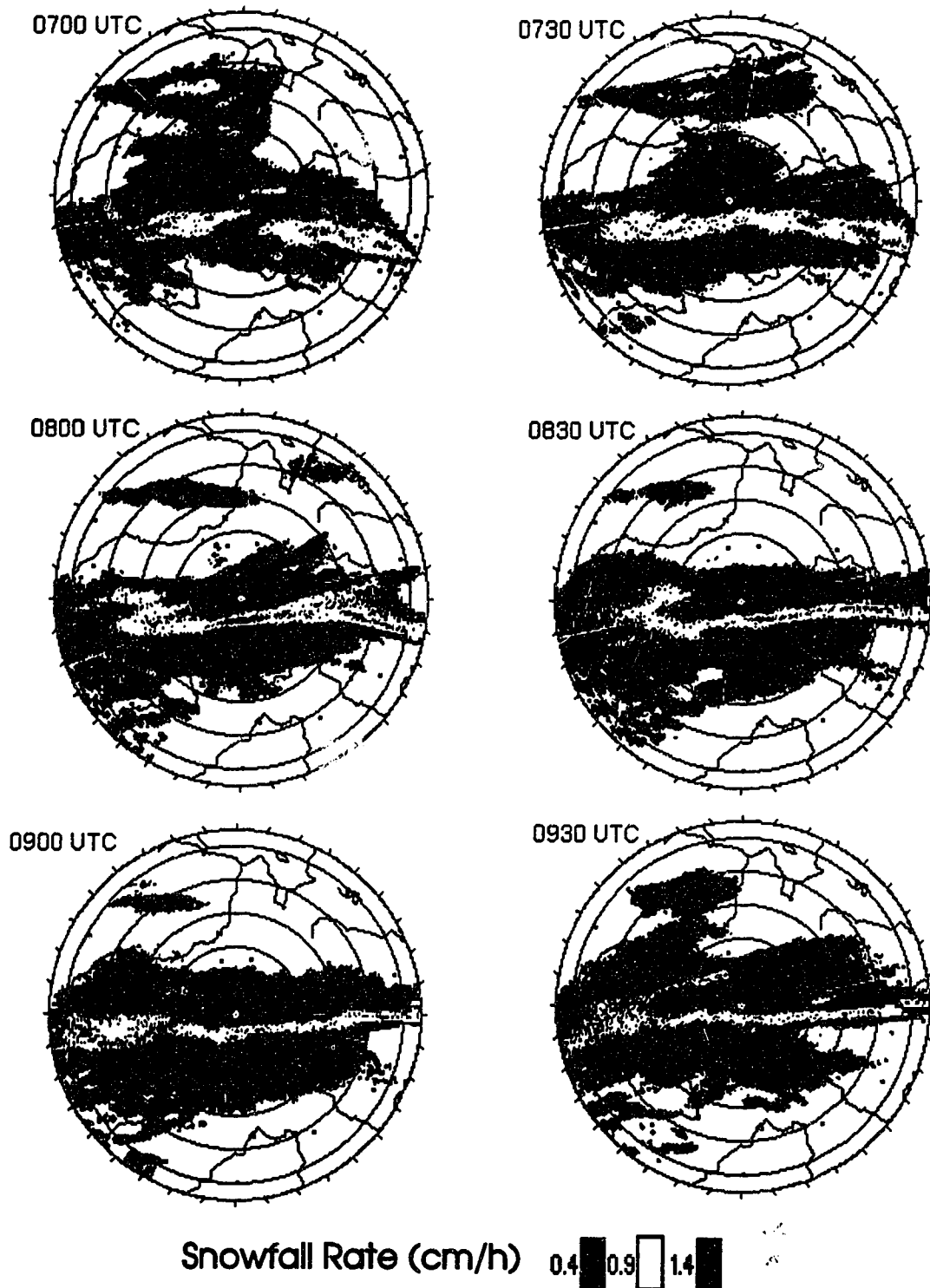


Figure 3.7: CAPPI 1.5 km radar images of the snow field for 16 October 1991. Rings spaced 40 km apart. Cities and towns within the range of the radar is shown in Fig. 3.1.



entire band. From the 0830 UTC radar volume scan of ice reflectivity factor  $Z_1(\text{dBz})$ , the vertical structure of the snowband can be determined using  $Z_1(\text{dBz})$  along an azimuth angle of  $175^\circ$  (i.e. angle perpendicular to the band). With a horizontal and vertical resolution of 1 km and 0.1 km, respectively, the  $Z_1(\text{dBz})$  data was interpolated to a uniform Cartesian grid using Cross (1959) interpolation method (Haltiner and Williams 1980, pg. 356).

A contour analysis of the gridded  $Z_1(\text{dBz})$  is shown in Fig. 3.8. The snowband is depicted by a distinct 25 km wide reflectivity zone about 30 km from the radar. The snowband had a reflectivity top about twice the height of the warm frontal zone near 2.8 km AGL (Above ground level). Between 2.8 km and 5 km AGL (630 hPa to 500 hPa), the core of higher  $Z_1(\text{dBz})$  values probably occurred due the release of CSI. Above 5 km AGL, the precipitation observed may correspond with a snow trail being created by generating cells (Houze et al. 1981). Generating cells would provide seed crystals into the roll circulation where they grow mainly by aggregation and accretion. As the crystals fall out of the roll circulation into the stable airmass, they grow further by aggregation.

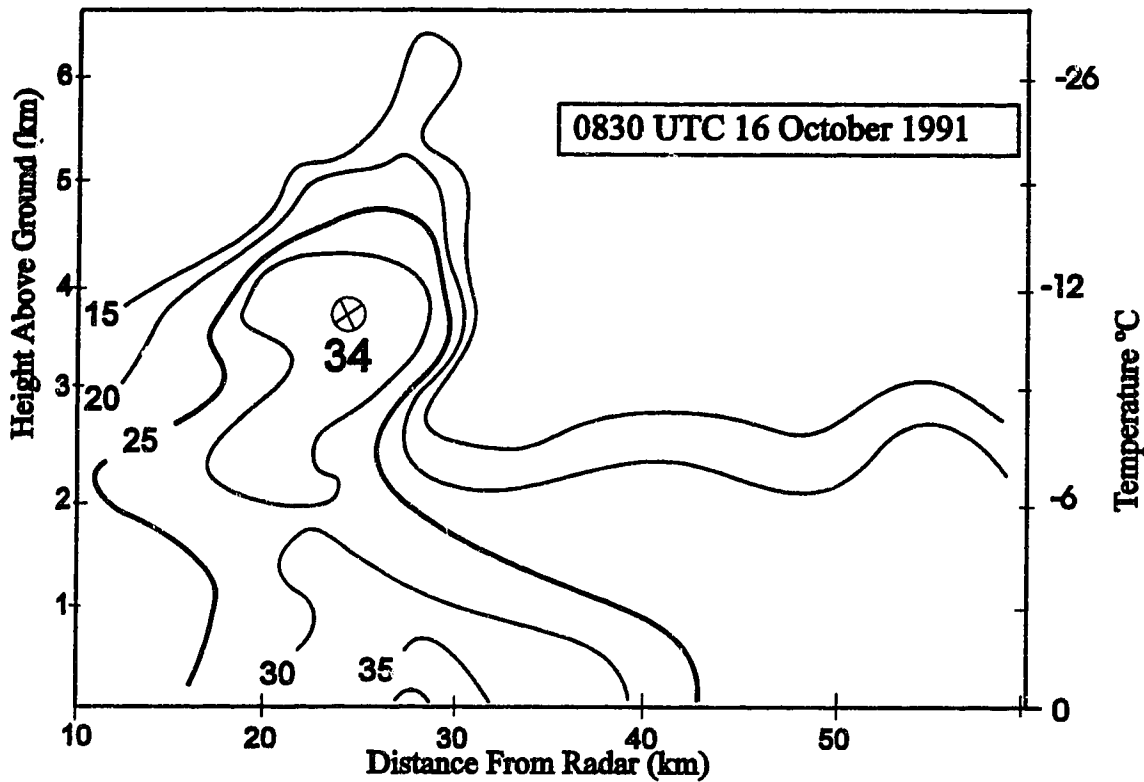


Figure 3.8: Snowband reflectivity cross-section at 0830 UTC. Contours every 5 dBz.

### 3.5 Snow budget at the mature stage

The CAPPI imagery indicated the snowband was at its mature stage between 0750 UTC and 0810 UTC. Based on radar observations of the snowband at 0800 UTC, the integrated snow budget was determined for a vertical cross-section perpendicular to the band. The cross-section data were first corrected for ground clutter and then converted to  $Z_i$  (dBz). To determine the snow budget quantities  $P$  and  $dO/dt$ , a cross-section azimuth angle of  $175^\circ$  and a reflectivity threshold  $Z_c$  (dBz) of 25 dBz were used. A cloud base height of 0.5 km AGL was determined from the synoptic observations taken at the Edmonton Municipal Airport.

To determine the effect that the size of the cross-section would have on the snow budget quantities, a 25 km and a 50 km cross-section were both analyzed. The

25 km cross-section analysis focused on the central core of the snowband, and used radar data between 15 km and 40 km. The 50 km analysis examined the entire width of the snowband, and used radar data between 10 km and 60 km. Table 3.3 lists the results for the 0800 UTC analysis.

Table 3.3: Mature stage (0800 UTC) snow budget analysis for a 25 km and a 50 km snowband cross-section.

Parameter	Units	25 km	50 km
$dO/dt$ - Mass Outflow Rate	Mg/s km <sup>-1</sup>	7.6	10.
W - Band Width	km	25	40.
$R_{avg}$ - Average Snowfall Rate	cm/h	1.1	0.9
P - Total Snow Content	Gg/km	12.2	14.5
A - Band Cross-sectional Area	km <sup>2</sup>	56	71
$P_{avg}$ - Average Snow Content	g/m <sup>3</sup>	0.22	0.20
$\tau$ - Characteristic Time	min	27	24
U - Characteristic Updraft	m/s	1.4	1.2

The contributions of reflectivity values, outside the 25 km analysis region, to the 50 km analysis produced smaller gains in the mass outflow rate  $dO/dt$  and the total snow content P relative to the size increase of the snowband. By doubling the cross-section width, the band width W increased by 60% while the mass outflow rate increased by 32%. Likewise, a 27% increase in the band cross-sectional area A resulted in an increase of 19% in the total snow content. Thus average or characteristic budget quantities determined using the 25 km cross-section would tend to be larger than the 50 km cross-section. However, with doubling the cross-section analysis region, only a 10% to 15% difference resulted in each of  $R_{avg}$ ,  $P_{avg}$ ,  $\tau$ , and U. Thus these budget quantities can be assumed independent of the cross-section width analyzed since their uncertainty is 20% or more. Since the 50 km band cross-section analysis

examined the entire band width, the discussion will focus on these results.

**a) Average snowband properties**

Since this was the first study to determine properties of a snowband through precipitation production, difficulties arose when trying to verify the results with other studies. Comparing the average snow rate  $R_{avg}$  to synoptic observations of snowfall accumulations at Edmonton indicated a similar snowfall rate of about 1 cm/h. The integration process can be verified by determining the average  $Z_1$  (dBz) value from the average snow content  $P_{avg}$ . With a  $P_{avg}$  of  $0.20 \text{ g/m}^3$ , the average  $Z_1$  (dBz) for the snowband was 31 dBz which appears reasonable when compared with Fig. 3.8. It was difficult to compare  $P_{avg}$  with other studies since the airmass type (e.g. Pacific, Continental) would influence it's value.

When the snowband is relatively steady, the characteristic time  $\tau$  represents the time needed for the snow to develop in the snowband. The value of  $\tau$  would be affected by the temperature of the airmass since this has some affect on which snow growth mechanism is dominant. The maximum diffusional growth rate of ice crystals occurs at a temperature of  $-15^\circ\text{C}$  (Roger and Yau 1989, pg. 161). Aggregation becomes significant in the formation of snow above  $-10^\circ\text{C}$ , while accretion is important in convective type clouds, where the updraft can provide a steady source of condensed water vapour (Rogers and Yau 1989, pg. 207). The value of  $\tau$  would also be affected by the time scales of the different microphysical mechanisms. Some model results reported by Young (1993, pg. 240, 274) are of interest. For an updraft of 1 m/s, condensation-diffusional growth of snow takes more than 50 minutes to reach a 20 dBz echo. However, growth by accretion and aggregation takes only 26 minutes with a cloud base temperature of  $-5^\circ\text{C}$ . For the warm frontal

snowband considered in this study, ice crystals most likely formed by deposition and accretion in the generating cells and possibly within the roll circulation caused by the release of CSI. These ice crystals grew further in the roll circulation by accretion and aggregation. The mass of snow above the frontal zone where the roll circulation was taking place was 4 Gg/km or 28% of the total snow content for the snowband. When this snow fell into the frontal zone it grew further by aggregation in the stratiform cloud. This possible growth mechanism is similar to the seeder-feeder mechanism discussed earlier. Houze et al. (1981) found that a seeder-feeder mechanism was responsible for the development of precipitation within a rainband in about 20 minutes.

A model of a seeder-feeder process occurring in a warm frontal rainband (Rutledge and Hobbs 1983) indicated that the strength of the vertical updraft in the feeder cloud played a crucial factor in determining the precipitation rate. If the vertical air motions in the feeder cloud was produced by warm frontal lifting (0.1-0.2 m/s), the snowfall rate above the melting layer was 1.0 cm/h to 2.0 cm/h. However, if mesoscale lifting occurred in the feeder cloud of the rainband (~0.7 m/s) the snowfall rate above the melting layer was about 8 cm/h. The concept of a low vertical air velocity beneath the frontal zone combined with a convective layer above was also observed in a snowband studied by Zawadzki et al. (1993a). They found that with a snowfall rate of 0.8 cm/h to 6.0 cm/h, the vertical velocities ranged from 0.1 m/s in the low levels to about 1 m/s in the convectively unstable region above 3 km. Modelling the microphysical processes in this snowband, Zawadzki et al. (1993b) found that the rate of ice crystal generation, at the top of the snowband in generating cells (~6 km) was insensitive to the vertical air velocity. Ice

crystal formation was found to be dependent on the available moisture and the number of freezing nuclei. The growth of these ice crystals below 6 km was affected by the vertical updraft and by the availability of cloud water and ice. With the release of Convective Instability from 3 km to 6 km, most of the snow growth would occur in this region.

The budget calculations in this study yielded a characteristic updraft of 1.2 m/s, suggesting that significant portion of the snow was produced in the roll circulations caused by the release of CSI. The U value in this investigation also agreed with the fall speed of an aggregated snowflake which ranges from 0.8 m/s to 1.2 m/s (Passarelli and Srivastava 1979). Using a vertically pointing Doppler radar, Houze et al. (1976) found that snow fell at 1.0 m/s to 1.5 m/s above the melting layer in a warm frontal rainband.

***b) Affect of the snowband on the ambient snow field***

To approximate the affect the snowband would have on the ambient snow field, the snow budget was analyzed for the approximately 170 km wide synoptic snow area observed on radar at 0800 UTC (Fig. 3.7). Since the snow area also occurred north of the radar, the snow budget was determined along the azimuth angles of 175° and 355°. Data were excluded within 5 km of the radar due to noise created by secondary lobes. A cloud base of 0.5 km was used within 50 km of the radar for the analysis of  $dO/dt$  and P. Beyond this, the lowest radar elevation angle of 0.4° was used to approximate the cloud base. This elevation angle would rise into the cloud with distance from the radar, thus  $dO/dt$  and P values could be in error by a factor of 2. All  $Z_1$ (dBz) data at and above the radar minimum reflectivity of 13.5 dBz were used in the snow budget analysis. Table 3.4 shows the

snow budget results for both the synoptic snow field and the snowband.

Table 3.4: Comparison of the snowband's snow budget (50 km) with the synoptic snow area (170 km) on radar at 0800 UTC.

Parameter	Units	50 km	170 km
$dO/dt$ - Mass Outflow Rate	Mg/s km <sup>-1</sup>	10.	18
W - Band Width	km	40.	119
$R_{avg}$ - Average Snowfall Rate	cm/h	0.9	0.5
P - Total Snow Content	Gg/km	14.5	47
A - Band Cross-sectional Area	km <sup>2</sup>	71	470
$P_{avg}$ - Average Snow Content	g/m <sup>3</sup>	0.20	0.10
$\tau$ - Characteristic Time	min	24	44
U - Characteristic Updraft	m/s	1.2	1.5

The snowband contributed about 55% to the mass outflow rate in the synoptic snow area. However, this contribution did not increase the average snowfall rate of the synoptic snow area which remained around the value (~0.4 cm/h) observed on the CAPPI radar imagery (Fig. 3.7). The snowband did have a significant affect in the mesoscale, with a  $P_{avg}$  and a  $R_{avg}$  that were about double those calculated for the ambient snow field.

The characteristic time in the snowband was 24 minutes, while in the synoptic snow area it was 44 minutes. If the assumption of steady conditions were indeed valid for both regions, it can be concluded that snow formed more rapidly in the snowband than in the synoptic snow area.

The characteristic updraft was larger in the synoptic snow area than in the snowband. Since the snowband was about twice the depth of the snow field this would increase the area over which the total snow content was averaged. It should be stressed that U is a measure of the updraft averaged over the entire band cross-sectional area rather than a measure of the updraft near the storm base.

### 3.6 Time evolution of the snow budget

For the time period 0730 UTC to 0930 UTC, the time history of the integrated snow budget ( $dO/dt$ ,  $P$ ,  $R_{avg}$ ,  $P_{avg}$ ,  $\tau$ ,  $U$ ) was determined using a 50 km cross-section. The results which also include the band width ( $W$ ) and the band cross-sectional area ( $A$ ) are plotted in Fig. 3.9.

The time evolution of  $P$  and  $A$  (Fig. 3.9a,b) showed values decreasing by about 50% over the period. Local maxima and minima existed in the plots, but whether these fluctuations represented a systematic feature or were simply noise was not known. The peak in  $P$  of 17.4 Gg/km and in  $A$  of 94 km<sup>2</sup> occurred at least 30 minutes prior to the band's mature stage.

The time history of  $P_{avg}$  (Fig. 3.9c) shows a sinusoidal like trend with peaks at 0800 UTC, 0840 UTC and 0910 UTC. The peaks appear to correspond with weak minima in  $P$  and  $A$ . The maximum at 0800 UTC occurred during the band's mature stage. With a range from 0.17 g/m<sup>3</sup> to 0.20 g/m<sup>3</sup> and a time average of 0.19 g/m<sup>3</sup>, the evolution of  $P_{avg}$  appears to be quasi-steady.

The time evolution of  $dO/dt$  and  $W$  (Fig. 3.9d,e) displayed similar trends with maxima and minima roughly coinciding. As the snowband reached it's mature stage, the maximum in  $dO/dt$  of 10.5 Mg/s km<sup>-1</sup> occurred ten minutes prior to the maximum in  $W$ . This lag was probably caused by the snow spreading out as it fell from the upper portions of the snowband where it developed. The minimum at 0900 UTC was observed on CAPPI imagery as a general weakening of snowfall rates over the previous half hour (Fig. 3.7). However, snowfall rates did not increase over the next half hour in step with  $dO/dt$  and  $W$ . The minimum in  $dO/dt$  at 0740 UTC combined with a maximum in  $P$  suggested that a strong updraft was temporarily suspending the snow in the cloud. Once the



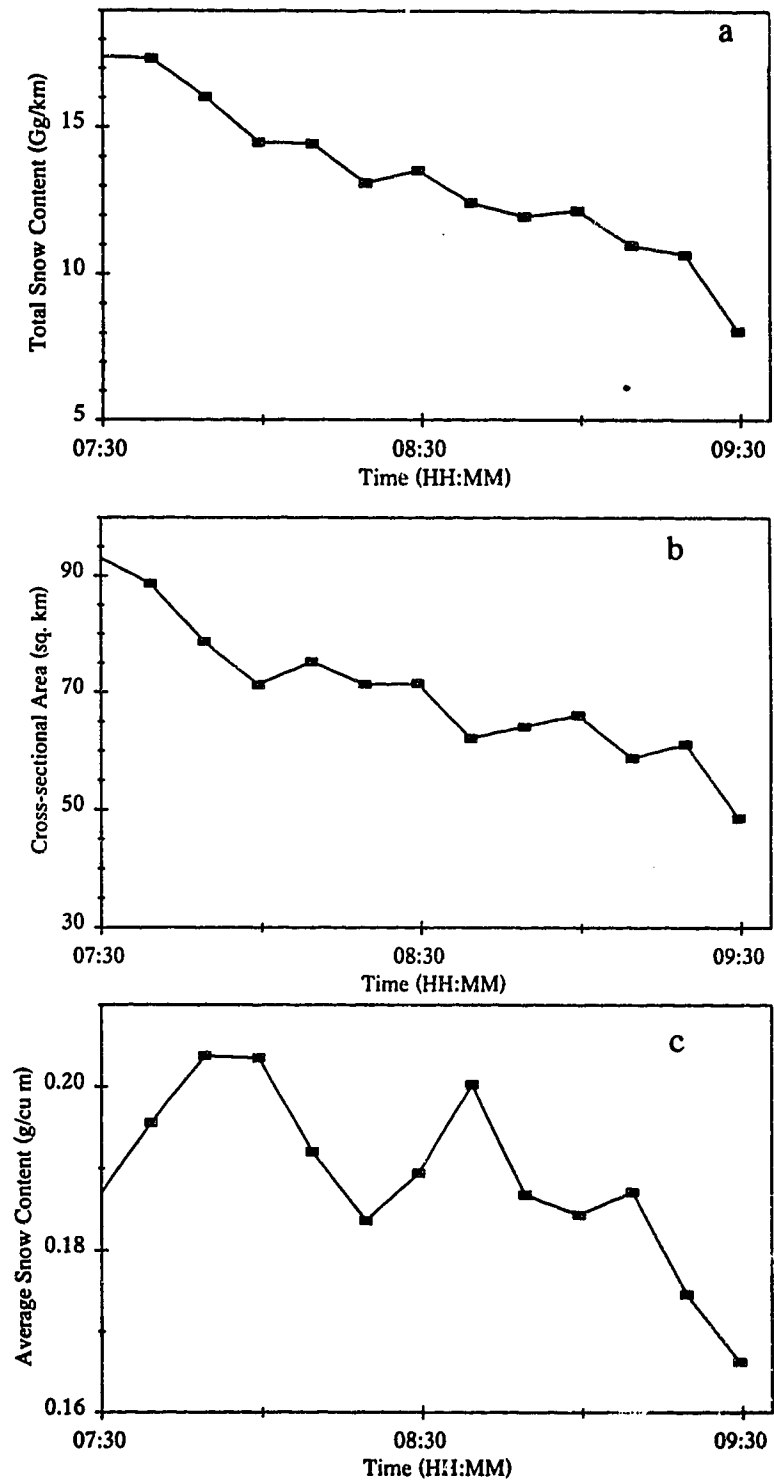


Figure 3.9: Evolution of budget parameters for 16 October 1991. Plots of: (a) Total snow content  $P$ ; (b) Cross-sectional area of the snowband  $A$ ; and (c) Average snow content  $P_{avg}$ .

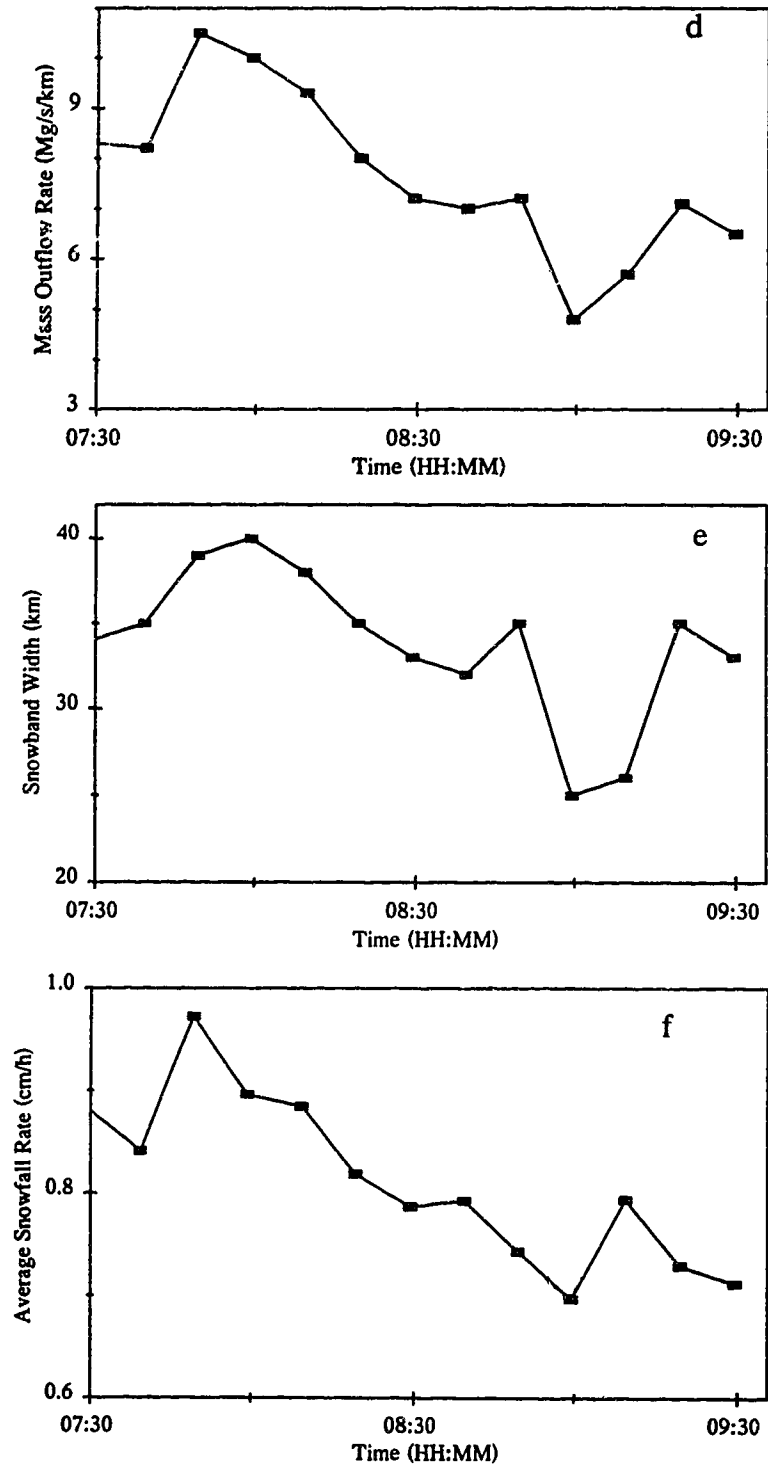


Figure 3.9: Evolution of budget parameters for 16 October 1991. Plots of: (d) Mass outflow rate  $dO/dt$ ; (e) Snowband width  $W$ ; and (f) Average snowfall rate  $R_{avg}$ .

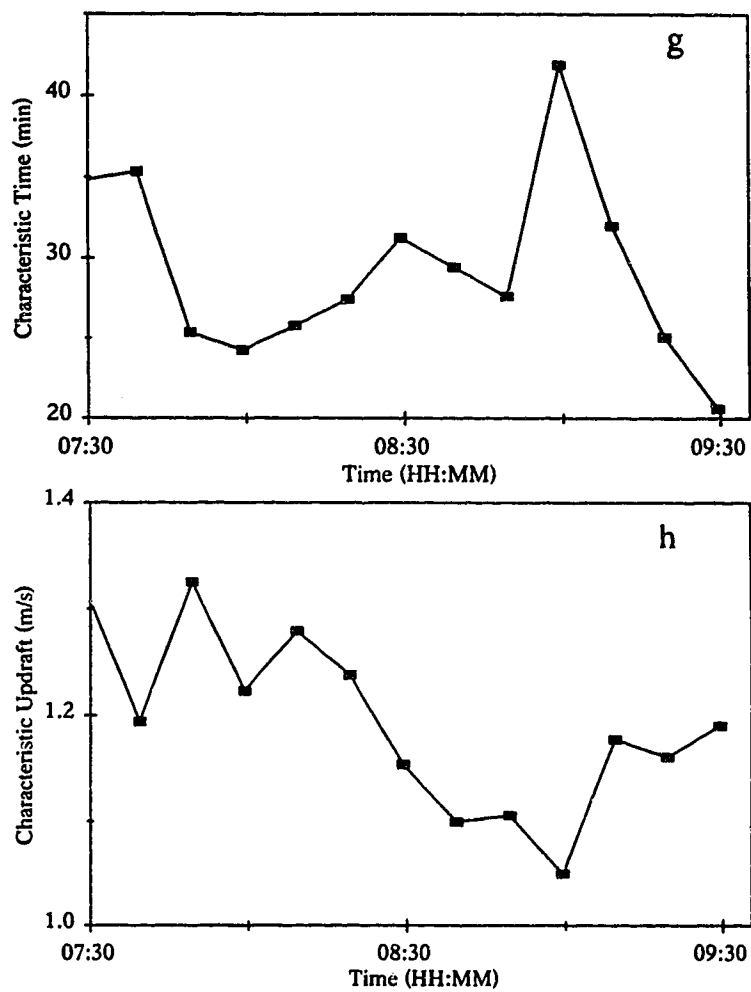


Figure 3.9: Evolution of budget parameters for 16 October 1991. Plots of (g) characteristic time  $\tau$  and (h) characteristic updraft  $U$ .

updraft could no longer support the snow,  $dO/dt$  increased while  $P$  decreased. The time lag between the peaks in  $P$  and  $dO/dt$  for the half hour leading up to the mature stage indicated that most of the snow was forming in the mid to upper levels of the snowband. Most likely snow formation occurred where CSI was observed (approximately between 3 km and 5 km AGL). However, after the snowband reached its mature stage, no discernible correlation existed between  $dO/dt$  and  $P$ .

The time evolution of  $R_{avg}$  (Fig. 3.9f) corresponded with the band evolution observed on the CAPPI imagery (Fig. 3.7). Maxima and minima appeared to be weakly correlated with  $P_{avg}$ , but the amplitude of the peaks and troughs were different. With a range from 0.7 cm/h to 1.0 cm/h, and a time average of 0.8 cm/h, the evolution of  $R_{avg}$  appears to be quasi-steady.

The time evolution of the characteristic time  $\tau$  (Fig. 3.9g) show maxima at 0740 UTC and 0900 UTC which may have been caused by strong updrafts temporarily suspending the snow in the cloud. This seems to be the case at 0740 UTC where a high total snow content was occurring with a minimum in the mass outflow rate. The maximum at 0900 UTC appears to be related to a drop in the mass outflow rate suggesting that the band may have been weakening. Even with these peaks, the evolution of  $\tau$  appears to be quasi-steady. With an average  $\tau$  of 29 minutes, aggregation and accretion would most likely be the dominate snow growth mechanism within the band.

The time variation of the characteristic updraft  $U$  (Fig. 3.9h) can also be considered quasi-steady. The average  $U$  of 1.2 m/s for the time period agreed with the fall speed of aggregated snow. Since significant portion of the snow appears to have formed in the CSI layer above 3 km,  $U$  would

be representative of the updraft required to maintain snow generation within the band.

**a) Cumulative amount of precipitation generated**

The accumulated outflow  $O(t)$  and the accumulated amount of snow generated  $G(t)$  is shown in Fig. 3.10. The two curves appear rather smooth. The jump in the first ten minutes can be attributed to the exclusion of data between 0700 UTC and 0730 UTC when the band was initially developing. The total snow generated is much larger than the maximum  $P(t)$  present at any stage. At the end of the life cycle of the snowband,  $O(t)$  converges to  $G(t)$  since  $P(t) \rightarrow 0$ .

From the  $G(t)$  of 63.5 Gg/km, the latent heat of sublimation released by the snowband was 178 TJ/km (1 TJ =  $10^9$  kJ). Larochelle (1991) determined the rate of latent heat released from snow that fell from a Pacific snowstorm. Larochelle found that the storm released latent heat at a rate of 75 TW, which over a 2 hour period gives  $5.4 \times 10^5$  TJ. Assuming our snowband has a length of 200 km, the latent heat released was about 7% of the storm investigated by Larochelle. Although the morphology was similar for the two storms, the values of latent heat released may be in error by a factor of 2 or more for both cases.

### 3.7 Snow budget sensitivity analysis

In determining the properties of a snowband from a snow analysis, corrections and settings were made to the radar data. It was assumed throughout the analysis that the budget parameters were insensitive to small variations in settings such as the reflectivity threshold  $Z_r$  (dBz), the cross-section azimuth angle  $\theta$ , and the cloud base height. The loss of data due to the removal of ground clutter was assumed to have a minimal affect on the budget quantities. The following sections will examine the sensitivity of

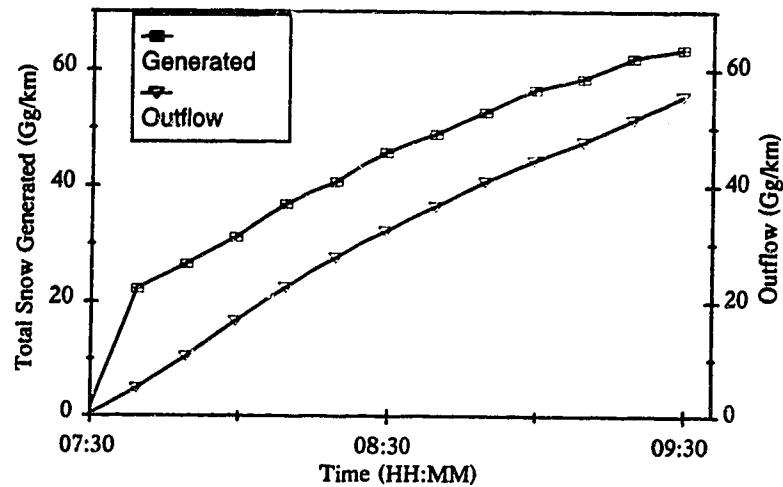


Figure 3.10: Outflow  $O(t)$  and cumulative amount of snow generated  $G(t)$  by the warm frontal snowband.

different factors on the snow budget analysis. Although the sensitivity analysis will be case dependent, an idea of the potential error size associated with each factor can be assessed.

#### a) Removal of ground clutter

Ground clutter existed below 1.5 km at a distance of 15 km and 55 km from the radar. Each area was about 5 km to 10 km wide. Before snow budget quantities could be calculated, these ground clutter areas were removed. Since ground clutter occurred close to the earth's surface, the data lost due to its removal could significantly affect the mass outflow rate  $dO/dt$ .

Budget quantities in section 5 were determined over two cross-section band widths, 25 km and 50 km (Table 3.3). At a range of 15 km the area of ground clutter was below the height of the cloud base of 0.5 km. Therefore, no data was lost in this area for either band width. The area of ground clutter at 55 km only affected budget quantities determined

over the 50 km cross-section range. With the removal of ground clutter, nine potential reflectivity measurements were excluded. Since little or no snow from the snowband fell into this region at 55 km (Fig. 3.8), the potential loss in  $dO/dt$  was less than 5%.

#### ***b) Reflectivity threshold***

To distinguish the snowband from the ambient snow field, a reflectivity threshold  $Z_t$ (dBz) of 25 dBz was used. The value of  $Z_t$ (dBz) was determined from a contour analysis of a vertical reflectivity cross-section sampled at 0830 UTC (Fig. 3.8). Since the time evolution of the budget quantities showed some variability over the two hour period, the choice of  $Z_t$ (dBz) may not be valid over the entire time period.

Snow budget quantities were determined for various  $Z_t$ (dBz) values starting at the radar minimum threshold value of 13.5 dBz (Table 3.5). With the exception of  $R_{avg}$  and  $P_{avg}$ , all snow budget quantities were at their maximum when  $Z_t$ (dBz) was at 13.5 dBz. The low  $R_{avg}$  and  $P_{avg}$  were caused by the dampening effect of including the ambient snow which consisted of low reflectivity values. Including the ambient snow in the snow budget calculations produced a higher  $U$  than when it was isolated from the snowband. This may be due to differences in the geometry of the snowband and the snow field which would then affect how  $R_{avg}$  and  $P_{avg}$  are calculated.

Table 3.5: Snow budget analysis at 0830 UTC for various reflectivity threshold values. Budget determined for a band cross-section width of 50 km and 25 km.

Cross-section	Z <sub>t</sub> dBz	dO/dt Mg/s km <sup>-1</sup>	W km	R <sub>avg</sub> cm/h	P Gg/km	A km <sup>2</sup>	P <sub>avg</sub> g/m <sup>3</sup>	τ min	U m/s
50 km	13.5	8.1	41	0.7	22.8	182	0.13	47	1.6
	15	8.1	41	0.7	22.1	167	0.13	45	1.5
	17	8.1	41	0.7	21.4	155	0.14	44	1.4
	19	8.1	41	0.7	20.0	136	0.15	41	1.3
	21	8.1	41	0.7	18.6	119	0.16	38	1.3
	23	7.9	39	0.7	15.8	91.2	0.17	33	1.2
	25	7.2	33	0.8	13.5	71.5	0.19	31	1.2
	27	6.1	25	0.9	10.8	52.2	0.21	30	1.2
	29	4.6	17	1.0	7.3	31.6	0.23	26	1.2
	31	2.4	7	1.2	4.3	16.6	0.26	29	1.3
25 km	13.5	6.0	25	0.9	15.9	108	0.15	44	1.6
	15	6.0	25	0.9	15.5	100.	0.15	43	1.6
	17	6.0	25	0.9	15.2	94.5	0.16	42	1.5
	19	6.0	25	0.9	14.6	86.4	0.17	40	1.4
	21	6.0	25	0.9	14.0	80.0	0.18	39	1.4
	23	6.0	25	0.9	13.0	69.5	0.19	36	1.3
	25	6.0	25	0.9	12.0	61.4	0.20	33	1.2
	27	5.7	23	0.9	10.5	50.5	0.21	31	1.2
	29	4.6	17	1.0	7.2	31.0	0.23	26	1.2
	31	2.4	7	1.2	4.3	16.6	0.26	29	1.3



As the reflectivity threshold increased to about 23 dBz,  $R_{avg}$  showed little change while  $P_{avg}$  increased steadily. The slow change in  $R_{avg}$  helps to explain why  $U$  was larger in stratiform precipitation rather than in the snowband. Beyond 23 dBz,  $U$  became constant while  $R_{avg}$  and  $P_{avg}$  continued to increase. The point where  $U$  becomes constant (23 dBz to 25 dBz), could be used to help determine  $Z_t$  (dBz) since the effects of the stratiform precipitation on snow budget quantities appear to be negligible.

The characteristic and average properties of the snowband determined for the 25 km and the 50 km cross-section regions indicated a difference of about 15% (Table 3.3). This difference may have been caused by a reflectivity threshold that was set too low. The difference between characteristic and average properties of the snowband disappeared when  $Z_t$  (dBz) increased to 29 dBz. However, over 50% of the snow mass within the snowband is neglected and budget quantities may not reflect the true nature of the snowband.

Assuming that over the time period,  $Z_t$  (dBz) was correct to within  $\pm 2$  dBz, the maximum variation with snow budget quantities would be  $\leq 20\%$  for the 50 km cross-section and  $\leq 15\%$  for the 25 km cross-section.

**c) Cross-section azimuth angle**

A snow budget analysis of the snowband was based on the assumption of slab-symmetry. The sensitivity of the cross-section azimuth angle was assessed by calculating snow budget quantities for a range of azimuth angles from 170° to 180° (Table 3.6). Only a 50 km band cross-section was analyzed since a 25 km analysis did not add any additional information. The mean and the standard deviation were also calculated for each budget parameter. The standard deviation was less than 10% of the mean for all parameters. All budget quantities were within one standard deviation from 172° to 178° and within 20% of the mean over the 10° range. Thus minor fluctuations of the band orientation should not significantly affect the time evolution of snow budget quantities.

Table 3.6: Variation of snow budget parameters with the cross-section azimuth angle at 0830 UTC. Budget quantities determined for a 50 km band cross-section.

Azimuth degrees	$dO/dt$ Mg/s km <sup>-1</sup>	W km	$R_{avg}$ cm/h	P Gg/km	A km <sup>2</sup>	$P_{avg}$ g/m <sup>3</sup>	$\tau$ min	U m/s
170	5.6	23	0.87	13.0	66	0.196	39	1.23
171	6.3	31	0.73	13.1	67	0.196	35	1.04
172	6.9	31	0.80	13.3	70	0.191	32	1.17
173	7.2	33	0.79	13.6	70	0.194	31	1.13
174	7.7	35	0.80	13.2	70	0.189	29	1.17
175	7.2	33	0.79	13.5	71	0.189	31	1.15
176	6.7	30	0.81	13.1	70	0.188	33	1.20
177	6.3	29	0.78	13.2	68	0.192	35	1.13
178	6.3	29	0.79	13.5	71	0.191	36	1.14
179	6.6	30	0.79	14.3	77	0.185	36	1.19
180	6.3	29	0.79	16.1	85	0.189	42	1.16
Mean	<u>6.6</u>	<u>30</u>	<u>0.79</u>	<u>13.6</u>	<u>71</u>	<u>0.191</u>	<u>34</u>	<u>1.15</u>
Std. Dev.	<u>0.6</u>	<u>3</u>	<u>0.03</u>	<u>0.9</u>	<u>5</u>	<u>0.003</u>	<u>4</u>	<u>0.05</u>

**d) Cloud base height**

To determine the total snow content and the mass outflow rate, reflectivity data at or above the height of the cloud base of 0.5 km were used. The sensitivity of the cloud base height on the snow budget quantities was assessed by determining budget quantities over a range of heights from 0.4 km to 0.6 km (Table 3.7). At a cloud base height of 400 m, ground clutter affected a larger portion of the snowband beyond 45 km. For this reason the snow budget quantities were examined only for the 25 km band width. If the estimate of the height of the cloud base was in error by  $\pm 0.1$  km, the error in snow budget quantities was less than 20%. Thus a non-uniform cloud deck should not significantly affect the snow budget analysis.

Table 3.7: Variations of water budget parameters with cloud base height at 0830 UTC. Budget quantities determined for a 25 km band 1 cross-section.

Base Height	$dO/dt$ Mg/s km <sup>-1</sup>	W km	$R_{avg}$ cm/h	P Gg/km	A km <sup>2</sup>	$P_{avg}$ g/m <sup>3</sup>	$\tau$ min	U m/s
400	6.7	24	1.0	12.6	64	0.20	31	1.4
450	6.5	25	0.9	12.4	63	0.20	32	1.3
500	6.0	25	0.9	12.0	61	0.20	33	1.2
550	5.5	24	0.8	11.8	61	0.20	36	1.2
600	4.9	21	0.9	11.6	59	0.20	39	1.2

## 4 Analysis of a Wide Cold Frontal Snowband

### 4.1 Introduction

An Arctic cold front passed through central Alberta on 13 February 1994 and spawned several snowbands. The bands were observed by radar just to the south of the city of Edmonton and were oriented in west to east lines. Snowfalls associated with these bands covered a small area of central Alberta with snow accumulations near 4 cm (Fig. 4.1).

The objective of this chapter is to determine the precipitation production of the largest snowband using radar observations. The potential of Conditional Symmetric Instability (CSI) as a band formation mechanism will also be examined. The organization of this chapter is as follows. Section 2 presents the large-scale flow pattern leading to the development of the snowbands. Section 3 examines the thermodynamic profile of the airmass and determines the potential for CSI. Section 4 presents the evolution and vertical structure of the snowband. Precipitation production of the snowband is shown in sections 5.

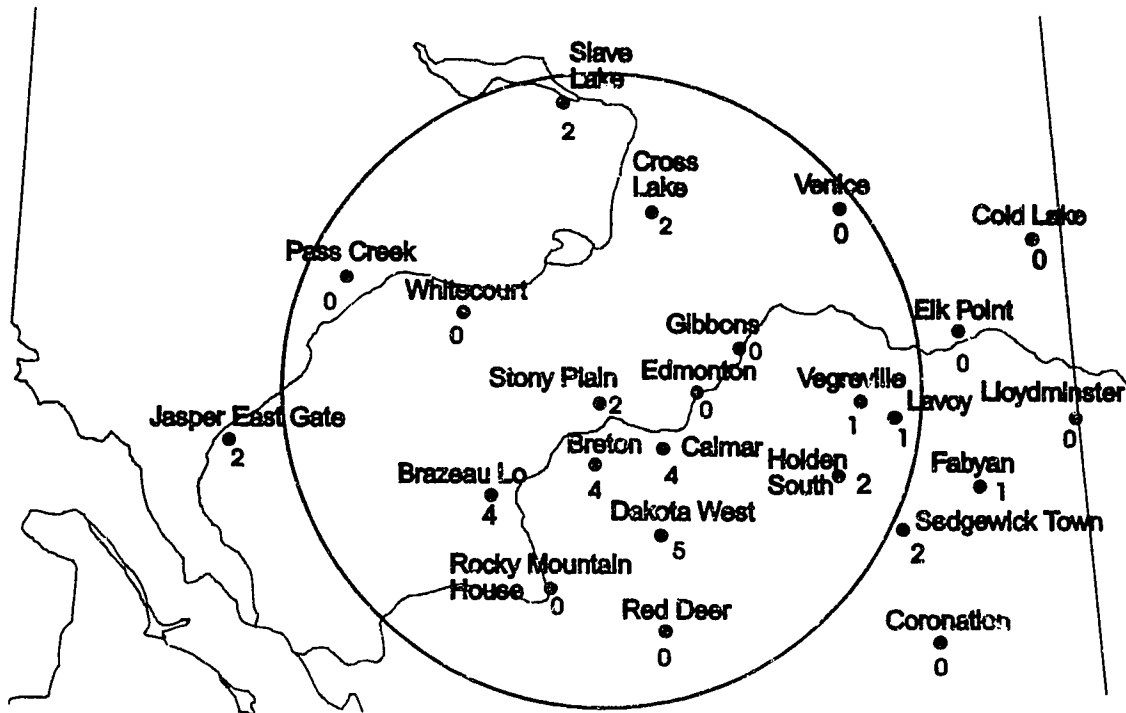


Figure 4.1: Snowfall accumulations (cm) across central Alberta for 13 February 1994. The circle represents the outer range (220 km) of the Carvel radar.

#### 4.2 Synoptic overview

With the building of an Arctic high pressure system over the southern Mackenzie Valley on 13 February 1994, the Arctic airmass surged southward. The cold front pushed southward at 25-40 km/h and had a temperature gradient of about 8°C/100 km. No cloud existed along the leading edge of the front but a distinct wind shift from the south-west to the north existed. As the front moved southward it became stalled over western Alberta, probably because the Arctic airmass was not deep enough to cross the Rocky Mountains. The 0000 UTC 14 February 1994 (evening of February 13) surface analysis shows the 6 hour history of the Arctic high pressure system over the Mackenzie valley and the position of the Arctic cold front over south-central Alberta (Fig. 4.2a). The sharp temperature gradient at the surface

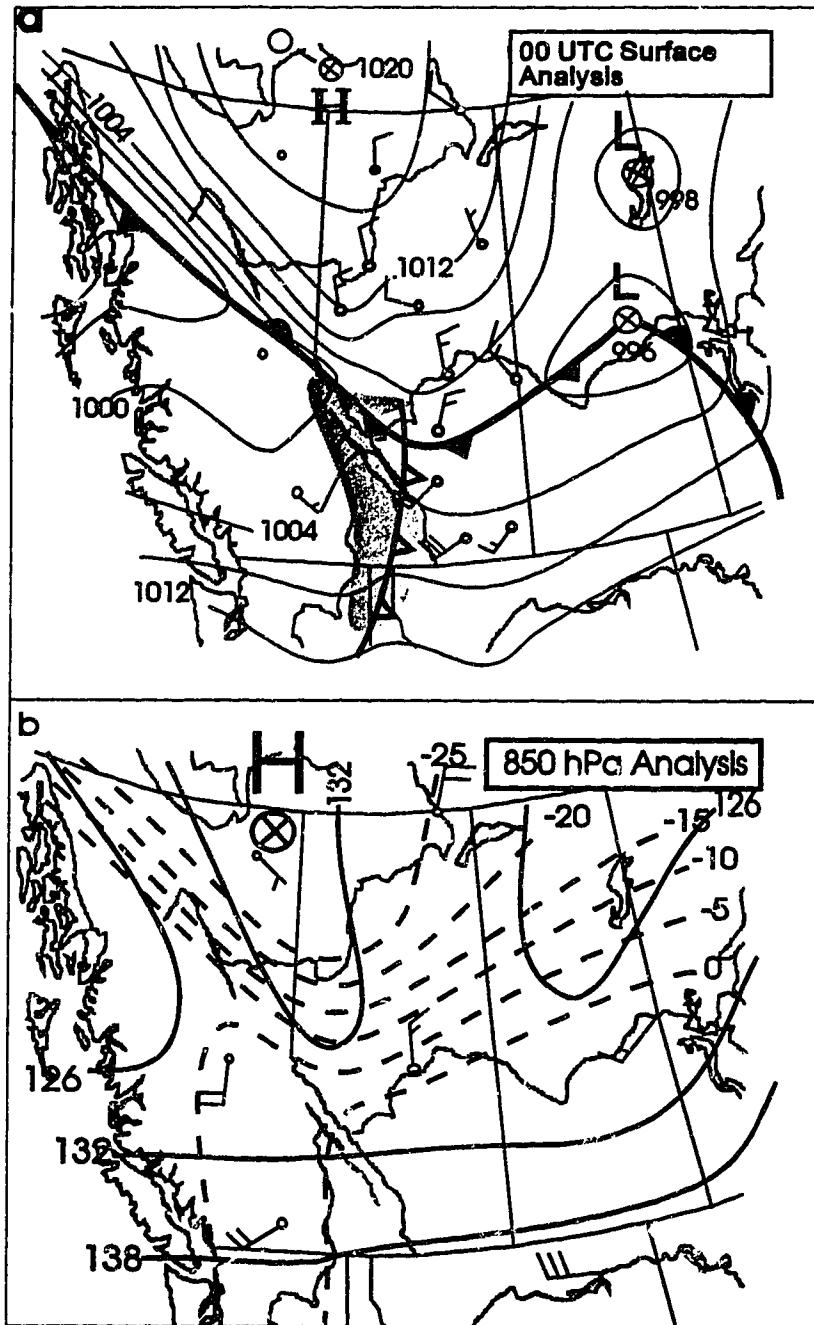


Figure 4.2: 0000 UTC 14 February 1994 surface analysis (a) with mean sea level pressure contours (every 4 hPa) and snow area shaded grey. 850 hPa analysis (b) with solid lines representing height contours (dm) and dashed lines representing isotherms ( $^{\circ}\text{C}$ ). Wind direction and speed at select stations using the conventional station model (half barb represents 5 Kt and full barb 10 Kt).

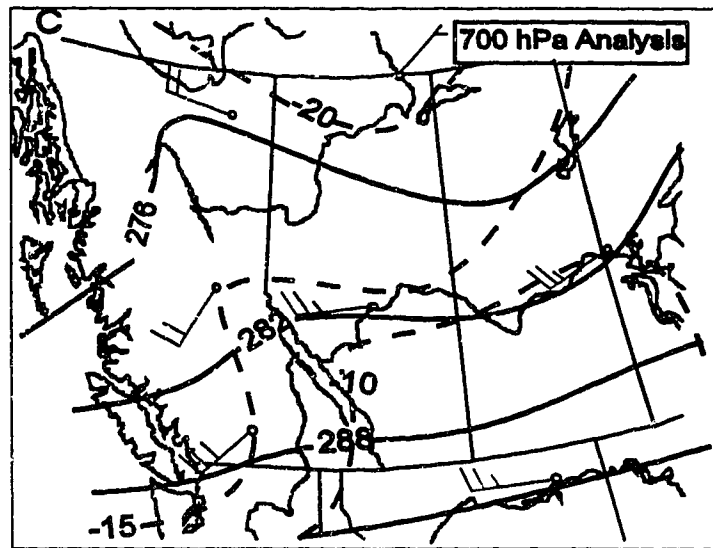


Figure 4.2: 0000 UTC 14 February 1994 700 hPa analysis (c) with solid lines representing height contours (dm) and dashed lines representing isotherms (°C). Wind direction and speed at select stations using the conventional station model. ,

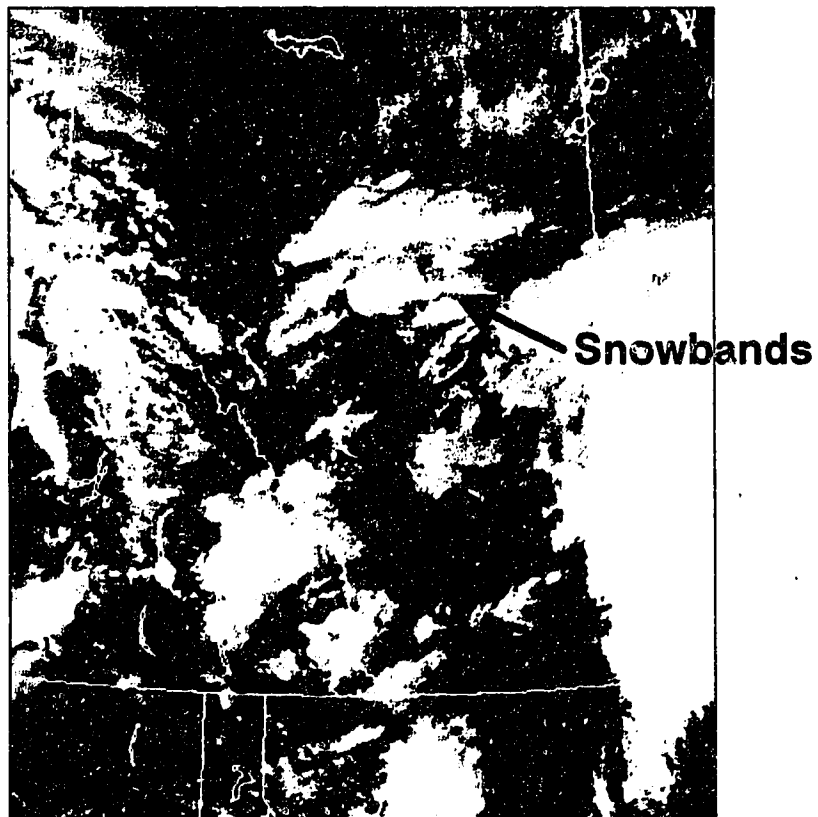


Figure 4.3: IR-satellite image at 0220 UTC 14 February 1994 of the southern two-thirds of Alberta.

was also supported at 850 hPa (Fig. 4.2b). The circulation pattern over Alberta was rather weak at this level. The weakness of the baroclinic zone at 700 hPa indicated that the Arctic airmass was shallow (Fig. 4.2c). The westerly flow across the southern half of Alberta did not support the southerly push of Arctic air, but the cold air advection over eastern British Columbia indicated a weak upper level Pacific cold front. This cold front was moving eastward at about 60 km/h and is shown on the surface analysis as a cold front with unshaded frontal barbs.

From 0000 UTC to 0300 UTC, the Arctic airmass continued to surge southward through Alberta. A number of snowbands formed north of the Arctic cold front over central Alberta. The satellite image (Fig. 4.3) shows the alignment of the snowbands.

#### 4.3 Atmospheric stability

The thermodynamic structure of the atmosphere was determined from data collected by the 0000 UTC 14 February 1979 radiosonde. The sounding, plotted in Fig. 4.4, was representative of the atmosphere just prior to the band formation. A frontal inversion existed between 860 hPa and 830 hPa. Above the frontal inversion, a wet bulb potential temperature  $\theta_w$  of 4°C indicated a warm, moist Pacific airmass, while below the inversion, the  $\theta_w$  of -6°C indicated a cold, dry Arctic airmass. The sounding was stable to upright cumulus convection except in the first 40 hPa and between 760 hPa and 590 hPa, where it was potentially unstable. Due to the sharp frontal inversion, no development could occur in the layer close to the surface. The layer from 700 hPa to 500 hPa was fairly moist (RH ~70%) so it is likely that potential for instability will be released once the layer is lifted to its level of saturation.



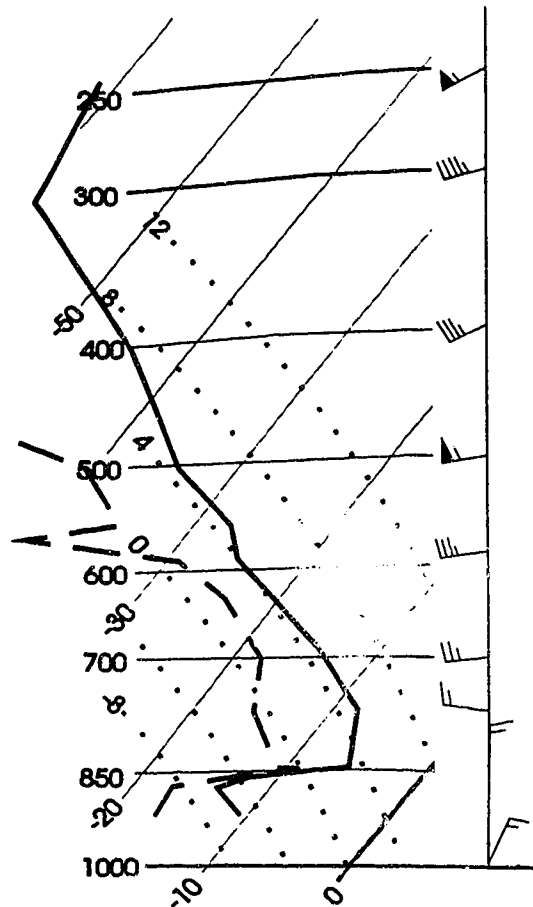


Figure 4.4: Tephigram of 1200 UTC, 14 February 1994 sounding taken at Stony Plain (WSE) with temperature (thick solid line) and dew point (dashed line). Horizontal lines are isobars (hPa), straight lines skewed to the right are isotherms ( $^{\circ}\text{C}$ ), and dotted lines are pseudo-adiabats ( $^{\circ}\text{C}$ ). Observed winds with height on the right hand side using the conventional station model (solid flag represents 50 Kt, full barb is 10 Kt and half barb 5 Kt).

The wind profile is shown on the right hand side of Fig. 4.4. Winds backing with height from surface to 700 hPa indicated cooling by advection. The strongest cooling occurred below 750 hPa as the radiosonde past through the frontal zone. Above 750 hPa the winds were roughly unidirectional and increased with height up to 500 hPa. Thus

the condition of strong unidirectional shear required for the release of CSI was only met in this layer.

**a) CSI analysis**

Potential for the release of CSI exists in a given layer of air when the Richardson number for ice saturation  $Ri_{ice}$  is less than 1. The special condition of Convective Instability occurs when  $Ri_{ice} < 0$ . Using the 0000 UTC 14 February 1994 sounding data (Table 4.1),  $Ri_{ice}$  was determined for various layers using the method described in chapter 2. Since conditions for slantwise overturning could only occur in one layer, the thermal shear of  $265^\circ$  was determined using winds at 700 hPa and 500 hPa.

In chapter 3, both the ice and water phase Richardson numbers were determined. For values between zero and one, the difference between using water or ice phase was within  $\pm 0.1$ . However it is not known whether this holds true for Convective Instability. Thus both  $Ri_{ice}$  and  $Ri_m$  (moist Richardson number) were determined (Table 4.2). The analysis reveals the following:

- ♦ The airmass was convectively unstable between 765 hPa and 590 hPa and moist Symmetrically unstable between 590 hPa and 500 hPa.
- ♦ The occurrence of Convective Instability is a rare event in winter. A climatological study of winter precipitation (i.e. December through February) in Alberta by Reuter and Aktary (1995) indicated that the potential for Convective Instability was associated with 10% of precipitation events.
- ♦ For Richardson numbers less than 1,  $Ri_{ice}$  and  $Ri_m$  produced similar results with values within  $\pm 0.1$ . Thus  $Ri_m$  provides an adequate indication of airmass stability, even when temperatures are below  $0^\circ\text{C}$ .

- ♦ Convective Instability also occurred in the first atmospheric layer. Since the frontal inversion firmly capped this layer, no cloud development could occur.

Studies have shown that Convective and Symmetric Instability can both combine to form a precipitation band (e.g. Jascourt et al. 1988; Reuter and Nguyen 1993; Reuter and Yau 1993). Although both types of convection have different time scales (i.e. minutes for Convective and hours for Symmetric instability), Emanuel (1980) suggested that latent heat released in the free-convective updraft could drive slantwise overturning associated with the release of moist Symmetric Instability. From observations of convective bands forming over Louisiana, Jascourt et al. (1988) found that once convective towers became deep enough to reach the layer where CSI existed, slantwise overturning would act to organize the convective cells into bands. It is possible that the organization of precipitation by Convective-Symmetric Instability may have taken place in the development of our snowband since the bands were oriented with the thermal shear determined between 700 hPa and 500 hPa.

Table 4.1: Analysis of the 0000 UTC 14 February 1994 atmospheric sounding. Listed are the temperature  $T$ , dewpoint  $T_d$ , frost point  $T_f$ , ice saturation vapour pressure  $e_i$ , ice mixing ratio  $w_i$ , the ice potential temperature  $\theta_i$ , the lifting condensation level  $T_{LCL}$ , the ice equivalent potential temperature  $\theta_{ei}$ , and the ratio of the ice adiabatic lapse rate to the dry adiabatic lapse rate  $\Gamma_{ice}/\Gamma_d$ .

Press hPa	T °C	$T_d$ °C	$T_f$ °C	$e_i$ hPa	$w_i$ g/kg	$\theta_i$ K	$T_{LCL}$ K	$\theta_{ei}$ K	$\Gamma_{ice}/\Gamma_d$
913	-10.3	-16.3	-14.4	2.53	1.7	270	258	275	0.74
872	-13.5	-16.7	-14.8	1.90	1.4	270	258	274	0.78
765	-8.1	-15.1	-13.4	3.07	2.5	286	259	294	0.67
700	-13.5	-17.5	-15.5	1.90	1.7	287	257	293	0.74
590	-24.5	-28.6	-25.5	0.66	0.7	289	247	291	0.86
500	-33.9	-39.9	-35.7	0.25	0.3	292	237	293	0.92
400	-44.3	-61.3	-55.4	0.08	0.1	297	216	298	0.97

Table 4.2: Stability analysis for the 0000 UTC 14 February 1994 atmospheric sounding. Listed are the relative humidity RH, the vertical gradient of the zonal wind  $dv_z/dz$ , the ice Brunt-Väisälä frequency  $N_i^2$ , the ratio  $\eta_g/f$ , the ice Richardson number  $Ri_{ice}$  and the moist Richardson number  $Ri_m$ . Convective Instability, Conditional Symmetric Instability and Absolute Stability are denoted by CI, SI and AS, respectively.

Layer hPa	RH %	$dv_z/dz$ $\times 10^{-3} s^{-1}$	$N_i^2$ $\times 10^{-4} s^{-2}$	$\eta_g/f$	$Ri_{ice}$	$Ri_m$	Stability Condition
sfc-872	76	7.4	-0.9	1.1	-1.4	-1.4	CI
872-765	57	6.8	6.5	0.9	8.8	9.3	AS
765-700	71	9.3	-0.5	0.8	-0.4	-0.3	CI
700-590	68	4.9	-0.4	1.0	-1.3	-1.4	CI
590-500	54	7.7	0.4	1.2	0.7	0.6	SI
500-400	25	-7.1	1.1	1.3	2.8	2.6	AS

#### 4.4 Radar analysis

##### a) *Evolution of the snowband*

Observations from the C-band radar located in Carvel, indicated that the snowbands existed for about 6 hours. Fig. 4.5 depicts the half-hourly CAPPI radar imagery from 0100 UTC to 0300 UTC.

At 0100 UTC 14 February 1994, four snowbands were identified on CAPPI radar imagery. Three of these bands ranged from 5 km to 10 km in width and were spaced about 50 km apart. These bands, located 50 km north, 5 km south and 60 km south of the radar indicated snowfall rates of 0.4 cm/h with a few convective cells giving 0.8 cm/h. The snowband located 60 km south of the radar had a south-west to north-east orientation and more embedded convective cells. The fourth band, about 30 km south of the radar had a width of about 20 km and snowfall rates of 0.4 cm/h to 0.8 cm/h. During the next 2 hours, the magnitude of the snowfall rate fluctuated while this band moved through various stages of its life span. By 0130 UTC, the mature stage was reached, characterized by higher snowfall rates (0.8 cm/h to 1.6 cm/h) and by a sharper cross-band reflectivity gradient. The snowband widened over the next half hour to 30 km and snowfall rates weakened to 0.4 cm/h to 0.8 cm/h. Between 0230 UTC and 0300 UTC, the snowband began to dissipate as another band developed 60 km south of the radar. Of the narrow snowbands, only one lasted up to 0200 UTC (located 70 km south of the radar). This band had widened to about 20 km and intensified with steady snowfall rates of 0.4 cm/h to 0.8 cm/h.

Over the two hour period convective cells embedded in each snowband propagated along the length of the band at 30-40 km/h. The snowbands themselves were tracking in a east-southeastward direction around 30 km/h, giving a

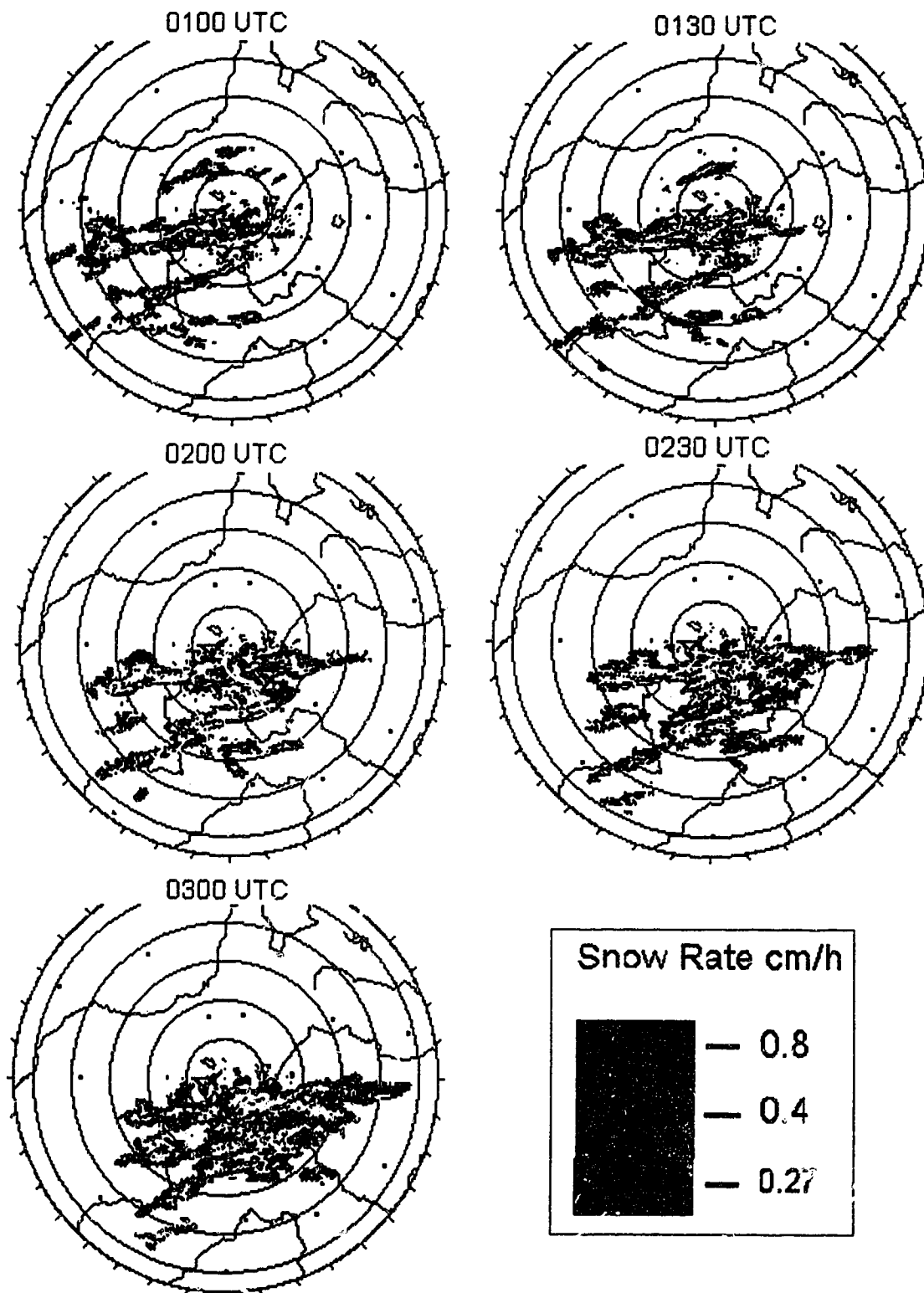


Figure 4.5: CAPPI 1.0 km imagery of the snowbands on 14 February 1994 from 0100 UTC to 0300 UTC. Image rings spaced 40 km.

southward motion of about 20 km/h.

The organization and orientation of the snowbands were found to be similar to a wide cold frontal rainband (band type 4, Fig. 1.1) reported by Matejka et al. (1980), Hobbs et al. (1980), Parsons and Hobbs (1983a,b), and Sienkiewicz et al. (1989). Hobbs et al. (1980) found that precipitation within a wide cold frontal rainband formed above the frontal zone. The rainband also moved faster than the surface front, probably because of differential advection. The movement of the snowbands towards the cold front did not occur in our case. The distinct directions of the flow above (westerly) and below the frontal zone (northerly) advected the snowbands in an east-southeasterly direction.

#### ***b) Snowband vertical cross-section***

For the 20-30 km wide snowband (~30 km south of the radar), the CAPPI imagery (Fig. 4.5) indicated that the snowfall intensity varied only slightly in the along band direction (i.e. the precipitation field was close to slab-symmetric). Thus a vertical cross-section of radar reflectivity field (perpendicular to the band) was representative of the entire band. The vertical structure of ice reflectivity factor  $Z_1$  (dBz), was obtained from the 0830 UTC data along an azimuth of 175°. The radar data were interpolated to a uniform Cartesian grid using the Cressman interpolation method (Cressman 1959; Haltiner and Williams 1980, pg. 356). The horizontal and vertical resolution of the grid was 1 km and 100 m, respectively.

Fig. 4.6 shows the vertical section of the  $Z_1$  (dBz) field. The snowband is depicted by a 32 dBz core 30 km from the radar and by a precipitation region which slopes back towards the Arctic cold front. The slope in the precipitation was probably caused by the wind shear zone across the frontal zone. With south-westerly winds above the

frontal zone (~1 km AGL) and northerly winds below, precipitation would be advected to the right as it falls through the frontal zone. Also a portion of the echoes 20 km to the south of the radar can be attributed to the narrow snowband that merged with the wider snowband at 0200 UTC.

With precipitation measured up to 5 km AGL (Above Ground Level), Convective and moist Symmetric Instability were most likely realized. Thus Symmetric Instability probably helped to organize convective cells into a banded structure.

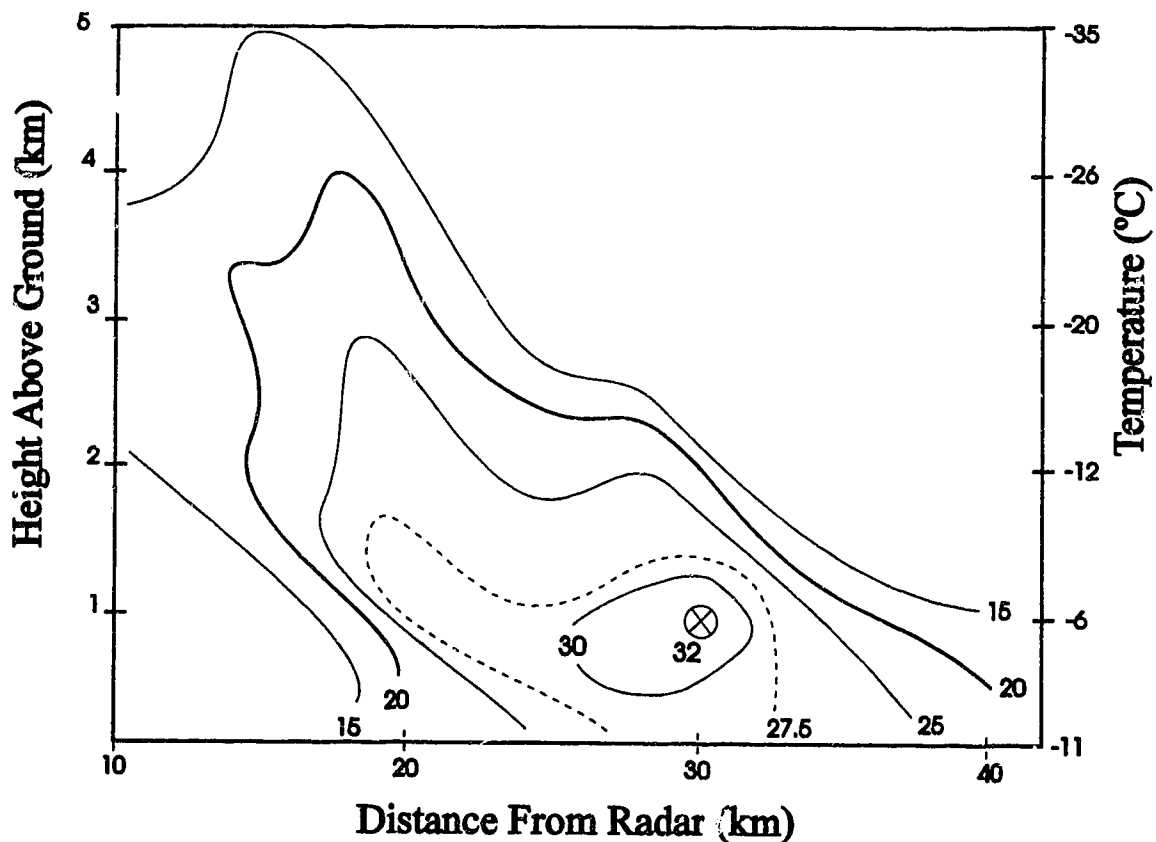


Figure 4.6: Contour analysis of the cold frontal snowband vertical cross-section at 0200 UTC. Contours every 5 dBz.



#### 4.5 Precipitation production

To improve our understanding of the formation of precipitation in the snowband, the evolution of the budget quantities  $dO/dt$ ,  $P$ ,  $R_{avg}$ ,  $P_{avg}$ ,  $\tau$ , and  $U$  were determined from 0100 UTC to 0300 UTC. Budget quantities, plotted in Fig. 4.7, were evaluated over a 40 km band cross-section (i.e. from 10 km to 50 km) along an azimuth angle of  $175^\circ$ . A reflectivity threshold  $Z_r$  (dBz) of 20 dBz and a cloud base height of 400 m AGL were used for the integrations. The cloud base height was determined from synoptic observations taken at the Edmonton International Airport. Radar data were corrected for ground clutter which existed between 10 km and 20 km below 1 km AGL. Since the northern edge of the band on the CAPPI imagery (Fig. 4.5) was about 20 km from the radar, the percentage of the snowband lost due to the removal of ground clutter on budget quantities was negligible. A second narrow snowband was also observed on the CAPPI imagery about 10 km south of the radar until 0200 UTC. Since it was too difficult to separate the two bands within the cross-section, reflectivity data associated with this band was included in the snow budget analysis. A  $0.5^\circ$  scan radar image indicated that precipitation was evaporating below the narrow snowband suggesting that it was weak.

The evolution of the band on the CAPPI radar imagery indicated that the snowband was at its mature stage at 0130 UTC. The snowband had a mass outflow rate ( $dO/dt$ ) of  $4.0 \text{ Mg/s km}^{-1}$  ( $1 \text{ Mg} = 1 \times 10^3 \text{ kg}$ ), an average snowfall rate of ( $R_{avg}$ )  $0.8 \text{ cm/h}$ , a total snow content ( $P$ ) of  $5.5 \text{ Gg/km}$  ( $1 \text{ Gg} = 1 \times 10^6 \text{ kg}$ ), an average snow content ( $P_{avg}$ ) of  $0.15 \text{ g/m}^3$ , a characteristic time ( $\tau$ ) of 23 minutes and a characteristic updraft ( $U$ ) of  $1.4 \text{ m/s}$ . With a life span of about 4 hours,  $R_{avg}$  was in good agreement with recorded snowfalls (Fig. 4.1). The peak in  $dO/dt$  and  $R_{avg}$  occurred at

0130 UTC while a maxima in  $P$  and  $P_{avg}$  occurred 10 minutes earlier. Thus changes in the generation of snow took about 10 minutes to appear in the band outflow, suggesting that snowflakes formed aloft in the convectively unstable region of the snowband. Assuming the snowband was quasi-steady, the value of  $U$  and  $\tau$  suggested that snowflakes formed by accretion and aggregation (Young 1993, pg. 218, 240, 274). Convective clouds forming as a result of the release of Convective Instability in the layer from 765 hPa to 590 hPa (about 1.5 km to 4 km AGL) would have supported this type of snow growth mechanism.

The time evolution of  $P$  and the cross-sectional area  $A$  (Fig. 4.7a,b) displayed similar trends with maxima and minima coinciding. Although a maxima in  $P$  and  $A$  occurred 10 minutes prior to the mature stage, the peak in  $P$  and  $A$  occurred at 0230 UTC. Thus the size of the snowband was greatest at 0230 UTC, just prior to its dissipation.

The time history of  $P_{avg}$  (Fig. 4.7c) had its peak value of  $0.15 \text{ g/m}^3$  at 0120 UTC (i.e. just prior to the snowband's mature stage). The drop in  $P_{avg}$  over the next 30 minutes coincided with the drop in  $P$  and  $A$  but with the minimum occurring 10 minutes later at 0150 UTC. This lag in the minimum was due to  $A$  increasing in size while  $P$  remained relatively steady. The lack of a maxima in  $P_{avg}$  at 0230 UTC suggested that although the snowband was at its greatest size at this time, the intensity of the snow generation (characterized by peaks in  $P_{avg}$ ) was weaker than just prior to the mature stage. A higher updraft would support a higher snow generation rate since more water vapour would be available. With a variation of  $\pm 0.02 \text{ g/m}^3$  about the time average of  $0.13 \text{ g/m}^3$ , the evolution of  $P_{avg}$  appears to be quasi-steady.

The plots of  $dO/dt$  and  $W$  (Fig. 4.7d,e) indicated that over the first 30 minutes both  $dO/dt$  and  $W$  quadrupled in size. However, whereas  $dO/dt$  remained fairly uniform after this time,  $W$  continued to increase to its maximum value of 27 km at 0240 UTC. The maximum in  $dO/dt$  and  $W$  at 0130 UTC corresponded with the mature stage of the snowband. The second maximum at 0240 UTC corresponded with a larger snowband. Maxima and minima in  $dO/dt$  lagged similar maxima and minima in  $P$  by ten minutes, suggesting snowflakes were being formed in the convective region of the snowband.

The evolution of  $R_{avg}$  (Fig. 4.7f) showed a peak at 0130 UTC which coincided with the band's mature stage. The second maximum at 0230 UTC appears to be related to the peak values in  $P$  and  $A$  when the band was at its largest size. The minimum at 0200 UTC corresponded with the reflectivity cross-section azimuth angle of  $175^\circ$  lying between two stronger echoes (Fig. 4.5). Except for an approximate 10 minute lag, the maxima and minima in the time evolution of  $R_{avg}$  and  $P_{avg}$  were similar. With a variation of  $\pm 0.2$  cm/h about the time average of 0.6 cm/h, the evolution of  $R_{avg}$  appears to be quasi-steady.

The time evolution of the characteristic time  $\tau$  is shown in Fig. 4.7g. From a high of 123 minutes at 0100 UTC,  $\tau$  dropped to 22 minutes when the mature stage was reached. Since  $P$  and  $A$  did not change drastically over the first half hour, the large  $\tau$  was probably caused by updrafts suspending the snow in the cloud. After 0120 UTC,  $\tau$  appears to be quasi-steady with an average of 34 minutes. The local maxima at 0200 UTC and 0230 UTC occurred when there were local minima in  $dO/dt$  and local maxima in  $P$ . The occurrence of these maxima and minima suggested a higher updraft into the cloud base produced more snow in the band.

The characteristic updraft  $U$  (Fig. 4.7h) can also be considered quasi-steady with a time average of 1.2 m/s. This value fits the fall speed of aggregated snow which ranges from 0.8 m/s to 1.2 m/s (Passarelli and Srivastava 1979). Reuter (1990) suggested that the characteristic updraft could represent the average updraft in a precipitation system. Updrafts of  $\sim 1$  m/s were measured by Hobbs et al. (1980) in the instability region in a wide cold frontal rainband. Thus  $U$  could also be representative of the average updraft required to maintain snow generation in the convective clouds.

**a) Cumulative amount of snow generated**

The accumulated outflow  $O(t)$  and the accumulated amount of snow generated  $G(t)$  from time 0 to  $t$  is shown in Fig. 4.8. The two curves are rather smooth with  $O(t)$  increasing throughout the time period.  $G(t)$  shows more variation and decreases after 0250 UTC. At the end of the life cycle of the snowband  $O(t)$  converges to  $G(t)$  since  $P(t) \rightarrow 0$ . From the maximum  $G(t)$  value of 24.7 Gg/km, the latent heat of sublimation released by the snowband was 69 TJ/km ( $1 \text{ TJ} = 1 \times 10^9 \text{ kJ}$ ).

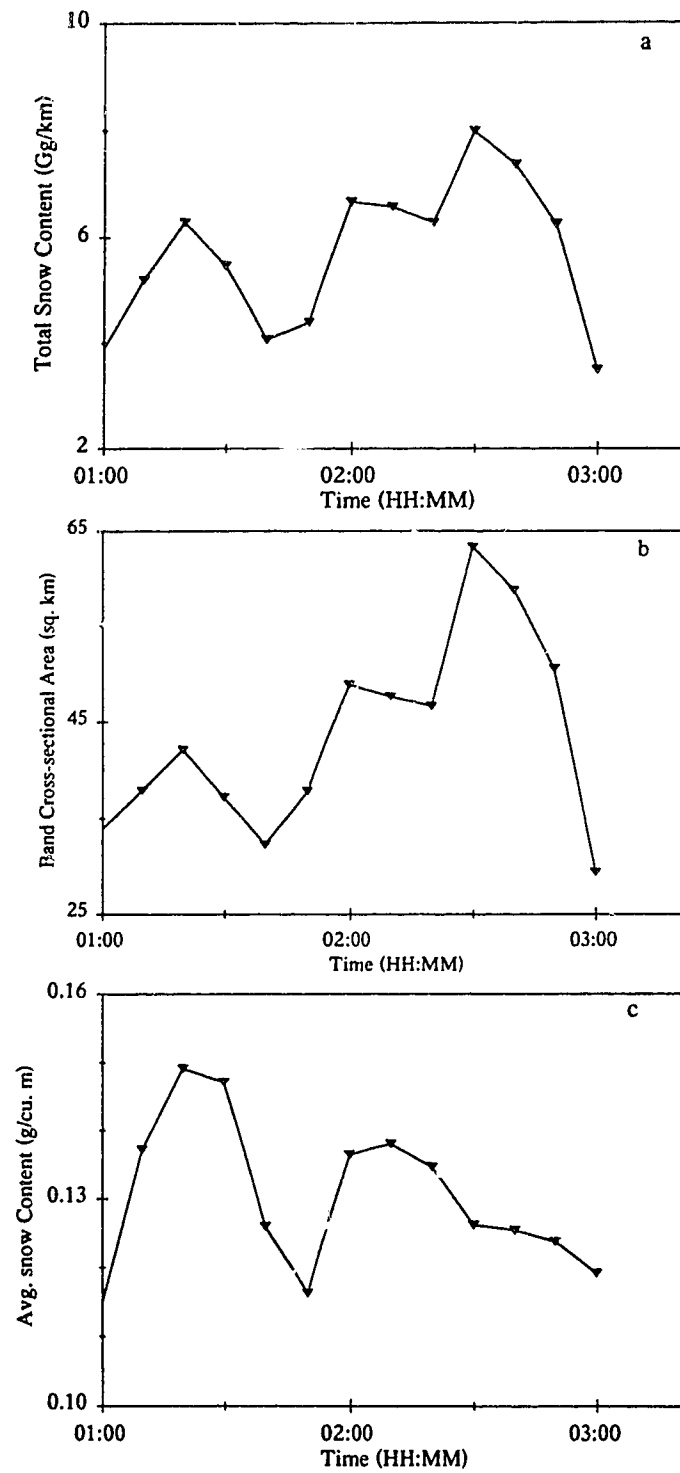


Figure 4.7: Evolution of precipitation production for 14 February 1994. Plots of (a) total snow content  $P$ ; (b) band cross-sectional area  $A$ ; and (c) average snow content  $P_{avg}$ .

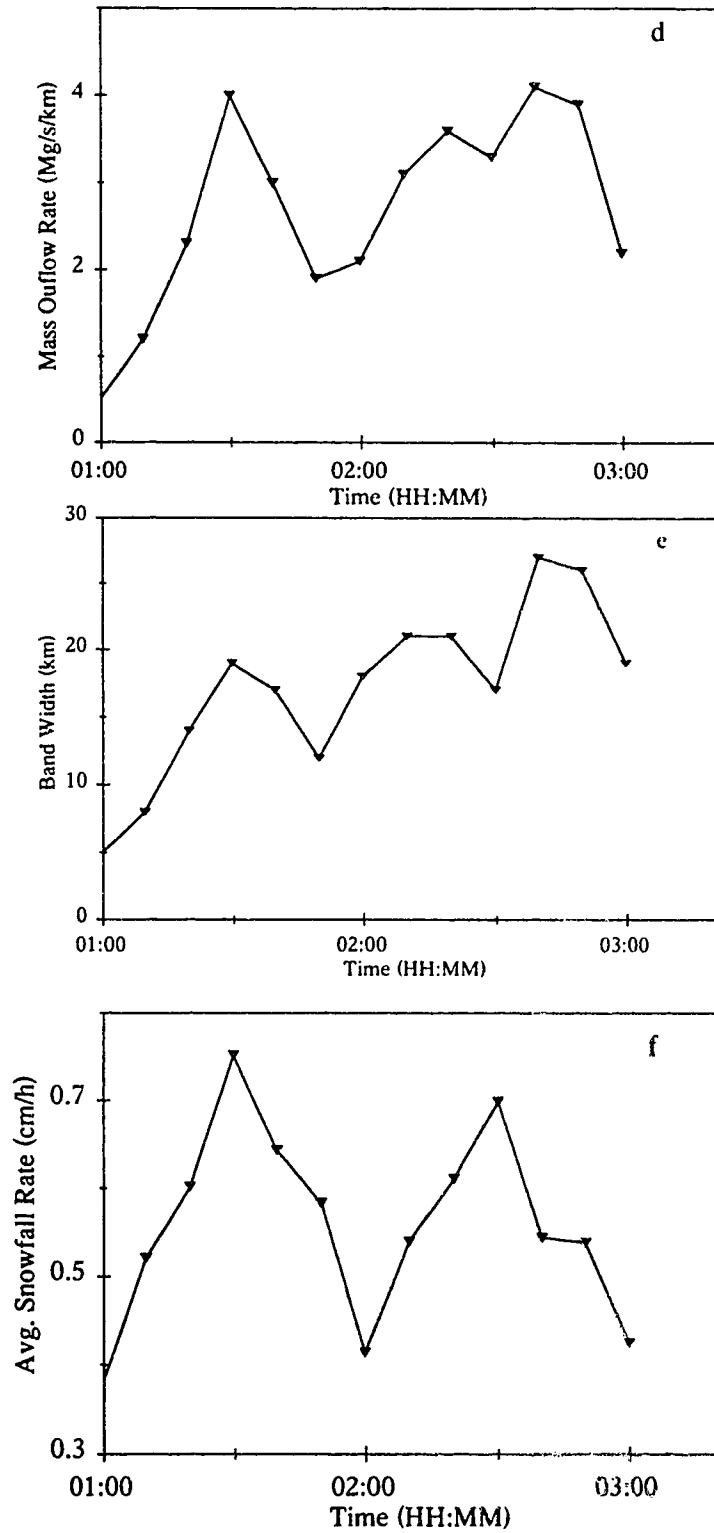


Figure 4.7: Evolution of precipitation production for 14 February 1994. Plots of (d) mass outflow rate  $dO/dt$ ; (e) band width  $W$ ; and (f) average snowfall rate  $R_{avg}$ .

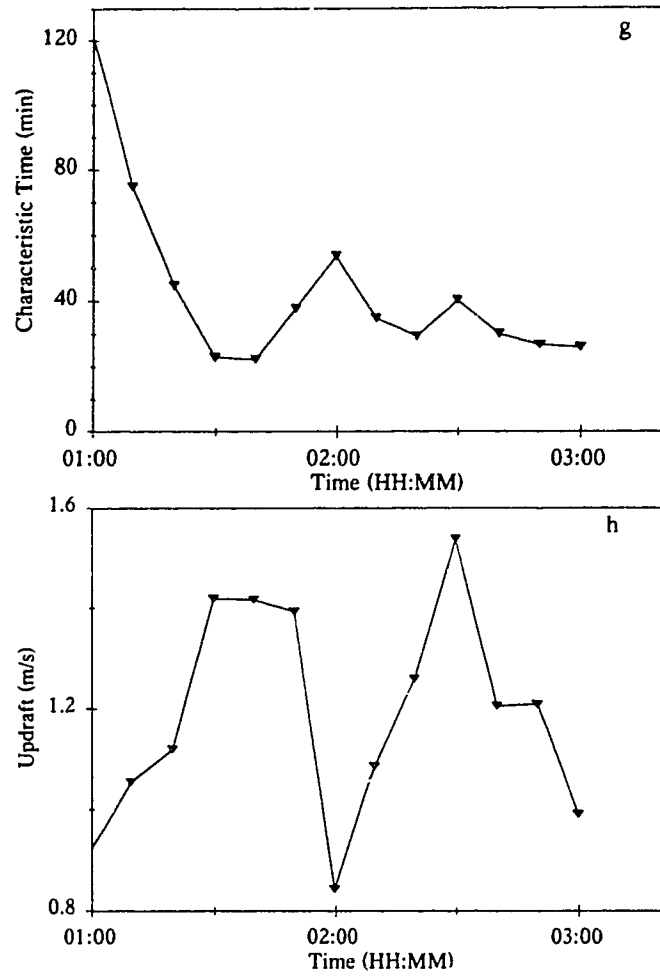


Figure 4.7: Evolution of precipitation production for 14 February 1994. Plots of (g) characteristic time  $\tau$ ; and (h) characteristic updraft  $U$ .

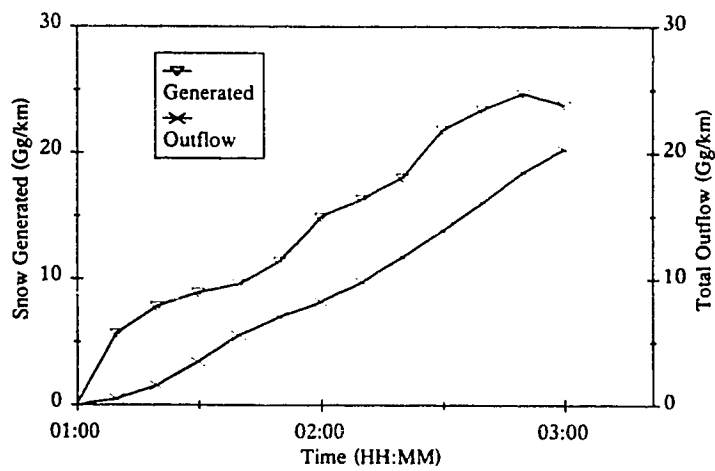


Figure 4.8: Outflow  $O(t)$  and the cumulative amount of snow generated  $G(t)$  by the snowband.



## 5 Discussion and Conclusions

### 5.1 Summary

An analysis was made of two Alberta snow events using data from radar, radiosondes, synoptic charts and satellite imagery. The focus was on precipitation production in snowbands. Precipitation production quantifies the time evolution of a snow budget integrated over the precipitation system. From digital reflectivity data  $Z_1(\text{dBz})$ , the total snow content aloft ( $P$ ) and the mass outflow rate through the cloud base ( $dO/dt$ ) were estimated using empirical  $Z_1$ - $M$  and  $Z_1$ - $R$  relations. As the snowbands were slab-symmetric, a vertical cross-section of radar data, oriented perpendicular to the band direction, was used to compute  $P$  and  $dO/dt$  over a unit length of the band. Integrating the precipitation content  $M$  over the cross-sectional area  $A$  of the snowband gives the total snow content aloft. Likewise, integrating the snowfall rate  $R$  across the width of the band  $W$  at the height of the cloud base gives the mass outflow rate.

#### *a) Warm frontal snowband*

A 986 hPa low pressure system developed over southern British Columbia on 15-16 October 1991. Heavy snow fell north of the warm front oriented in a west to east line across south-central Alberta. Snowfalls ranged from 7 cm over the eastern section to 55 cm along the foothills.

Over approximately 6 hours, the Carvel weather radar monitored the evolution of a snowband 30 km south of the city of Edmonton. The snowband nearly doubled the snowfall accumulations south of the city with 29 cm recorded at the Edmonton International Airport, while just north of the city 17 cm were recorded. The snowband, oriented in a west to east line, was parallel to the vertical shear in the layer from 635 hPa to 500 hPa. Potential for CSI existed in the layer from 700 hPa to 500 hPa at 1200 UTC. A central core of

high reflectivity was observed in this layer supporting the notion that CSI was released at this altitude.

Based on estimates of  $P$  and  $dO/dt$  for a 25 km and a 50 km cross-section of the snowband, the average snow content ( $P_{avg} = P/A$ ), the average snowfall rate ( $R_{avg} = (dO/dt)/W$ ), the characteristic time ( $\tau = P/(dO/dt)$ ) and the characteristic updraft ( $U = R_{avg}/P_{avg}$ ) were found to be roughly independent of the cross-section width. At the mature stage (0800 UTC), the band had a  $R_{avg}$  value of 0.9 cm/h, a  $P_{avg}$  value of 0.20 g/m<sup>3</sup>, a  $\tau$  value of 24 minutes and a  $U$  value of 1.2 m/s. Assuming the snowband was quasi-steady,  $\tau$  represents the time required for snow to develop, and  $U$  represents the updraft required to maintain an average snow content while snow is falling through the cloud base at the average snowfall rate. To account for the  $\tau$  and  $U$  values, a significant portion of the snow was most likely forming in the roll circulation caused by the release of CSI.

Snow budget quantities were also determined for the ambient snow field. The value of  $P_{avg}$  and  $R_{avg}$  calculated for the snowband were about twice the values calculated for the ambient snow field. The characteristic time in the snowband was 24 minutes, while in the ambient snow field it was 44 minutes. If the assumption of steady conditions were indeed valid for both regions, it can be concluded that snow formed more rapidly in the snowband than in the ambient snow field.

The characteristic updraft was larger in the synoptic snow area than in the snowband. Since the snowband was about twice the depth of the snow field this would increase the area over which the total snow content was averaged. It should be stressed that  $U$  is a measure of the updraft averaged over the entire band cross-sectional area rather than a measure of the updraft near the storm base.

The time evolution of snow budget quantities were determined from 0730 UTC to 0930 UTC. The peak in  $dO/dt$ ,  $P_{avg}$ , and  $R_{avg}$  occurred at the band's the mature stage. However the peak in  $P$  occurred 20-30 minutes prior to the mature stage which supported snow formation in mid to upper portions of the snowband. The time evolution of  $R_{avg}$ ,  $P_{avg}$ ,  $\tau$  and  $U$  indicated they were quasi-steady. Integrating the mass outflow rate over the time period and adding the total snow content aloft gives the cumulative amount of snow generated  $G(t)$ . With a value of 63.5 Gg/km, the latent heat released by the snowband was 178 TJ/km.

A sensitivity analysis was carried out on the various settings and corrections that were used to determine a snow budget. The areas removed from the analysis due to ground clutter were at the edges of the snowband so the possible precipitation lost amounted to less than 5%. Changes in budget quantities were less than 20% if the cross-section azimuth angle varied  $\pm 5^\circ$ . These effects of changing the cross-section angle supported the assumption of band slab-symmetry. Varying the reflectivity threshold by  $\pm 2$  dBz had little impact on  $P$  and  $dO/dt$  (both less than 20%). The budget parameters were also largely insensitive to changes in the cloud base height of  $\pm 100$  m. Although the sensitivity analysis was applied to this one case, it was believed that similar results would occur with other snowbands.

#### ***b) Wide cold frontal snowband***

The passage of an Arctic cold front through central Alberta resulted in the development of a number of snowbands on 13 February 1994. Atmospheric sounding data indicated that the airmass from 700 hPa to 590 hPa was moist, but not saturated. Bands, typically lasting for 3-5 hours, were oriented in west to east lines in the direction of the vertical shear from 700 hPa to 500 hPa. The sounding

analysis indicated that the potential for Convective Instability existed from 765 hPa to 590 hPa. The airmass from 590 hPa to 500 hPa was also potentially unstable for moist Symmetric Instability. Jascourt et al. (1988) found that precipitation can become organized into a band by Convective-Symmetric Instability. A vertical cross-section of the widest band indicated that the precipitation was about 5 km deep. This suggests that both types of instability may have been realized.

At its mature stage (0130 UTC), the snowband had a  $R_{avg}$  value of 0.8 cm/h, a  $P_{avg}$  value of 0.15 g/m<sup>3</sup>, a  $\tau$  value of 23 minutes and a  $U$  value of 1.4 m/s. With a life span of about 4 hours, the snowband's  $R_{avg}$  value agreed well with the observed snowfall accumulation of 5 cm. The values of  $U$  and  $\tau$  suggested that snow formation was most likely taking place in cumulus cells which developed above the frontal zone due to the release of Convective Instability.

The time evolution of snow budget quantities were determined from 0100 UTC to 0300 UTC. The peak in  $P$  occurred at 0230 UTC with a secondary maximum at 0120 UTC. The peak  $P_{avg}$  occurred at 0120 UTC indicating that the snowband was more intense at this time. The curves for both  $R_{avg}$  and  $P_{avg}$  were similar but maxima and minima for  $P_{avg}$  occurred about 10 minutes earlier. This lag of  $R_{avg}$  relative to  $P_{avg}$  is consistent with the development of snow in the convective cells. The precipitation production parameters  $R_{avg}$ ,  $P_{avg}$ , and  $U$  were quasi-steady, suggesting that Symmetric Instability may have organized the convective cells into a band. The time evolution of  $\tau$  indicated that it was not quasi-steady until about 0120 UTC suggesting that updrafts may have been suspending the snow in the cloud.

## 5.2 Comparisons between the two snowbands

Observations of the CAPPI imagery indicated that both snowbands reached their mature stage within the first hour of development. The length of time that the snowbands remained at their mature stage varied. For the warm frontal snowband, the mature stage lasted about 20-30 minutes while for the cold frontal snowband the mature stage lasted about 10 minutes. For both snowbands,  $dO/dt$  was at a maximum at the mature stage, while  $P$  reached a maximum about 10-30 minutes prior to the mature stage. The time difference between peak values in  $dO/dt$  and  $P$  was shorter for the cold frontal snowband (approximately 10 minutes) suggesting that the height where snow formed was lower than in the warm frontal snowband.

The peak  $R_{avg}$  value occurred during the time of the mature stage for both bands. Except for an approximate 10 minute lag, the maxima and minima in the time evolution of  $R_{avg}$  and  $P_{avg}$  were similar for the cold frontal snowband. For the warm frontal snowband, however, little or no correlation existed between  $R_{avg}$  and  $P_{avg}$ .

Over the two hour period, the maximum amount of snow generated were 63.5 Gg/km and 24.7 Gg/km for the warm and the cold frontal cases, respectively. Although average precipitation production values were similar for both bands, the warm frontal snowband generated about 2½ times more snow than the cold frontal snowband. This was probably related to the different properties of the two frontal airmasses. Above the frontal zone, where the snow was most likely produced, the wet bulb potential temperature ( $\theta_w$ ) was 14°C for the warm frontal case and 4°C for the cold frontal case. Thus the warm saturated airmass associated with the warm frontal case caused more snowfall.

Table 5.1 lists the integrated snow budget quantities for the warm and cold frontal snowbands averaged over a two hour period. The mass outflow rate for the warm frontal snowband was almost triple that of the cold frontal snowband, even though the warm frontal band was only twice as wide as the cold frontal band. Similarly, the cross-sectional area and the total snow content were larger for the warm frontal snowband by about 1½ and about 2½ times, respectively. Even with these differences, average and characteristic properties ( $R_{avg}$ ,  $P_{avg}$ ,  $\tau$  and  $U$ ) were quite similar for the two cases. The  $R_{avg}$  and  $P_{avg}$  for the cold frontal snowband were about 25-30% lower than values calculated for the warm frontal band. The similar  $\tau$  and  $U$  values suggested that most of the snow growth occurred by accretion and aggregation in both bands. As the  $U$  value of 1.2 m/s was much higher than typical synoptic ascent values (few cm/s), most of the snow must have developed in the layer of instability above the frontal zone.

Table 5.1: Time average of snow budget quantities for the warm and cold frontal snowbands.

Parameter	Units	Warm frontal	Cold frontal
$dO/dt$ - Mass Outflow Rate	Mg/s km <sup>-1</sup>	7.7	2.7
$W$ - Band Width	km	34	17
$R_{avg}$ - Average Pcpn. Rate	cm/h	0.8	0.6
$P$ - Total Snow Content	Gg/km	13	5.7
$A$ - Band Cross-sectional Area	km <sup>2</sup>	70	44
$P_{avg}$ - Average Pcpn. Content	g/m <sup>3</sup>	0.19	0.13
$\tau$ - Characteristic Time	min	29	34
$U$ - Characteristic Updraft	m/s	1.2	1.2

### 5.3 Comparisons with other studies

#### a) Comparison with Alberta thunderstorms

Precipitation production was used to analyze the evolution of summertime thunderstorms in Alberta (Rogers and Sakellariou 1986). It is of interest to compare the snowband budget results with those obtained for Alberta thunderstorms.

Precipitation production parameters were determined for single cell thunderstorms using data collected by the radar located in Penhold (52.2°N, 113.8°W, 904 m). The cases examined occurred on the 18 July 1977 and on the 3 July 1983. From sounding data, the airmass of 3 July 1983 had a buoyant energy of 700 J/kg or about twice that of the 18 July 1977 event. Using Z-R and Z-M relations for rain, water budget parameters were determined in a similar method used for the snowband. However, integrations were carried out over the volume of the storm to determine the total precipitation content aloft and across the area of the cloud base to determine the mass outflow rate. Since  $dO/dt$  and  $P$  were determined for a unit length of a snowband, only the quantities  $R_{avg}$ ,  $P_{avg}$ ,  $\tau$  and  $U$  were compared with those obtained for the thunderstorms.

Budget values averaged over a two hour period are shown in Table 5.2. Although the two snowbands developed in different airmasses, they produced similar  $R_{avg}$ ,  $P_{avg}$ ,  $\tau$  and  $U$  values. This was not the case for the two thunderstorms, with the July 1983 storm producing  $R_{avg}$  and  $P_{avg}$  values that were about double those for the July 1977 storm. Budget values suggest that precipitation production is more vigorous in thunderstorms than in snowbands. With  $P_{avg}$  2 to 3 times greater for the thunderstorms, the  $R_{avg}$  was 8 to 30 times greater. The characteristic updraft value suggest that rain has a larger terminal velocity than snow. Thus, falling

rain drops grow more rapidly collecting cloud droplets than slowly falling snowflakes.

Table 5.2: Budget comparisons between the snowbands and two Alberta thunderstorms (Rogers and Sakellariou 1986). The values listed are 2 hour averages of quantities during the storm's mature stage.

Event Type/Date	$R_{avg}$ (mm/h)	$P_{avg}$ (g/m <sup>3</sup> )	$\tau$ (min)	U (m/s)
Warm frontal snowband (16 Oct. 1991)	0.8	0.19	29	1.2
Cold frontal snowband (13 Feb. 1994)	0.6	0.13	34	1.2
Moderate Thunderstorm (18 July 1977)	7	0.3	18	7
Intense Thunderstorm (3 July 1983)	18	0.5	25	10

#### b) Comparison with other precipitation band studies

A search through the research literature failed to find studies of precipitation production in snowbands. However integrated water budget parameters were reported for rainbands that developed over western Washington state. Using radar observations, the mass outflow rate for a wide cold frontal rainband was computed to be 40-50 Mg/s km<sup>-1</sup> (Hobbs et al. 1980). For a warm frontal rainband, the mass outflow rate was 58 Mg/s km<sup>-1</sup> (Houze et al. 1981). The much larger values for the rainbands compared to values obtained for the two Alberta snowbands could be attributed to liquid-ice phase differences, and the lack of a mountain chain to "wring" out moisture from the cyclone.

Average precipitation content values have also been determined for precipitation bands. Herzegh and Hobbs (1980) determined a vertical profile of precipitation content within a warm frontal rainband. The average precipitation content above the melting layer for one of the rainbands was 0.1 g/m<sup>3</sup> to 0.2 g/m<sup>3</sup> which is similar to the Alberta



snowband cases. This agreement is probably related to a similar Pacific airmass affecting both regions. Much higher average precipitation content values have been observed in other snowbands. For example, Zawadzki et al. (1993a) reported average precipitation contents as high as  $0.9 \text{ g/m}^3$  for a snowband associated with a cyclone developing over the Atlantic.

#### 5.4 Discussion

This thesis is novel in two aspects. First, it extends the analysis of precipitation production to snowbands, whereas previous studies focused on summertime convection. This was done by using appropriate Z-R and Z-M relations for snow. Second, the stability analysis using the Richardson number was extended to include the thermodynamic effects of the ice phase. In both cases it was found that the ice phase processes had only minute effects in the stability of the airflow, despite the fact that the release of latent heat due to sublimation is almost 13% larger than that due to vapourization.

For the warm frontal case, potential for Conditional Symmetric Instability was observed for a layer above the frontal zone. Likewise, potential for Convective Instability was observed for a layer above the cold front. Despite differences in airmass stability and characteristics, the values for the average snow content, average snowfall rate, characteristic time and characteristic updraft were similar for both cases.

## 5.5 Recommendations for further research

Our research on precipitation production can be extended in several ways. An important contribution would be to quantify the errors caused by inaccurate observations, on various terms in the water budget equation. Special attention should be given to the role of partial beam filling and its contribution to integrated storm parameters. The technique used by Amayenc et al. (1989) may be useful to evaluate the errors. Precipitation production can also be improved by determining empirical Z-R and Z-M relationships for the radar located at Carvel.

A useful extension of this study would be to build a database of snowband cases and their relation to synoptic conditions. This should clarify which environmental factors control snow production. Ambient kinematic and thermodynamic data for case studies could be obtained from numerical weather models. These data, in conjunction with simulation results from a numerical cloud model, would provide three dimensional microphysical and dynamical properties of the snowband.

Precipitation production could also be used as a short term (~3 hours) forecasting tool to assess the potential for further development of a precipitation system. By programming the formulae into a weather radar system, integrations would be carried out over the volume of the storm to determine the total precipitation content aloft and the mass outflow rate through cloud base level. The forecaster would specify a reflectivity threshold, a cloud base height, and the section on the radar display where budget parameters are to be determined. Graphical displays of the time histories of selected budget quantities could be automatically updated after each new scan of the precipitation system.

## Bibliography

- Aktary, N. and G. W. Reuter, 1993: Observations of a snow band in a symmetrically unstable flow over Alberta, *Contr. Atmos. Phys.*, **66**, 275-282.
- Al-Jumily, K. J., Charlton, R. B., and R. G. Humphries, 1991: Identification of rain and hail with circular polarization radar, *J. Appl. Met.*, **30**, 1075-1087.
- Amayenc, P., Marzoug, M., and J. Testud 1989: Non uniform beam filling effects in measurements of rainfall rate from a spaceborne radar, *Proc. 24th Conf. on Radar Meteorology, 17-20 March 27-31, 1989, Tallahassee, Florida, Am. Met. Soc., Boston*, 569-572.
- Auer, A. H. and J. D. Marwitz, 1968: Estimates of air and moisture flux into hailstorms on the High Plains, *J. Appl. Met.*, **7**, 196-198.
- Barge, B. L., 1968: Thunderstorm energy budgets from radar data, Pre-prints, *Proc. 13th Radar Meteorology Conf., 20-23 August 1968, Montreal, Que., Am. Met. Soc.*, 114-117.
- Battan, L. J., 1973: *Radar observation of the atmosphere*, revised edition, University of Chicago Press, Chicago, 324 pp.
- Bennetts, D. A. and B. J. Hoskins, 1979: Conditional symmetric instability - a possible explanation for frontal rainbands, *Quart. J. Roy. Met. Soc.*, **105**, 945-962.
- , and J. C. Sharp, 1982: The relevance of conditional symmetric instability to the prediction of mesoscale frontal rainbands, *Quart. J. Roy. Met. Soc.*, **108**, 595-602.
- Bevington, P. R., 1969: *Data reduction and error analysis for the physical sciences*, McGraw-Hill, New York, 336 pp.
- Bjerknes, J., 1919: On the structure of moving cyclones. *Geophysical Publikationer*, **1**, No. 2.
- , and H. Solberg, 1922: Life cycle of cyclones and the polar frontal theory of atmospheric circulation, *Geophysical Publikationer*, **3**, No. 1, 3-18.

- Bolton, D., 1980: The computation of equivalent potential temperature, *Mon. Wea. Rev.*, **108**, 1045-1053.
- Bosart, L. F., and F. Sanders, 1985: Mesoscale structure in the megalopolitan snowstorm of 11-12 February 1983. Part III: A large-amplitude gravity wave and coastal frontogenesis, *J. Atmos. Sci.*, **43**, 924-939.
- Braham, R. R., 1952: The water and energy budgets of the thunderstorm and their relation to thunderstorm development, *J. Met.*, **9**, 227-242.
- Browning, K. A. and T. W. Harrold, 1969: Air motion and precipitation growth in a wave depression, *Quart. J. Roy. Met. Soc.*, **95**, 288-309.
- , Hardman, M. E., Harrold, T. W. and C. W. Pardoe, 1973: The structure of rainbands within a mid-latitude depression, *Quart. J. Roy. Met. Soc.*, **99**, 215-231.
- , 1974: Mesoscale structure of rain systems in the British Isles, *J. Met. Soc. Japan*, **50**, 314-327.
- Byers, H. R. and R. R. Braham, 1949: *The Thunderstorm*, U.S. Government Printing Office, Washington, D.C., 287 pp.
- Byrd, G. P., 1989: A composite analysis of winter season overrunning precipitation bands over the southern plains of the United States, *J. Atmos. Sci.*, **46**, 1119-1132.
- Carbone, R. E., 1982: A severe frontal rainband. Part I: Stormwide hydrodynamic structure, *J. Atmos. Sci.*, **39**, 258-279.
- , and A. R. Bohne, 1975: Cellular snow generation - A Doppler radar study, *J. Atmos. Sci.*, **32**, 1384-1394.
- Cheng, L., and M. English, 1983: A relationship between hailstone concentrations and size, *J. Atmos. Sci.*, **40**, 204-213.
- Chisholm, A. J., and J. H. Renick, 1972: Supercell and multicell Alberta hailstorms, *Abstracts, Intern. Conf. on Cloud Phys.*, London, England, 67-68.
- Chung, Y. S., K. D. Hage and E. R. Reinelt, 1976: On lee cyclogenesis and airflow in the Canadian Rocky Mountains and the East Asian Mountains, *Mon. Wea. Rev.*, **104**, 879-891.

- Cotton, W. R., 1990: *Storms*, 1st edition, Geophysical Science Series Vol. 1, Fort Collins, 158 pp.
- Cressman, G. P., 1959: An operational objective analysis system, *Mon. Wea. Rev.*, **87**, 367-374.
- Crozier, C. L., 1986: *King weather operations manual and users guide*, Internal publication, Atmospheric Environment Services, Toronto, 423 pp.
- Donald, T. W., 1983: *Calculus and analytic geometry*, Addison-Wesley, Don Mills, 866 pp.
- Donaldson, N. R., and R. E. Stewart, 1989: On the precipitation regions within two storms affecting Atlantic Canada, *Atmos. Ocean*, **27**, 108-129.
- Durran, D. R., and J. B. Klemp, 1982: On the affects of moisture on the Brunt-Väisälä frequency. *J. Atmos. Sci.*, **39**, 2152-2158.
- Elliot, R. D. and E. L. Hovind, 1964: On convective bands within Pacific Coast storms and their relation to storm structure, *J. Appl. Met.*, **3**, 143-154.
- Emanuel, K. A., 1979: Inertial instability and mesoscale convective systems. Part I: Linear theory of inertial instability in rotating viscous fluids, *J. Atmos. Sci.*, **38**, 2425-2449.
- , 1980: Forced and free mesoscale motions in the atmosphere, *Collection of Lecture Notes on Dynamics of Mesometeorological Disturbances*, CIMMS Symposium, University of Oklahoma/NOAA, Norman, 191-259.
- , 1983a: The Lagrangian parcel dynamics of moist symmetric instability, *J. Atmos. Sci.*, **40**, 2368-2376.
- , 1983b: In assessing local conditional symmetric instability from atmospheric soundings, *Mon. Wea. Rev.*, **111**, 2016-2033.
- , 1988: Observational evidence of slantwise convective adjustment, *Mon. Wea. Rev.*, **116**, 1805-1816.
- English, M., 1973: Growth of large hail in Alberta hailstorms, Part II, *Met. Monogr.*, **36**, 37-98.
- , Kochtubajda, B., and F. D. Barlow, 1991: Radar measurements of rainfall by differential propagation phase: A pilot experiment, *Atmos. Ocean*, **29**, 357-380.

- Environment Canada, 1986: *Climate Atlas Climatique-Canada: A series of maps portraying Canada's climate, Map series II-precipitation*, Minister of Supply and Services Canada.
- Fankhauser, J. C., 1971: Thunderstorm-environment interactions determined from aircraft and radar observations, *Mon. Wea. Rev.*, **99**, 171-192.
- Foote, G. B. and J. C. Fankhauser, 1973: Airflow and moisture budget beneath a northeast Colorado hailstorm, *J. Appl. Met.*, **12**, 1330-1353.
- Gendron, Y., 1991: The January 1989 central Alberta Blizzard, *Western Region Tech. Notes*, **91-N-103**, Atmospheric Environment Services, Edmonton.
- Geotis, S. G., 1971: Thunderstorm water contents and rain fluxes deduced from radar, *J. Appl. Met.*, **10**, 1233-1237.
- Gunn, K. L. S., and T. W. R. East, 1954: The microwave properties of precipitation properties, *Quart. J. Roy. Met. Soc.*, **80**, 522-545.
- , and J. S. Marshall, 1958: The distribution with size of aggregate snowflakes, *J. Met.*, **15**, 452-466.
- Haltiner, G. J., and R. T. Williams, 1980: *Numerical prediction and dynamic meteorology*, 2nd edition, John Wiley and Sons, New York, 477 pp.
- Harrold, T. W. and P. M. Austin, 1974: The structure of precipitation systems - a review, *J. Rech. Atmos.*, **8**, 41-57.
- Herzogh, P. H. and P. V. Hobbs, 1980: The mesoscale and microscale structure and organization of clouds and precipitation in mid-latitude cyclones. II: Warm-frontal clouds, *J. Atmos. Sci.*, **37**, 597-611.
- Hobbs, P. V., 1978: Organization and structure of clouds and precipitation on mesoscales and microscales in cyclonic storms, *Rev. Geophys. and Space Phys.*, **16**, 741-755.
- , and J. D. Locatelli 1978: Rainbands, precipitation cores and generating cells in a cyclonic storm, *J. Atmos. Sci.*, **35**, 230-241.
- , Matejka, T. J., Herzogh, P. H., Locatelli, J. D., and R. A. Houze, Jr., 1980: The mesoscale and

- microscale structure and organization of clouds and precipitation in midlatitude cyclones. I: A case study of a cold front, *J. Atmos. Sci.*, 37, 568-596.
- , and O. G. Persson, 1982: The mesoscale and microscale structure and organization of clouds and precipitation in mid-latitude cyclones. V: The substructure of narrow cold-frontal rainbands, *J. Atmos. Sci.*, 39, 280-295.
- Holt, A. R., Joe, P. I., McGuinness, R., Torlaschi, E., Nichols, T., Bergwall, F., and D. A. Holland, 1994: simultaneous polarization and Doppler observations of severe convective storms in central Alberta, *Atmos. Res.*, 33, 37-56.
- Holtz, C. D. and J. S. Marshall, 1966: Total precipitation aloft in a summer storm, *Proc. 12th Conf. on Radar Meteorology, 17-20 October 1966*, Norman, Oklahoma, Am. Met. Soc., Boston, 110-113.
- , 1968: Life-cycle of a summer storm from radar records, Ph.D. Thesis, Dept. of Meteorology, McGill Univ., Montreal, 141 pp.
- Houze, Jr, R. A., Hobbs, P. V., Biswas, K. R. and W. M. Davis, 1976a: Mesoscale rainbands in extratropical cyclones, *Mon. Wea. Rev.*, 104, 868-878.
- , Locatelli, J. D. and P. V. Hobbs, 1976b: Dynamics and cloud microphysics of rainbands in an occluded frontal system, *J. Atmos. Sci.*, 33, 1921-1936.
- , Rutledge, S. A., Matejka, T. J., and P. V. Hobbs, 1981: The mesoscale and microscale structure and organization of clouds and precipitation in mid-latitude cyclones. III: Air motions and precipitation growth in a warm-frontal rainband, *J. Atmos. Sci.*, 38, 639-649.
- Imai, I., Fujiwara, M., Ichimaura, I., and Y. Toyama, 1955: Radar reflectivity of falling snow, *Papers Met. Geophys. (Japan)*, 6, 130-139.
- Iribarne, J. V., and W. L. Godson, 1986: *Atmospheric thermodynamics*, 2nd edition, Reidel Publishing Company, Boston, 259 pp.
- Jascourt, S. D., Lindstrom, S. S., Seman, C. J., and D. D. Houghton, 1988: An observation of banded convective

- development in the presence of weak symmetric stability, *Mon. Wea. Rev.*, 116, 175-191.
- Kaylor, R., and A. J. Fallor, 1972: Instability of the stratified Ekman boundary layer and the generation of internal waves, *J. Atmos. Sci.*, 29, 497-509.
- Kessler, E., 1969: On the distribution and continuity of water substance in atmospheric circulations, *Met. Monogr.*, 32, Am. Met. Soc., Boston, 84 pp.
- Kochtubajda, B., 1991: Application of radar-derived rainfall measurements in a forage insurance program, *Proc. 25th Inter. Conf. on Radar Meteorology, 24-28 June 1991*, Paris, France, Am. Met. Soc., Boston, 572-575.
- Krauss, T. W., and J. D. Marwitz, 1984: Precipitation processes within an Alberta supercell hailstorm, *J. Atmos. Sci.*, 41, 1025-1034.
- Larochelle, B., 1991: A 75,000 Gigawatt snowfall in Alberta November 23, 1990, *Western Regional Tech. Notes*, 91-N-101, Atmospheric Environment Services, Edmonton.
- , 1994: *Application of the synthetic dual-Doppler technique to an operational Doppler weather radar*, M.Sc. thesis, Dept. of Geography, University of Alberta, Edmonton, 138 pp.
- Lilly, D. K., 1966: On the instability of the Ekman boundary layer flow, *J. Atmos. Sci.*, 23, 481-494.
- Lindzen, R. S. and K. K. Tung, 1976: Banded convective activity and ducted gravity waves, *Mon. Wea. Rev.*, 104, 1602-1617.
- List, R. J., 1963: *Smithsonian Meteorological Tables*, 6th edition, Smithsonian Institute, Washington, 527 pp.
- Longley, R. W., and C. E. Thompson, 1955: A study of the causes of hail, *J. Appl. Met.*, 4, 69-82.
- Ludlam, F. H., 1980: *Clouds and Storms*, Pennsylvania State University Press, University Park, 405 pp.
- Marshall, J. S., 1953: Precipitation trajectories and patterns, *J. Met.*, 10, 25-29.
- Matejka, J., Houze, Jr, R. A. and P. V. Hobbs, 1980: Microphysics and dynamics of clouds associated with mesoscale rainbands in extratropical cyclones, *J. Roy. Met. Soc.*, 106, 29-56.



- McLaughlin, M. R., 1967: The energy budget of a severe local storm, Rep. No. 7, Atmospheric Science Group, University of Texas, Austin, 57 pp.
- Meeus, J., 1988: *Astronomical formulae for calculators*, Willmann-Bell, Inc., 36-37.
- Moore, J. T. and P. D. Blakley, 1988: The role of frontogenetical forcing and conditional symmetric instability in the Midwest snowstorm of 30-31 January 1982, *Mon. Wea. Rev.*, **116**, 2155-2171.
- Moore, C. G., and R. L. Vaughan, 1978: An economical technique for Cartesian interpolation and display of reflectivity factor data in three-dimensional space, *Proc. 18th Radar Met. Conf. Proceedings, 1978, Atlanta, Georgia, Am. Met. Soc., Boston*, 490-496.
- Nozumi, Y., and H. Arakawa, 1968: Pre-frontal rainbands in the warm sector of sub-tropical cyclones over the ocean, *J. Geophys. Res.*, **73**, 487-492.
- Parsons, D. B. and P. V. Hobbs, 1983a: The mesoscale and microscale structure and organization of clouds and precipitation in mid-latitude cyclones. VII: Formation, development, interaction and dissipation of rainbands, *J. Atmos. Sci.*, **40**, 559-579.
- , and P. V. Hobbs, 1983b: The mesoscale and microscale structure and organization of clouds and precipitation in mid-latitude cyclones. XI: Comparisons between observational and theoretical aspects of rainbands, *J. Atmos. Sci.*, **40**, 2377-2397.
- Passarelli, R. E., Jr., and R. C. Srivastava, 1979: A new aspect of snowflake aggregation theory, *J. Atmos. Sci.*, **36**, 484.
- Pell, J., 1971: The use of broad-beam radar for quantitative analysis of severe storms, *J. Appl. Met.*, **10**, 1238-1251.
- Petterssen, S., 1940: *Weather analysis and forecasting*, McGraw-Hill, 505 pp.
- Robert Jones, J. R., 1962: The radar equation in meteorology, *Quart. J. Roy. Met. Soc.*, **88**, 485-495.
- Ray, P. S., 1986: *Mesoscale meteorology and forecasting*, Am. Met. Soc., Boston, 793 pp.

- Reinelt, E. R., 1970: On the role of orography in the precipitation regime of Alberta, *The Albertan Geographer*, 6, 45-58.
- Renick, J. H., and J. B. Maxwell, 1977: Forecasting hailfall in Alberta, *Met. Monogr.*, 38, Am. Met. Soc., Boston, 145-151.
- Reuter, G. W. and M. K. Yau, 1990: Observation of slantwise convective instability in winter cyclones, *Mon. Wea. Rev.*, 118, 447-458.
- , and —————, 1993: Assessment of slantwise convection in ERICA cyclones, *Mon. Wea. Rev.*, 121, 375-386.
- , 1990: Radar observations of precipitation production in thunderstorms, *Atmos. Ocean*, 28, 216-229.
- , and C. D. Nguyen, 1993: Organization of cloud and precipitation in an Alberta storm, *Atmos. Res.*, 30, 127-141.
- , and N. Aktary, 1995: Convective and symmetric instabilities and their effects on precipitation: Seasonal variations in central Alberta during 1990 and 1991, *Mon. Wea. Rev.*, 123, 153-162.
- Rogers, R. R., 1971: The effect of variable target reflectivity on weather radar measurements, *Quart. J. Roy. Met. Soc.*, 97, 154-167.
- , and N. K. Sakellariou, 1986: Precipitation production in three Alberta thunderstorms, *Atmos. Ocean*, 24, 145-168.
- , and M. K. Yau, 1989: *A short course in cloud physics*, Third edition. Pergamon Press, Oxford, 293 pp.
- Rutledge, S. A., and P. V. Hobbs, 1983: The mesoscale and microscale structure and organization of clouds and precipitation in mid-latitude cyclones. VII: A model for the "Seeder-Feeder" process in warm-frontal rainbands, *J. Atmos. Sci.*, 40, 1185-1206.
- Sanders, F., 1955: An investigation of the structure and dynamics of an intense surface frontal zone, *J. Met.*, 12, 542-552.

- \_\_\_\_\_, 1986: Frontogenesis and symmetric instability in a major New England snowstorm, *Mon. Wea. Rev.*, **114**, 1847-1862.
- \_\_\_\_\_, and L. F. Bosart, 1985: Mesoscale structure in the megalopolitan snowstorm of 11-12 February 1983. Part I: Frontogenetical forcing and symmetric instability, *J. Atmos. Sci.*, **42**, 1050-1061.
- Sauvageot, H., 1992: *Radar Meteorology*. Artech House, Boston, 366 pp.
- Sekhon, R. S., and R. C. Srivastava, 1970: Snow size spectra and radar reflectivity, *J. Atmos. Sci.*, **27**, 299-307.
- Seltzer, M. A., Passarelli, R. E., and K. A. Emanuel, 1985: The possible role of symmetric instability in the formation of precipitation bands, *J. Atmos. Sci.*, **42**, 2207-2219.
- Shields, M. T., Rauber, R. M., M. K. Ramamurthy, 1991: Dynamical forcing and mesoscale organization of precipitation bands in a midwest winter cyclonic storm, *Mon. Wea. Rev.*, **119**, 936-964.
- Sienkiewicz, J. M., Locatelli, J. D. Hobbs, P. V., and B. Geerts, 1989: Organization and structure of clouds and precipitation on the Mid-Atlantic coast of the United States. Part II: The mesoscale and microscale structures of some frontal rainbands, *J. Atmos. Sci.*, **46**, 1349-1364.
- Sikdar, D. N., Schlesinger, R. E., and C. E. Anderson, 1974: Severe storm latent heat release: Comparison of radar estimates versus a numerical experiment, *Mon. Wea. Rev.*, **102**, 455-465.
- Smith, S. B., and M. K. Yau, 1987: The mesoscale effect of topography on the genesis of Alberta hailstorms, *Contr. Atmos. Phys.*, **60**, 371-392.
- \_\_\_\_\_, and \_\_\_\_\_, 1993a: The causes of severe convective outbreaks in Alberta. Part I: A comparison of a severe outbreak with two non-severe events, *Mon. Wea. Rev.*, **121**, 1099-1125.
- \_\_\_\_\_, and \_\_\_\_\_, 1993b: The causes of severe convective outbreaks in Alberta. Part II: Conceptual model and statistical analysis, *Mon. Wea. Rev.*, **121**, 1126-1133.

- Solberg, H., 1930: *Verhandl. III Intern. Kongr. Tech. Mechanik*, Stockholm.
- Vickers, G. G., 1975: *Diffluence and cyclogenesis in the lee of the Rocky Mountains*, M.Sc. thesis, Dept. of Geography, University of Alberta, Edmonton, 126 pp.
- Wallace, J. M., and P. V. Hobbs, 1977: *Atmospheric science: An introductory survey*, Academic Press, New York, 467 pp.
- Wexler, R., 1955: Radar analysis of precipitation streamers observed 25 February 1954, *J. Met.*, 12, 391-393.
- Wolfsberg, D. G., Emanuel, K. A., and R. E. Passarelli, 1986: Band formation of a New England winter storm, *Mon. Wea. Rev.*, 114, 1552-1569.
- Wojtiw, L., 1975: Climatology of hailstorms in Alberta, *NHRE Symposium/Workshop on Hail*, Estes Park, NCAR, Boulder, Colorado, Preprint I, Sec. 11, c. 3, 14 pp.
- Xu, Q. and J. H. E. Clark, 1985: The nature of symmetric instability and its similarity to convective and inertial instability, *J. Atmos. Sci.*, 42, 2880-2883.
- Young, K. C., 1993: *Microphysical processes in clouds*, Oxford University Press, New York, 427 pp..
- Zawadzki, I., 1973: The loss of information due to finite sample volume in radar-measured reflectivity, *J. Appl. Met.*, 12, 683-687.
- , Zwack, P., and A. Frigon, 1993a: A study of a CASP storm: Analysis of radar data, *Atmos. Ocean*, 31, 175-199.
- , Ostiguy, L., and J. P. R. Laprise, 1993b: Retrieval of the microphysical properties in a CASP storm by integration of a numerical kinematic model, *Atmos. Ocean*, 31, 200-232.